Improvements in finite element models of spinal cord injury and interpretation of mechanical outputs using machine learning

by

Cesar Alejandro Jimenez Gonzalez

B.S., Monterrey Institute of Technology – Campus Queretaro, 2020

Thesis Submitted in Partial Fulfillment of the
Requirements for the Degree of
Master of Applied Science

in the
School of Mechatronic Systems Engineering
Faculty of Applied Sciences

SIMON FRASER UNIVERSITY
Spring 2024

Declaration of Committee

Name:	**Cesar Alejandro Jimenez Gonzalez**
Degree:	**Master of Applied Science**
Title:	**Improvements in finite element models of spinal cord injury and interpretation of mechanical outputs using machine learning**
Committee:	**Chair: Mohammad Narimani** Senior Lecturer, Mechatronic Systems Engineering
	Carolyn J. Sparrey Supervisor Associate Professor, Mechatronic Systems Engineering
	Edward Park Committee Member Professor, Mechatronic Systems Engineering
	Salvatore Federico Committee Member Professor, Mechanical and Manufacturing Engineering University of Calgary
	Shervin Jannesar Committee Member Lecturer, Engineering Science
	Siamak Arzanpour Examiner Professor, Mechatronic Systems Engineering

Abstract

This thesis explores the correlation between mechanical impact and neurological damage in spinal cord injury (SCI) through computational modeling and machine learning (ML). It emphasizes on the role of the cerebrospinal fluid (CSF) boundary conditions and morphology in SCI models and the classification of injured elements using ML algorithms. Findings reveal the major influence of CSF boundary conditions and morphology on the predicted mechanical outcomes, highlighting the importance of proper modelling choices for enhancing the models' biofidelity. Furthermore, the integration of supervised ML techniques facilitates the classification of injured elements based on FE model results, providing valuable insights into specific damage mechanisms. Additionally, the feature importance analysis and injury threshold estimation reveal distinct susceptibility patterns in gray and white matter tissues. This work contributes to the development of more reliable computational models and innovative approaches for SCI prevention and treatment, addressing a critical need in the field of SCI research.

Keywords: Spinal cord injury; Finite element analysis; CSF representation; Supervised machine learning; Injury identification

To my family and friends back home.

To the decisions and experiences that took me more than 3770 km away from Queretaro to do research.

And to the new friends I made along the way.

It was a long journey, but we made it.

"A los que buscan, aunque no encuentren; a los que avanzan, aunque se pierdan; a los que viven, aunque se mueran." - Mario Benedetti

Acknowledgements

I would like to start these acknowledgements by expressing my deep appreciation to my supervisor, Dr. Carolyn J. Sparrey. Without her guidance and assistance, it would not have been possible for me to complete this thesis. Her calm, precise, and rigorous feedback on my writing and research work was paramount to my growth as a professional. She has set a high standard for future mentoring figures, and I hope we remain connected.

I also want to thank my supervisory committee members for their support and patience. I valued Dr. Park's questions that helped me identify parts of my research that could be better explained. I am also grateful for Dr. Federico's insights on my FE models and his teachings on the importance and beauty of math in mechanics. Moreover, I have Dr. Jannesar to thank for his previous mentorship and support in my coming back to Canada. I hope my thesis highlights the admiration and respect I have for his work and for him as a professional. I want to extend my gratitude to my colleagues at the NeuroSpine Lab and to the members of the MSE department. Especially to Dexter Lagasca, with whom I have been honoured to collaborate, and Dr. Mohammad Narimani, whose trust and guidance on my final project resulted in a paper accepted at an international conference.

A huge thanks to my friends Edgardo, Dani, Gera, and Josh for having visited Vancouver and having brought a bit of Mexico with them. To my carnales: Edgardo and Josh, thank you for having consistently been a great source of distraction and laughter. I could not have asked for better friends. To my friends Ana Vi and Grace, thank you for all those conversations and your advice. To my buddies: Cris, Gabo, Lalo, and Hectorin, thank you for those fun/stressful gaming sessions. And to the people that made it a pleasure to live in Vancouver: Aadi, Ahmad, Andrea, Ann and her family, Gaby, Jason, Priyaa, Raven, and the ALAS and LDP groups, from the bottom of my heart, thank you.

To my partner, Ann, I thank her for the patience and kindness she showed me, particularly during the last year. I deeply appreciated her concern for my wellbeing, her encouraging words, her writing support, and her comforting hugs. The most significant acknowledgement is reserved for my parents, Irma and Jesus, and my sister Brenda. It has been their love and unwavering belief in me that have allowed me to achieve everything that I have. They were my inspiration to keep going during this life-changing experience that was the master's program, and as such, I dedicate this thesis to them.

Table of Contents

List of Tables

List of Figures

List of Acronyms

AB	Alternating-boundary
AI	Artificial intelligence
AUC	Area under the receiver operating characteristic curve
CB	Closed-boundary
CNS	Central nervous system
CSF	Cerebrospinal fluid
CV	Cross-validation
DT	Decision trees
ESEDEN	Strain energy density
FE	Finite element
FSI	Fluid-structure interactions
GM	Gray matter
KNN	K-nearest neighbors
LEAXON	Logarithmic strain in axonal direction
LEP	Principal logarithmic strain
LR	Logistic regression
ML	Machine learning
MRI	Magnetic resonance imaging
NHP	Non-human primates
OB	Open-boundary
QLV	Quasi-linear viscoelastic
SCI	Spinal cord injury
SD	Standard deviation
SPH	Smoothed particle hydrodynamics
SVM	Support vector machines
TRESCA	Tresca stress
VR	Volume reduction
WM	White matter

Glossary

Caudal	Directed towards the back end of the model
Contralateral	Occurring on the opposite side of the model
Dorsal	Directed towards the upper section of the model
Ipsilateral	Occurring on the same side of the model
Lateral	Directed away from the midline of model
Rostral	Directed towards the front end of the model
Ventral	Directed towards the lower section of the model

Preface

A version of Chapter 2 will be submitted for publication as a full-length article to a journal yet to be determined - Jimenez, C., & Sparrey, C. J., Methods for containing the cerebrospinal fluid in a computer simulation of large animal cervical spinal cord injury using smoothed particle hydrodynamics. In this study, I was responsible for generating and running the computational models of spinal cord injury, extracting the outcomes from the output files, analyzing the data, and writing the document. Dr. Carolyn Sparrey provided guidance and support on the computational modelling choices, the analysis of data, and the preliminary writing of the future paper.

A version of Chapter 3 was published as a full-contributed paper in the 45th Annual International Conference of the IEEE Engineering in Medicine and Biology Society (EMBC 2023) - Jimenez, C., Sparrey, C. J., & Narimani, M. (2023). Identification of injured elements in computational models of spinal cord injury using machine learning. Annual International Conference of the IEEE Engineering in Medicine and Biology Society. IEEE Engineering in Medicine and Biology Society. Annual International Conference, 2023, 1–4. https://doi.org/10.1109/EMBC40787.2023.10340243. For this paper, I was responsible for coding the sequences for training and testing of the machine learning algorithms, the collection and processing of the results, and writing the manuscript. Dr. Carolyn Sparrey and Dr. Mohammad Narimani provided their assistance defining the best methodologies to implement, interpreting the results, and iteratively reviewing the manuscript prior to submission.

Chapter 1.

Introduction

1.1. Motivation

Spinal cord injury (SCI) is a global health concern, affecting between 250,000 and 500,000 individuals worldwide every year [1]. According to the Rick Hansen Spinal Cord Injury Registry: A look at traumatic SCI in Canada in 2019 [2], SCI affects over 86,000 individuals in Canada, from which more than half of the cases are the result of a traumatic event, such as transportation accidents or falls. There is currently no cure for SCI, although promising treatments have emerged, demonstrating potential for enhancing the quality of life in affected patients [1].

Given the traumatic nature of most cases of SCI [3], one of the keys to preventing SCI or effectively diagnosing injury lies in understanding the correlation between the mechanics of the impact on spinal cord and the resulting injury [4], [5]. Animal models have proven to be invaluable tools for advancing our knowledge of SCI [3], [6], [7] and unraveling the underlying correlation between injury biomechanics and neurological damage [4], [5]. Nonetheless, employing animal models presents challenges and ethical concerns, which can be partially mitigated by using computational or finite element (FE) models of SCI [5].

Computational models offer a complementary and non-invasive approach for investigating SCI phenomenon [5]. They can provide a detailed approximation of the distribution of loads resulting from the mechanical impact on the spinal cord [5]. In combination with experimental tissue damage data, FE outcomes have been used to study the impact-to-injury link [8], [9], [10]. However, the correlation between these two variables has not been conclusively defined. Properly defining the impact-to-injury link could help quantify the tolerance of the spinal cord tissues to mechanical loading using computational and experimental data [8], [9], [10]. These findings would be a relevant contribution to the field that could allow for the development of better prevention strategies or technologies, improvements of animal injury protocols, and even the creation of new methods for injury prevention.

The correlation between mechanics and tissue damage has been difficult to define. One of the reasons for this are the computational challenges involved in characterizing and modelling the related tissues and structures during a SCI [4], [5]. The effectiveness of FE models of SCI lies in their ability to accurately recreate the experimental behavior and interactions of the spinal cord and surrounding tissues during an injury [4], [5]. Computational models need to recreate these behaviors and interactions, because experimental studies have shown how these interactions influence SCI distribution or severity [4], [5], [11]. If the computational models cannot capture those mechanisms or interactions, it is not possible to rely on the obtained mechanical results. Consequently, it would be difficult to use them in combination with experimental tissue damage data to study the tolerance of the spinal cord tissue to forces and deformations.

One of the interactions that has shown high importance during the SCI process is the protective role of the cerebrospinal fluid (CSF) [12]. Experimental findings on animal models highlighted the contribution of this fluid mitigating spinal cord's compression and damping the impact forces during injury [11], [13], [14]. These findings motivated the study of the importance of including the CSF in computational models of SCI [15], and the biofidelity of different methods to represent it [16]. As a result, more recent FE studies of SCI have included the CSF in their models [9], [17], and implemented new techniques to better capture the biomechanics and fluid behavior of the CSF during SCI, such as smoothed particle hydrodynamics (SPH) [8], [18], [19].

SPH is a method useful for representing solids under large deformations and interactions between solids and fluids [20], [21]. It showed promising results representing the CSF in computational models of brain traumatic injury [22], and it has also been used in FE models of rat [8], non-human primate [18], [19], and human SCI [23]. However, its effectiveness capturing all the reported experimental behaviors of the CSF that contribute to injury has not been explored. For instance, it is known from experimental work that the pressure distribution in the CSF during SCI can influence the severity and distribution of the damage in the spinal cord [13], however it has not been validated if the SPH technique can replicate this behavior. Moreover, the different strategies and boundary conditions used by different researchers to contain the CSF represented with SPH inside their SCI models can also influence the calculated pressure distribution, yet their effect has not been evaluated.

These validations are important since most computational studies of SCI that use the SPH method for modelling the CSF have not reported the pressure in the fluid. Although those FE models successfully predict other mechanical parameters within the experimental observations [8], [18], [19], these models need to be revisited since CSF pressure distribution might affect the predicted tissue-level distribution of loads in the spinal cord [13], [15]. It is important to validate that the SPH implementation and the strategies to contain the CSF in FE models of SCI are not increasing the variability of the mechanical predictions. That could further complicate the validity of the use of FE models to understand the relationship between mechanics and tissue damage.

Motivated by the need to contribute to this growing body of knowledge, this work aims to enhance FE models of SCI by examining the SPH implementation to represent the CSF. The present work will evaluate the biomechanical effect of different CSF containment strategies in FE models of cervical contusion SCI with a preload phase in non-human primates (NHP). Large animal models of SCI, such as NHPs, are more representative of human injuries. As such, achieving a more accurate representation of the complex CSF dynamics within the spinal cord can lead to more accurate predictions of injury patterns and severity. Furthermore, the use of supervised machine learning (ML) techniques will enable the classification of injured elements based on the results obtained from FE models of SCI, providing valuable insights into the identification and characterization of specific damage mechanisms.

1.2. Anatomy of the spinal cord

The spinal cord is a vital structure that runs through the center of the spine, connecting the brain to the rest of the body, and serves as a communication pathway for the transmission of motor and sensory messages [24], [25], [26]. Together, the brain and spinal cord make up the central nervous system (CNS) [27]. The CNS works together with the nerves of the peripheral nervous system to receive, process, and respond to sensory information acquired from the body [26], [28]. The spinal cord is about 43 to 45 cm long [30], and it has a diameter of 1.27 – 1.33 cm in the cervical and lumbar sections [30], and 0.64 – 0.83 cm in the thoracic regions [30] (Figure 1-1). It is encased within approximately two-thirds of the spinal column [31], which provides structure and protection against trauma [25], [26]. The spinal cord extends down the spinal column through the vertebral foramen or spinal canal [25], [28], (Figure 1-1).

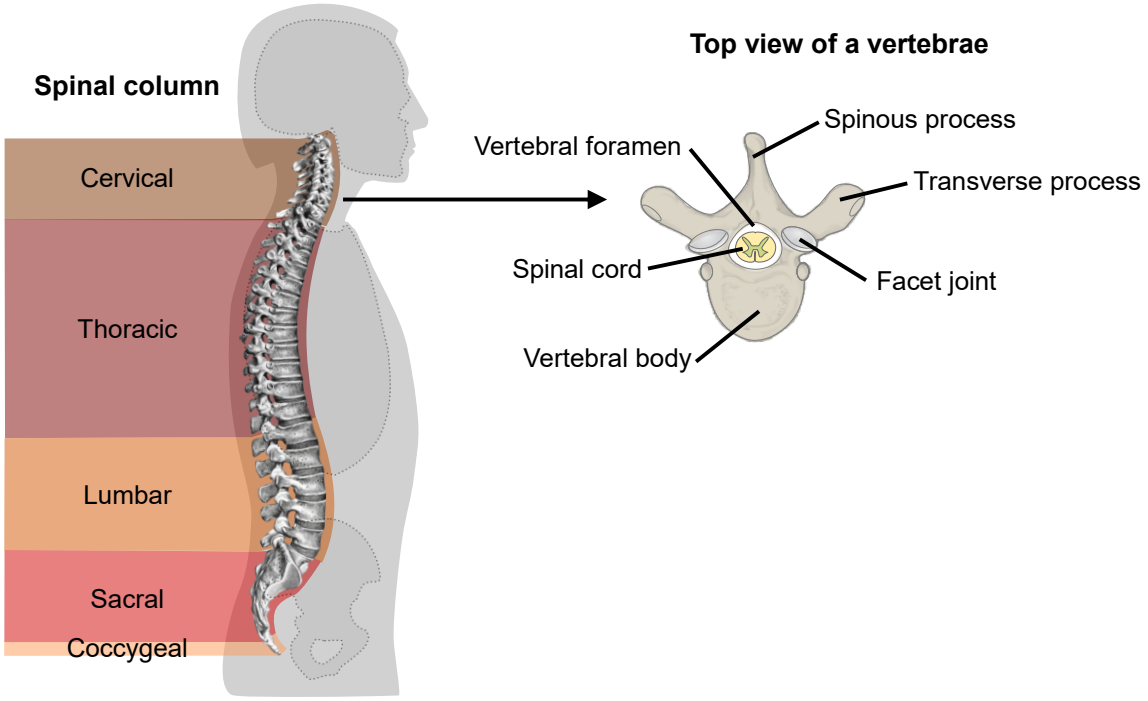

Figure 1-1. Location and organization of the spinal column regions (left), and top view of a vertebrae with its corresponding parts (right). A spinal cord cross section is included to visualize its location with respect to the spinal column vertebras.

The boney spinal column has 33 vertebrae that are divided into five regions (Figure 1-1) cervical (7), thoracic (12), lumbar (5), sacral (5), and coccyx (4) [28]. Each one of the vertebrae are labeled with an initial letter or letters of the spinal region they belong and a number (e.g., C1-C7 for the cervical vertebrae, T1-T12 for the thoracic ones, etc.) [27], [29]. The spinal cord is also divided into levels that are named after the corresponding spinal column sections that house them [31]: cervical, thoracic, lumbar, and sacral. Along the sides of the spinal cord originate 31 consecutive pairs of spinal nerves, that exit the spinal canal in between the vertebrae (Figure 1-2) [27], [28], [31]. These nerves carry motor and sensory information back and forth between the spinal cord and the body [24], [26], [27]. Like the vertebrae, the spinal nerves are also labeled with the initial letter of the spinal cord region they belong to and a number (Figure 1-2) [31].

Each spinal cord level and the corresponding set of nerves control the functions of specific parts of the body [31]. The cervical region controls the upper limbs, head, and neck [32]. The thoracic region governs the chest, abdomen, and back [32]. The lumbar region manages the lower limbs, while the sacral region handles bladder, bowel, and

sexual functions [32]. This division of roles ensures the precise coordination of bodily processes.

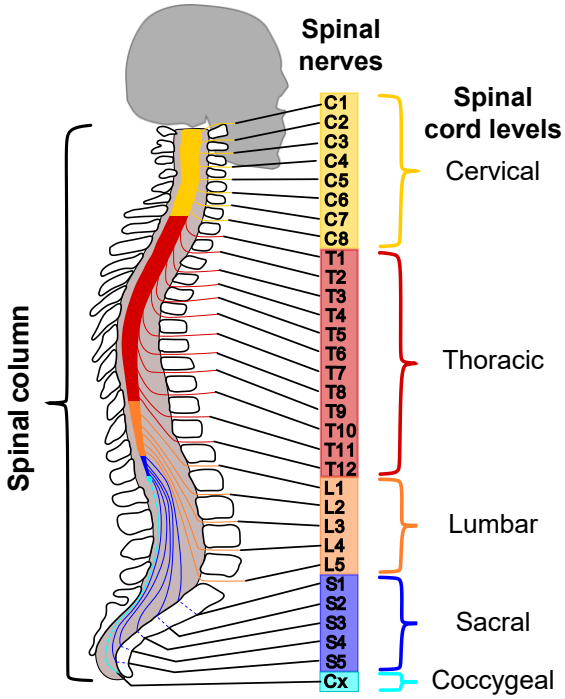

Figure 1-2. Representation of the spinal cord levels and their corresponding pairs of nerves (adapted from [7] - Fig. 3). The spinal cord is located inside the spinal column, and extends along the vertebral foramen or spinal canal.

The spinal cord by itself can be divided into two fundamental tissue types [26], [27], [31]: the inner gray matter (GM), which exhibits a distinctive butterfly or 'H' shape, and the outer white matter (WM) (Figure 1-3). The GM houses neuronal cell bodies responsible for generating motor and sensory signals [27], [33]; additionally, depending on the spinal cord level they are located (i.e., cervical, thoracic, lumbar, or sacral), they also control specific functions for the corresponding parts of the body [31]. Meanwhile, the WM is a tissue that includes ascending and descending axons that run longitudinally along the spinal cord [27], [31], [33]. Depending on the WM area, these can have different densities of axonal fibers, and the axons can also exhibit different diameters that vary between 0.3-20 μm [34]. In combination with the alignment of the axons, the location and different diameters of these fibers provide the WM with a mechanically anisotropic structure [10]. The axonal fibres also facilitate the transmission of signals between neurons located in

the brain or brainstem and those residing within the GM, or between different spinal levels [33].

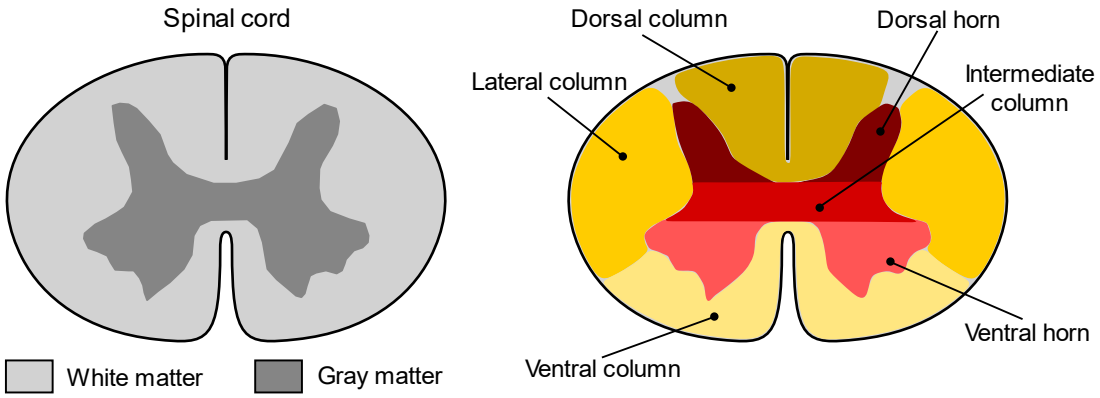

Figure 1-3. Constituent tissues of the spinal cord (left) and individual organization of the gray and white matters at the cervical level (right - adapted from [33] – Fig. 1.11).

Specific functions are carried in different locations of the spinal cord, which can affect the nature of injury. In the case of the GM, the dorsal horns house neurons in charge of receiving and processing sensory information transmitted from the spinal nerves [31], [33], while the ventral horns include motor neurons that connect through the spinal nerves to different muscles [33]. The lateral horns or intermediate column are mostly present in the thoracic region of the spinal cord, and regulate neurons connected to visceral and pelvic organs [31].

The WM is also organized into three columns [33]: dorsal, lateral, and ventral (Figure 1-3). The dorsal column carries sensory information directed to the brain, while the lateral columns may carry both sensory and motor information [33]. Meanwhile, the ventral columns transmit descending motor signals from the brain to the spinal cord [33]. The columns are further subdivided into sets or bundles of axons called tracts (Figure 1-4) [33]. The nerve fibers associated with a tract will usually share characteristics, such as function, origin, and destination in the spinal cord [31]. Tracts are subdivided into two categories: ascending and descending [26], [33]. Ascending tracts are associated with sensory information collected about the external environment through sensory receptors [26], [31], [33], such as temperature, pain, and touch. Descending tracts involve motor neurons that enable voluntary and involuntary movements in muscles, as well as some other autonomic functions [26], [31], [33].

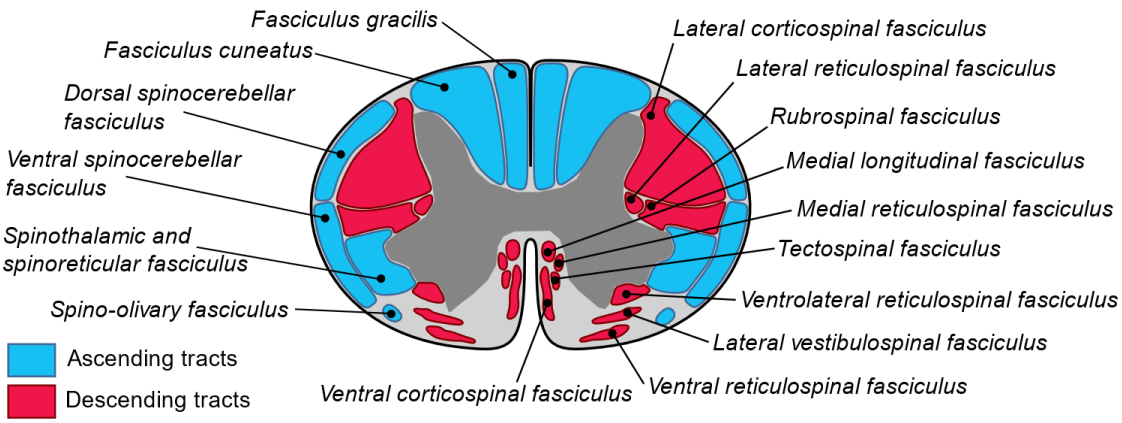

Figure 1-4. Location of the ascending and descending tracts of the WM at the cervical level (figure adapted from [34] – Fig. 1).

Even though each set of tracts covers specific functions, only the functions of the more relevant tracts for this work will be described. The ascending nerve fibers located in the dorsal spinocerebellar fasciculus send signals related to unconscious proprioception; proprioception refers to the perception of joint position, movement, and carried load [35]. Meanwhile, the ventral spinocerebellar fasciculus sends signals on fine and gross movements [36]. The spinoreticular fasciculus controls some motor responses to pain [37]. Finally, the axonal fibers in the spino-olivary fasciculus carry proprioceptive information from tendons and muscles [38], contributing to the control of the body and movement of limbs [37]. For the descending tracts, the lateral corticospinal tracts control voluntary movement of skeletal muscles [36]. Reticulospinal tracts, such as the lateral, ventrolateral, and ventral fasciculus play an important role in posture, balance, and starting limb movements [37]. In the case of the rubrospinal fasciculus, it controls flexor and extensor muscles [36]. Lastly, the lateral vestibulospinal fasciculus conducts signals for controlling movement in the libs and trunk related to posture and balance [37]. As a result of the organization of both ascending and descending tracts in the spinal cord, any medical condition that affects or damages the spinal cord tissue will represent a threat to the body's functions. Depending on the location of the sustained damage, it could interfere with one or more of the sensory and motor functions of a patient.

The spinal cord is surrounded by different layers of tissues called the spinal meninges (Figure 1-5) [28], [31], [39], [40]. The spinal meninges are the pia mater (inner most layer), arachnoid matter (middle layer), and dura mater (outer most layer). The pia mater is a resilient, thin, transparent, and impermeable layer of fibrous tissue that

intimately envelops the spinal cord [40]. The arachnoid mater is a thin intermediary layer, devoid of blood vessels and nerves [41], that lies directly below the dura mater. The outer most meninge, the dura mater, is a robust and thick membrane comprised of a dense matrix of collagen fibres [40]. The dura mater possesses significant strength that helps protect the underlying spinal cord [26], [40], [41]. It also consists of two layers of connective tissue [40], [41]: one of them is attached to the spinal column, while the other adheres to the arachnoid mater. Since both the dura and arachnoid maters are closely attached to each other, the two membranes are often referred to simply as dura [12].

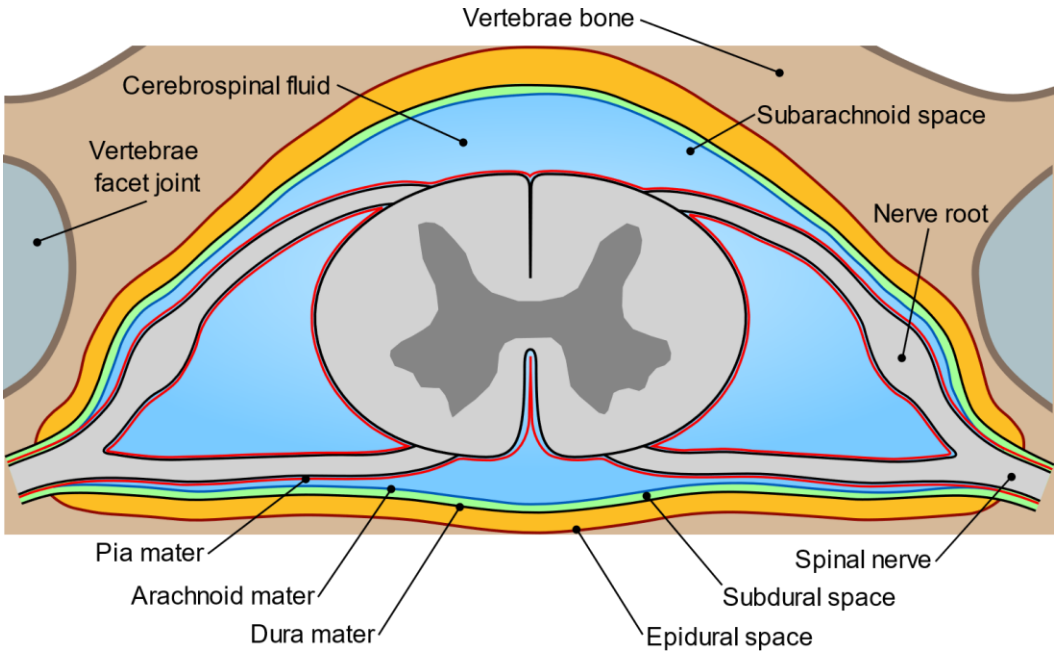

Figure 1-5. Cross-section view of a vetebrae, the spinal cord, and the surrounding meninges. The three spaces (i.e., epidural, subdural, and subarachnoid) are also included, with the epidural space representing the fat deposits that separate the dura mater from the vertebrae bone, and the subarachnoid space containing the CSF.

In between the layers of spinal meninges three potential spaces or cavities can also be found [40], [41]. These spaces, from inner to outer most, are the subarachnoid, subdural, and epidural space [40], [41]. The subarachnoid space, located between the pia and the arachnoid mater, is a continuous cavity that extends along both the brain and the spinal cord [40], [41], and it contains the CSF [39], [40], [41]. The CSF is a clear and colorless fluid that surrounds the brain and spinal cord within the subarachnoid space [42]. It plays an essential role in different physiological functions, such as waste clearance and homeostasis of the CNS environment [43], [44], while also providing buoyancy and

protection [43]. The potential gap or separation between the arachnoid and dura maters is known as the subdural space [40], [41]. Lastly, the space in between the dura mater and the boney surface of the spinal canal is the epidural space [40], [41] . The epidural space contains deposits of fat, blood vessels, and nerve roots [40]. The fat deposits in the epidural space also contribute to protect the spinal cord by acting as a shock absorber [23]. It is important to mention that the subdural space is reported to exist only due to pathological conditions, since otherwise the arachnoid and dura maters are closely attached to each other [40], and it is why this is denominated as a *potential* space.

1.3. Spinal cord injury

Given the vital and numerous motor and sensory functions carried out by the spinal cord, a SCI represents a complex and often life-altering condition with profound implications for the affected individuals [3]. SCI is defined as a damage to the spinal cord tissue that causes impairment to spinal cord function [6]. Depending on the severity and location of the lesion, SCI may cause partial or complete loss of motor and sensory function below the injury level [3]. This type of injury can be caused by traumatic or non-traumatic incidents [6]. Traumatic SCI arises from external physical impact [3], [6], such as the one caused by a vehicle crash, sport, or a fall. Non-traumatic SCI results from acute or chronic pathological processes [6], such as tumors pressing against the spinal cord, or degenerative diseases such as multiple sclerosis.

SCI encompasses primary injury resulting from mechanical trauma to the spinal cord, followed by secondary injury, which involves a cascade of biological events, such as cellular death and structural alterations within the spinal cord, evolving over minutes to weeks after the injury [3], [6], [7]. Primary injury mechanisms include impact plus persistent compression, impact alone with transient compression, distraction, and laceration/transection, all culminating in neurological damage [3]. The secondary injury exacerbates the initial damage, leading to the chronic phase characterized by persistent neurological impairments [3], [6], [7].

In North America, traffic accidents represent the primary cause of traumatic SCI, followed by falls, and sports-related injuries [6]. SCI resulting from high-energy impacts predominate in younger individuals, while low-energy impacts disproportionately affect those over 60 years of age [6]. Injuries at the cervical spine level constitute the majority

(~60%) of traumatic SCIs, followed by thoracic (32%) and lumbo-sacral (9%) injuries [3], [6]. Cervical injuries are also considered the most disruptive type of injury since lesions at this level are often associated with higher mortality rates than thoracic or lumbar injuries [6] and can cause quadriplegia [3].

Despite advances in medical care, individuals with SCI continue to experience neurological deficits and high mortality rates [6]. As a result, SCI inflicts profound physical, social, and professional repercussions on patients and their families [6]. Independence loss and elevated lifelong mortality rates are key consequences of SCI [3], [6]. Additionally, the direct costs associated with SCI care are staggering, reaching up to several million dollars per patient [3], [6], underscoring the urgent need for preventive measures and effective therapeutic interventions [3], [6], [7].

Currently, there are no effective clinical treatments for SCI [7]. This is primarily due to the lack of comprehensive understanding of both the cellular and molecular mechanisms underlying SCI, as well as the biomechanical aspects of the primary injury [4]. Since more than 90% of SCI cases are of traumatic origin [3], unraveling the impact-to-injury link could be paramount for designing prevention strategies that can reduce the impact of SCI on patients and the significant healthcare costs involved [4], [5].

1.3.1. Spinal injury patterns and mechanisms of SCI

Traumatic SCI predominantly arises from interactions between the spinal cord and the vertebral column [4]. When the forces generated by the initial trauma exceed the structural integrity of the hard and soft tissues, their protective capacity for the spinal cord is compromised and can lead to injury [4]. The spine can play a significant role in this process, since structural damage to the vertebrae or to the intervertebral discs can result in different SCI patterns [4]. Experimental and computational injury models to study SCI are often designed to recreate the mechanical conditions of these patterns.

Spinal injury patterns are influenced by several factors. Depending on the impact conditions and the patient's body position before impact, the loading exerted by the traumatic event will transfer specific forces to the vertebrae [4]. These conditions can result in distinct spine/vertebrae damage patterns, which are generally classified as: compression fracture, dislocation (with or without associated fractures), burst fracture, or

distraction [4]. Among these, dislocations and burst fractures are the most common injuries, occurring in 45–58% and 9–35% of cases, respectively [3], [4]. Dislocations typically result from a force inflicted on the spine that generates a transverse displacement of a vertebrae, and results in multiaxial loading on the spinal cord [4] (Figure 1-6 B). Most dislocation cases can be related to a fracture in the vertebrae, which often result in the most severe neurological impairments [4]. Meanwhile, burst fractures are caused by axial loading of a vertebral segment that results in bone fragments being propelled into the spinal canal after an impact (Figure 1-6 C).

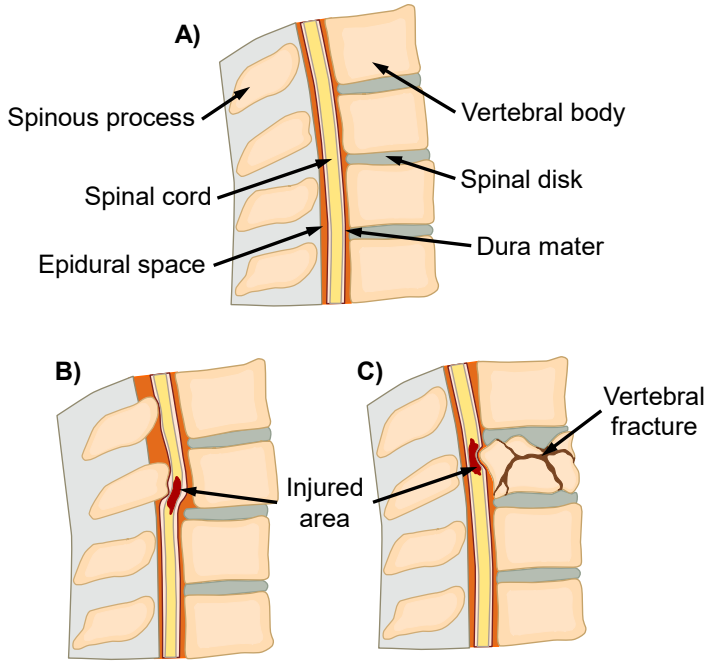

Figure 1-6. Transver plane figure of a section of the cervical spine and spinal cord (A). Representation of the two most common types of spinal injury patterns: dislocation (B) and burst fracture (C).

From these spinal injury patterns, it is possible to define three main mechanisms responsible for SCI [4], [12]: blunt or contusive, stretch or distractive, and laceration-type injuries. Contusion injuries often stemmed from burst fractures and fracture dislocations [12]. On the other hand, distractive injuries are related to less common injury patterns [12], such as axial distraction, or SCIs without apparent radiographic abnormalities or trauma evidence, also known as SCIWORA-ET. Lastly, laceration-type injuries are related to penetrating SCI caused by foreign objects or projectiles [4], [12].

1.4. Models of SCI

There are two main approaches for modeling SCI: 1) animal models of SCI, that offer insights into the physiological and biomechanical responses to injury within living systems, as well as a platform for testing potential treatments, and 2) computational models, which serve as non-invasive tools for simulating and analyzing the complex mechanics of SCI. These models have contributed to the foundation of the current knowledge of SCI and have propelled the development of potential therapeutic strategies [4], [5].

1.4.1. Animal models of SCI

SCI research heavily relies on animal models. These models have significantly contributed to our understanding of physiological and biological responses to SCI and have facilitated preclinical testing of potential therapies [3], [6], [7]. Animal models have also greatly contributed to the study of SCI biomechanics, since they provide an experimental platform where it is possible to control the input parameters leading to injury [4]. In such models, characteristics of a SCI and the potential treatment strategies are examined by generating a controlled injury in the animals. Generating repeatable and consistent injury that results in consistent neurological and functional deficits in the spinal cord is vital to further study SCI pathophysiology [4] or the effectiveness of potential treatments [6].

Currently, there are many different animal models available. However, given the reported heterogeneity of SCI in the human population [3], there is no single animal model that can address all the specific questions in SCI research [4]. Therefore, there are different considerations that need to be included when selecting an animal model. These considerations include the type and location of the SCI, anatomical and pathophysiological differences in comparison with humans, possible outcome measurements, and the animal species [3]. In addition, researchers suggest that the animal model should require minimal animal training, be cost-effective, and provide consistent results [6]. Among animal models, rats are the most widely used for SCI research, since they provide important advantages, such as cost-effectiveness, reduced ethical implications, accessibility, ease of care, and the availability of well-established functional analysis techniques [3], [6], [7]. Studies on rats have shown they closely mimic several pathophysiological,

electrophysiological, and functional features of human SCI [3], [6]. Moreover, histological assessments in rats have shown a strong correlation between spared WM and functional preservation following injury, indicating their suitability for evaluating the benefits of therapeutic strategies for SCI [3].

While all these characteristics have made rat models widely used in SCI research, direct translation of their findings to human SCI has been challenging due to the inherent anatomical and morphological differences [3], [6]. As a result, there has been an increase in the use of large animal models, such as pigs and NHPs, that offer a closer resemblance in terms of size, neuroanatomy, and physiology to humans [3], [7]. These models are particularly important for intermediate-stage research, where it is possible to confirm results obtained from rodents and provide relevant safety, biodistribution, and technical feasibility data before transitioning to human trials [3], [6], [7]. Despite their advantages, limitations such as higher costs, ethical concerns, smaller sample sizes, and the need for specialized facilities limits the use of large animal models in SCI research [3], [6], [7].

Some of the most common large animal models use a controlled impact to the dorsal surface of the spinal cord, after the vertebral lamina is removed, to generate an injury [45], [46], [47]. There are two different approaches for controlling the impact 1) a “weight-drop” device, that generates an injury by dropping a weight from a specific height on the spinal cord [4], and, 2) a contusion model that uses a displacement controlled linear actuator to prescribe the impact. Two examples of large animal models with these approaches are particularly important for the work presented in this document. The first one is a porcine model of thoracic SCI, developed by Lee and colleagues [45], and the second one is a model of unilateral cervical spinal cord contusion injury in NHP developed by Salegio and coworkers [47]. The porcine model by Lee et al. was proposed as an alternative to small animal models, such as rodent, where the considerable difference in spinal cord size with respect to humans could affect the outcomes after the distribution of pharmacological, structural, or cellular-based treatments. At the same time, this model was also presented as a suitable alternative for other large animal models, such as primate models, that are closer anatomically to humans, but involve greater costs, and ethical, and logistical complications [45]. This weight-drop model was fundamental for the work of Jones et al. [12] assessing CSF mechanics during SCI. On the other hand, the contusion model described in [47] by Salegio et al. was proposed for the study of the impact-to-injury link, and behavioral outcomes on NHPs. NHPs are one of the closest representations to

humans available in SCI research [47], [48], so it was expected to use this model as a platform to test the efficacy and safety of potential treatments before moving into human trials.

1.4.2. Computational models of SCI

Quantifying the internal distribution of forces and deformations could be key for understanding the mechanisms that lead to SCIs and developing effective diagnosis and treatment [4], [8], [18]. As a result, computational models, specifically FE models, have emerged as powerful tools for understanding the mechanics of injury in SCI research. FE models offer a novel approach to investigating the mechanical intricacies of spinal injuries and their consequences [4], [5]. Validated computational models grant researchers the ability to manipulate critical variables such as impact conditions, geometry, and tissue properties, allowing for a detailed examination of their impact-to-injury link [4], [5], [18]. This versatility is particularly advantageous, as it circumvents the ethical and logistical challenges associated with animal studies while saving time and resources [4], [5].

Computational models need to be properly validated against experimental data to ensure they provide accurate information regarding the SCI process [4], [5], [49]. The validation, however, rely heavily on experimental data to define the mechanical properties of each tissue in the structure involved [4], [5]. This validation has been particularly challenging when building human FE models of SCI, where the lack of *in vivo* data prevents researchers from defining biofidelic material properties [5]. As a result, experimental data from animal models is often used to develop the material models that are included in FE models of SCI [5], [49].

There are different types of FE models of SCI. Some models are based on humans and try to recreate clinical injury scenarios [50], [51], [52], [53], while others are based on animal models and try to recreate controlled injury experiments [8], [9], [17], [18], [54], [55]. For the scope of this thesis, we will focus on FE models of SCI that recreate controlled experiments on animals, since these experimental results make it possible to validate the accuracy of the FE model. In exchange, FE models provide a non-invasive platform to test potential changes to the injury protocol executed in animal subjects, or the opportunity for additional analysis of the experiments without the need for additional animals.

FE models have captured *in vivo* animal experiments and *in vitro* benchtop studies. For example, Maikos and colleagues [9] built an FE model to simulate a weight-drop experiment in rat spinal cord and found that changes in the defined instantaneous shear modulus for the spinal cord had affected the impactor's predicted displacement. Additionally, they found that using different mechanical properties for the gray and white matter significantly changed the stress and strain patters in their model, while predicting similar weight-drop displacements. Persson et al. [15], [56] also created a computational model of SCI based on *in vitro* transverse impacts on bovine spinal cords to first investigate the importance of including the CSF in computational models of SCI [15], and then to study the effect of CSF thickness on the spinal cord's deformation during injury [56]. Their findings pointed out that it was important to include both the CSF and dura mater in FE models of SCI, since both structures play an important role in reducing strains in the cord [15]. In addition, they reported that thicker layers of CSF resulted in lower levels of spinal cord compression, and reduced levels of stresses and strains in the tissue [56]. Russel et al. [8] also presented the results from a contusion and dislocation FE model of rat cervical SCI, where they looked at the impact-to-injuy link in the spinal cord. Based on the maximum principal strain values of the FE model, their analysis suggested a lower tolerance in the GM to strain than in the WM.

Using experimental data from *in vivo* cervical contusion experiments in non-human primates, Sparrey et al. [17] built an FE model to investigate and refine the impact parameters of the contusion experiments. The data presented in their paper indicated the importance of defining the impactor's alignment with respect to the midline of the spinal cord, as well as the pre-load exerted to the it before impact, so it is possible to generate mild injuries in the subjects. Fournely and colleagues [55] developed an FE model to investigate the effect of morphological and mechanical factors in a mouse contusion model, where they concluded that the assigned material properties to the spinal cord and the impactor's alignment were the most influential variables in the predicted strain outcomes. Later, Jannesar and co-workers [18] created both simplified and subject-specific FE models of cervical contusion in NHPs and used the results to assess the impact-to-injury link in NHP spinal cord. They concluded that certain mechanical measures including, maximum and minimum principal strains, Von Mises stress and Tresca stress, strongly correlate with tissue damage in the gray and white matters. Their data also showed the subject-specificity of the predicted damage thresholds. More recently, Obaid

et al. [19] presented a study where simplified FE models of cervical contusion in NHPs were used to explore the effect of intersubject variability in the mechanical outcomes of the experiments. The findings reported in their paper showed that variability in the reaction force outcomes of the simulations and the spinal cord slippage during the impact were reduced by tuning the impactor diameter and mediolateral alignment of the impactor.

Despite the described progress, there are several different challenges that persist in the development of more reliable FE models of SCI. For example, the level of detail in the geometries and structures included in computational models of SCI ranges greatly between studies. Some studies have used a combination of imaging technologies, such as magnetic resonance imaging (MRI) or CT scans, and software packages to generate specific geometries [8], [9], [18], [55], while other studies have approximated their models using experimental measurements [15], [17], [19], [57]. Moreover, depending on the computational resources available, it has not always been possible for researchers to include all the relevant tissues, nor to use the best methods to represent some of these anatomical structures, such as the CSF that was often omitted or simplified [9], [17], [55]. Additionally, for some of the spinal tissues there is a wide range of material properties available, and there has not been a consensus on which ones are more suitable for recreating certain experiments [5]. At the same time, there are other tissues that have been difficult to characterize, so there is limited information regarding their mechanical properties [5], [49]. These challenges complicate the interpretation and comparison of results in this emerging field of research; however, they also open the door for new research avenues to address these challenges.

1.5. Cerebrospinal fluid's role in SCI

1.5.1. Characteristics and functions of the CSF

The CSF is composed of 99% water, and 1% of proteins, ions, and neurotransmitters [58]. Being a water-based fluid, the CSF is a Newtonian fluid [59], [60], [61], meaning that its viscosity will remain constant regardless of the shear forces acting upon it. It has a similar density to water (~1000 kg/m^3) and a viscosity of approximately 0.7 to 1 $mPa \times s$ [61], [62]. The CSF circulates through the subarachnoid space, providing essential nutrients and removing waste from the CNS [43]. CSF circulation is facilitated by the constant production and absorption of this fluid [43], which helps maintaining

homeostasis for the CNS environment. On average, an adult man will have a CSF circulating volume of approximately 150 mL [43], [44], [63].

Normal values of CSF pressure range between 1 - 2 kPa (10-15 mmHg) for human adults, with lower values for children and infants [44], [63]. The CSF pressure is in constant fluctuation, meaning that the usual reported CSF pressure is the mean value of those fluctuations [12]. The fluctuations are derived from a constantly shifting balance between the production, absorption, and flow resistance of CSF in the body. The fluctuations are also related to factors such as vascular pressures, activity of the sympathetic nervous system, elasticity of the dura-arachnoid complex, etc. [12], [44], [64]. These factors make the CSF pressure susceptible to changes related to everyday activities, such as breath holding or coughing, or clinical procedures that change intra-abdominal pressure [12].

Among its functions, the CSF offers mechanical protection, nourishment, and waste elimination to the spinal cord and the rest of the CNS [43], [44], [63]. The CSF manages to protect the brain and spinal cord through two mechanisms: firstly, it acts as a shock absorber, preventing direct contact between these structures and the skull or the spinal column [43], [63]; and secondly, the CSF provides buoyancy for the brain and spinal cord, helping reduce the forces exerted on them during mechanical impacts [43], [63].

1.5.2. Biomechanical effect of the CSF during SCI

The biomechanical effects of the CSF during SCI are a subject of increasing interest in the SCI scientific community. One of the principal functions of the CSF is to act as a shock absorber for mechanical forces directed to the spinal cord [43], [63], and studies such as those conducted by Jones et al. [11], [13] and Persson et al. [15], [56], have delved into the effect of this CSF function during SCI. Their findings suggested that the CSF, along with other surrounding tissues that envelop the spinal cord, plays a pivotal role in mitigating the impact forces associated with SCI. Altogether, they reduce the compression exerted on the cord's tissue. These findings indicate that the CSF influences the severity and extent of SCI.

The CSF, and the neighboring tissues, provide a damping effect for the spinal cord [26], [40], [43]. The CSF is capable of dissipating or attenuating the forces and the pressure wave generated by the mechanical impact experienced during an injury [12],

[13], [65] by absorbing some of the impact's energy and spreading it out over a larger area. With this attenuation of the impact forces, the CSF also contributes to reducing the spinal cord's compression during injury, which can result in lesser damage to the neurological tissue [11], [14], [56].

At the same time, studies have found that the biomechanical effects of the CSF are closely related to the thickness of the CSF layer around the spinal cord [56]. Increasing dimensions of the CSF layer tend to decrease the peak impact load and the cord's compression during injury [56]. These findings highlight the importance of incorporating the CSF into both computational and experimental models used for studying SCI biomechanics and validating the size of the included CSF layer. Moreover, these observations provide a plausible explanation for the variability found in the biomechanical results of different animal models. Significant interspecies variability of the morphology and dimensions of the spinal cord and CSF layer thickness has been reported in large animal models [57], [66], [67], and these variations can significantly affect their biomechanical response to a similar impact [9], [12], [56], [65].

Alternatively, researchers also have discovered that the CSF may play a negative role in extending the damage near the injury site [13]. There is a possibility that the resulting pressure transient in the CSF contributes to further damage in the cord's tissue, primarily due to an increase in CSF pressure in the vicinity of the impact location [13]. This effect appears to diminish in spinal cord sections further away from the injury epicenter [13]; still, it should be taken into consideration for the development of more biofidelic computational and experimental models of SCI [12].

1.5.3. Representations of CSF in computational models

One of the principal challenges in the development of accurate FE models of SCI has been the inclusion of the CSF. Different experimental models have shown the effect of CSF in the severity and distribution of SCI [11], [65]. They have also highlighted the importance of including it in FE models to improve the biofidelity of their results [15], [56]. Still, due to limitations in computational resources, previous FE studies of SCI have not included the CSF [52], [55], [68] or have used solid elements with elastic or hyperelastic material properties to represent the CSF [9], [17]. While these are valid approaches, studies on head impact FE models, such as Duckworth et al. [22] and Chafi et al. [69]

found that elastic or hyperelastic solid representations of the CSF were not able to properly capture the strain distribution and relative displacement of the brain observed during experiments. The limitations of the solid CSF representations found by Duckworth et al. and Chafi et al. could have similar effects in computational models of SCI. Motivated by these observations, more detailed FE models of SCI have been developed using fluid-structure interactions (FSI) to model the CSF [8], [15], [16], [18], [23].

FSI are computational methods used to simulate scenarios where there is an interaction between different structures and a fluid [70], [71]. FSI help to couple both the solid mechanics and fluid dynamics in the analysis [70], [71], which makes them a suitable tool for SCI models involving CSF. Persson and colleagues [15] were one of the first groups to highlight the importance of implementing an FSI method for representing the CSF in FE simulations of SCI. In Persson's work [15], they followed a FSI approach by Zhang et al. [72] where the fluid was modelled using an arbitrary Lagrangian-Eulerian (ALE) mesh. An ALE mesh combines aspects of two common types of meshes used in FE models [73], [74]: Lagrangian and Eulerian. In general terms, a Lagrangian mesh is attached to a body or geometry and will move or deform with the body [73], [74]. The previously mentioned elastic and hyperelastic solid representations of the CSF [9], [17] would be implementation examples of a Lagrangian mesh. In contrast, an Eulerian mesh is fixed in space, and the body or geometry moves through the mesh as it deforms [73], [74]. An ALE mesh integrates aspects of both Lagrangian and Eulerian meshes, which allows for the mesh to move and deform with the evaluated body, while also providing a fixed reference frame for the analysis [73]. These characteristics of an ALE mesh make it a suitable approach for modelling fluids [73], [75], [76], and it helps circumvent some of the individual limitations of Lagrangian and Eulerian meshes [73], [74], such as excessive mesh distortion, limited accuracy, and computational cost.

Later FE models of SCI continued to use FSI methods to model the CSF in their simulations [8], [18], [19]. For instance, in their model of rat cervical SCI to study the correlation between strain and tissue damage, Russell and colleagues [8] proposed the use of SPH for representing the CSF. SPH is a Lagrangian method characteristic for representing a continuum body as a set of particles [21]. Unlike regular Lagrangian or Eulerian approaches, SPH is a mesh-free method, which means that it does not rely on a fixed mesh in the evaluated body or in the simulation space to compute the displacement or deformations of a body [20], [21]. Instead, SPH calculates the displacement or

deformations using the particles' location, which allows it to efficiently simulate scenarios with large deformations and fluid-like behaviors [20], [21]. As a result of the favorable outcomes acquired by Russell and coworkers using SPH in their simulations, they suggested that this method could be further applied in SCI models of large animals or humans, where the CSF represents a larger volume than in rats [8]. Accordingly, Jannesar et al. [18] and Obaid et al. [19] would later use SPH for modeling the CSF in their FE models of SCI in NHPs, while researchers such as Arhiptsov et al. [23] would include it in their models of human SCI.

More recently, noting the implementation of different FSI in FE models of SCI, Rycman and collegues [16] undertook the task of comparing the accuracy and efficiency of different representations of the CSF. Rycman et al. [16] compared four FSI methods reported in the literature to have been included in FE models of SCI, starting with: pressurized volume. This method was reported in an FE model of human cervical spinal cord [77], and it works by modelling a fluid's volume as a pressurized cavity that exerts the pressure on the surrounding instances of the model [77]. The other three methods were: traditional Lagrangian mesh, ALE mesh, and SPH, that have been previously explained in this section. Each FSI technique was tested in an FE model of spinal cord transverse impact and compared against *ex vivo* data from bovine experiments. The assessment indicated that, within the four evaluated approaches, SPH was the most computationally efficient, and suitable method for capturing CSF behavior in FE models of spinal cord transverse impact. The promising results and relative consensus of different researchers on the implementation of SPH to represent the CSF in FE models of SCI further motivates its exploration in this document.

Overview of the SPH method

SPH is a meshless or mesh-free FE implementation method [20], [21]. Contrary to traditional FE analysis, where Lagrangian or Eulerian approaches are used to represent a continuum body, in SPH modelling, the body is represented by a collection of points or particles that are not fixed in space [20], [21] (Figure 1-7). The method has been broadly used for different engineering applications, particularly the ones involving extreme deformations [78], [79], fractures [80], [81], and fluid motion. This last characteristic makes SPH an option for addressing problems involving fluid-structure interactions, which has researchers implementing it for the study of human injuries. Particularly in the case of

traumatic brain injury or SCI, where the impact-to-injury link involves interactions between tissues and CSF [8], [16], [18], [22].

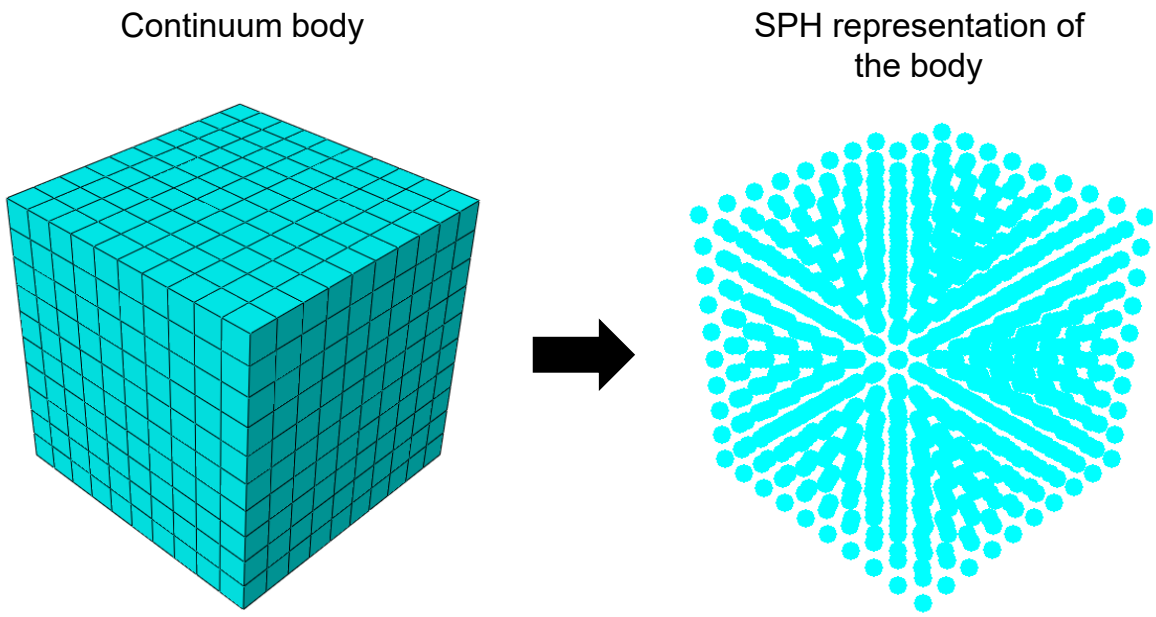

Figure 1-7. Example of a continuum body and its equivalent representation using SPH.

It is important to understand the underlying mathematical principles behind the SPH method to properly implement it in commercial FE software. SPH works by approximating the particle's value of an estimated property (e.g., displacement, velocity, etc.) by considering the estimated values of the same property in the surrounding particles [20], [21]. The surrounding or neighbor particles to be considered are defined by a kernel function, that assigns a contribution weight to each particle, based on distance with respect to the particle of interest. Mathematically, this is represented with the following equation [20], [21], [82]:

$$A(r) = \Sigma_j \frac{m_j}{\rho_j} A_j W\left(\left|r - r_j\right|, h\right) \qquad (1)$$

Where $A(r)$ represents the smoothed estimate or the property being estimated, r is the position of the particle of interest, and j is the subscript for neighbor particles. Meanwhile, m and ρ are the mass and density, respectively, A_j represents the estimate function at particle j, W denotes the kernel function that depends on the relative position $\left|r - r_j\right|$ and the h parameter, also know as the smoothing length. The smoothing length

defines the radius of the kernel function, helping determine how many particles participate in the interpolation [21], [82].

In other words, Eq. 1 states that the estimated value of the property A at the particle r will be equal to the sum of the contributions from all the nearby particles, indexed by the j subscript, and resulting from the product of their volume, V_j, since we know that $V_j = \frac{m_j}{\rho_j}$, the property A_j of each particle, and a weighting factor. The weighting factor is determined by the kernel function W, that depends on the relative position between the particle of interest and the neighbouring ones ($|r - r_j|$), and the smoothing length.

Currently, different FE software packages allow for the implementation of SPH. Although they followed similar principles for calculating the particles' values during a mechanical simulation, the requested parameters, and the procedure to implement the method might defer between software [20], [21], [86]. In this thesis the relevant aspects of the implementation of SPH in ABAQUS will be described.

SPH implementation in ABAQUS

ABAQUS, from Dassault Systemés, is one of the commercially available software for performing FE analysis. It provides different capabilities [87], such as an extensive material's library, coupled stress analysis, simulation of non-linear responses, and efficient use of computational resources. Those capabilities have shown potential to solve engineering problems related to mechanics and biomedical problems. Given the non-linear nature of the tissues and structures involved in SCI and the complex set of interactions between them, ABAQUS is a suitable tool for building and simulating models of SCI. FE models of SCI inspired in both animals and humans have already been developed and studied using this software [8], [9], [17], [18], [19], and their results have shown strong capabilities at recreating *in vitro* and *in vivo* SCI experiments.

ABAQUS also allows for the implementation of SPH [21], method that has shown promise to represent the CSF in computational models of SCI [8], [16], [18], through two different workflows that will be briefly discussed. In previous versions of ABAQUS, SPH could only be defined manually through the modification of the input file from the model of interest [21]. An input file is a script file generated by FE software to include the commands associated with the model and analysis defined in the computer interface. This input file

method requires the user to manually define the elements to be converted into particles, and the value of some important parameters for calculating the particles' volume, such as the characteristic length [21]. Other SPH settings, such as the artificial viscosity, tensile instability control, smoothing length calculation, SPH kernel and formulation, and analyzed domains can also be changed through the input file modification. In newer versions of the ABAQUS software (2020 and on), the computer-aided environment (CAE) allows for the definition of SPH without having to modify the simulations' input file [21], [88]. In this workflow, the user can activate the "particle conversion" option during the meshing of a part, which allows the solid mesh to convert into SPH particles during the analysis. Contrary to the input file method, this approach does not request for a manual definition of parameters, such as the characteristic length or a surface for the particles, since ABAQUS will automatically calculate or define them. However, this approach asks for the definition of other parameters, such as the interpolation kernel for computing the particles' outcomes, the number of particles per element, and to define a time, stress, or strain threshold that will trigger the particle conversion. More explicit details and resources on the two SPH implementation methods in FE analysis can be found in the ABAQUS documentation manual [21], [88].

It is important to consider the differences between the requested parameters in these two approaches, particularly when recreating earlier work involving SPH in more recent versions of ABAQUS. Properly translating the parameters from the input method to the CAE one or the other way around would allow to replicate the results, since regardless of the SPH workflow, the calculation of the mechanical values in the particles is the same [21]. The CAE method to define SPH in ABAQUS facilitates the calculation of the characteristic length of the particles, and the reduced number of steps needed to define it minimizes the possible sources of mistakes in comparison with the input file modification. Accordingly, SPH was implemented in the FE models of this thesis using the CAE approach, and more details of the defined values for the requested parameters are included in following sections.

1.6. Impact-to-injury link in SCI

It is well-established that the primary injury mechanisms are closely linked to the damage inflicted on spinal cord tissue [3], [4], [5]. To explore these mechanisms and the impact-to-injury link, animal models have proven invaluable under controlled conditions

[3], [4], [5]. However, relying exclusively on animal models poses limitations, since they cannot provide insights into the tissue-level distribution of forces and deformations within the spinal cord [4], [8], [18]. In addressing this gap, computational models emerge as complementary tools that can enhance our understanding of the intricate impact-to-injury link [4], [5], [49]. This not only allows for discerning the correlations between variables, it also provides some of the means to quantify them and define mechanical failure thresholds for spinal cord tissues [8], [9], [18]. Such advancements would represent significant progress towards developing more effective injury protocols, designing better protective equipment, and using SCI FE outcomes to predict injury severity and pinpoint injury locations [8], [17], [18], [19], [49]. To this end, supervised ML algorithms could be an important complementary tool for FE models of SCI, since recent studies have shown their suitability for using FE data for different mechanical applications, such as prediction of material properties [89], identification of damage in structures [90], vibration modal analysis [91], and prediction of bone fracture [92]. These implementations of ML algorithms motivate its integration to SCI workflow, as this tool could potentially help to better understand the impact-to-injury link in SCI.

1.6.1. Relevant findings from SCI studies

Both animal and computational models come with specific constraints that limit the information they can provide to researchers. Combining the findings from both approaches could contribute to a wider overview of the problem. Computational models of SCI can provide detailed information about the loading distribution in the spinal cord tissues and meninges [4], [5], [8], [9]. However, they lack the means to define the level of damage sustained by the tissues or the effect it will have in their functional outcomes. Experimental data from animal models can provide this information, and using the appropriate data processing tools, it could be possible to combine both sources of information for correlating the tissue-level mechanical outcomes with the observed tissue damage. Previous studies have already used this approach to complement the results from computational models with histopathology data [93] from SCI experiments [8], [9], [18].

Maikos et al. [9], simulated a weight-drop SCI experiment in rats, they used a logistic regression analysis to match the maximum principal strain distributions found in the computational models with tissue damage patterns in the gray and white matter collected from parallel *in vivo* studies. They did this by generating images of horizontal

slices of the spinal cord and identifying the injured areas and overlapping them against corresponding slices of the FE model. The elements located inside injured areas were labeled and their values of maximum principal strain calculated by the FE model were identified. Using logistic regression, their analysis showed that maximum principal strain was correlated to damage in both constituent tissues of the spinal cord, with a stronger level of correlation with the GM than the WM.

A similar approach was presented by Russell et al. [8], by investigating the correlation between maximum principal strain and tissue damage in FE models of contusion and dislocation SCI. Tissue damage data were collected from the experimental procedures they were trying to recreate, and the strain values of the elements in the computational models that matched the injured areas were identified. Their correlation analysis was performed with a linear regression model, with the outcomes suggesting a stronger correlation between strain and tissue damage in the contusion scenario. In this study, GM sections also showed a stronger correlation with strain values. However, those results could have been affected by the limited injury data available from the GM due to technical challenges.

Even though their methodology did not include the use of FE models, the study presented by Bhatnagar and coworkers [94] also correlated tissue-level strains with damage exclusively in the GM in an *in vivo* rat contusion model. The strain measurements were collected using a combination of magnetic resonance technology and image registration methods during the injury experiments, and the tissue damage data originated from a histological analysis done to spinal cord samples collected post-injury. The observations from their linear regression analysis pointed out that different injured regions of the gray matter were correlated with different types of strain. However, the strongest correlation found was between minimum principal strain and the damage located in the ventral horns of the GM.

Jannesar and colleagues [18] built subject-specific FE models from MRI scans taken from non-human primate subjects and used them to recreate the contusion SCI experiments done in the animals. One-element thick cross-section of the FE models were overlapped against images of the histological results taken from spinal cord tissue samples, and the elements were labeled depending on their location with respect to the injured areas. Using logistic regression, the correlation between the mechanical

parameters and the damage in the spinal cord were studied. Jannesar et al. [18], also found a stronger correlation between the mechanical parameters and the damage in the GM than in the WM, particularly for strain values. They also calculated injury threshold values for the mechanical measures using the inverse prediction method, which allowed them to report the threshold values of stress and strain after which the spinal cord tissues would be injured.

These studies showed the utility of computational models along with histological data to determine how the mechanical parameters are relevant indicators of injury in the spinal cord tissue. Moreover, their results also suggest the potential of these approaches for the definition of injury thresholds, as proposed in [18], which would allow for the development and validation of prevention or protective technologies that can help minimize the mechanical forces under the defined thresholds.

1.6.2. Machine learning applications in FE studies

In recent years, artificial intelligence (AI) and its corresponding subcategories, such as ML, have become increasingly employed in different research and engineering fields [89], [90], [95], [96], [97], including biomedicine [95], [96], [97], [98], [99], [100], [101]. In areas such as mechanical or materials engineering, where there are available tools for studying complex systems or simulating physical phenomena, such as FE models, ML has opened the possibilities for either substituting [89], [102] or complementing [90], [91], [92] these tools in certain scenarios. The surging interest of the research community to implement ML algorithms alongside FE analysis originates from the capabilities shown by ML in problems involving large amounts of variables, uncertainty, and inconsistent behaviors [103], [104]. It is expected that these capabilities could circumvent some of the limitations of traditional FE analysis, such as the computational costs or the interpretation of results.

ML covers a large spectrum of methods and techniques. For the scope of this work, only the integration of supervised ML algorithms with FE models are investigated. Supervised ML models learn and generalize from existing information, making them particularly well-suited for tasks such as classification, regression, and pattern recognition [103]. The main difference between supervised ML algorithms and other branches of ML, such as unsupervised ML, resides in the use of previously labeled data for its training

process [103]. A relevant example of the applications of supervised ML algorithms and FE models is the work by Pathan and colleagues [89]. Pathan et al. [89] presented a study where a supervised ML algorithm was used to predict the mechanical properties of fibre composites and the predictions were compared against the FE models of the composites microstructure under loading. The training data for algorithm were generated by running FE simulations of different composite microstructures under three loading cases. After training, the prediction capabilities of the algorithm were tested and compared against additional FE simulations, where the results showed that the ML algorithm had a margin of error no greater than 5% in predicting the mechanical properties of the composite structures. Based on their findings, Pathan et al. [89] concluded that combining FE models and ML algorithms provided a reliable and inexpensive procedure for estimating the mechanical properties of composite microstructures.

Other examples are Abedin et al. [90] and Castro et al. [91] work using ML algorithms for damage detection in bridges and structural vibration problems in ships. Abedin and coworkers [90] performed a series of static and dynamic loading tests on a bridge with some level of damage and measured the deflections in different sections of the bridge. Then, built a detailed FE model of the bridge and simulated different damage scenarios. Three ML models were trained using the experimental and computational deflection measurements and used to predict the damage in a separate bridge scenario, also simulated using FE. The results indicated that the algorithms were capable of accurately finding the location and amount of damage of the bridge. Meanwhile, Castro et al. [91] proposed the use of supervised ML to correlate the experimental and computational modal shapes of a catamaran ship. This approach proved to be effective for correlating the modal shapes of the ship, and Castro and colleagues also reported that including ML provided the advantage of identifying the most relevant input parameters of this vibration problem.

In the field of biomedicine, the work done by Villamor et al. [92] exploited the two computational tools (i.e., FE models and ML algorithms) for the prediction of osteoporotic hip fracture in women. They generated patient-specific FE models based on scans of patients with and without hip fracture and used them to simulate a sideways-fall. The mechanical outcomes of the FE simulations were used in combination with clinical data of the patients to create a dataset. This dataset was used for training four supervised ML algorithms to identify hip fracture in patients based on the provided mechanical and clinical

attributes. Their results showed that using this combined approach provided better results at identifying hip fracture than the usual gold-standard, and that including the FE-related attributes improve the fracture identification.

The previously described findings suggest that combining the capabilities of FE analysis and supervised ML algorithms can be beneficial for the study of complex problems in different fields. The work by Villamor et al. [92] showcases the use of these two tools, FE and ML, for a problem similar in nature to the study of the correlation between mechanical outcomes of FE models and tissue damage in the spinal cord. In both cases, FE models are generated to recreate an injury process, from where it is possible to request the values of different mechanical attributes, and it is also possible to assign the generated samples into injured and non-injured classes, thanks to clinical or experimental data available. Consequently, the results by Villamor et al. motivate the exploration of including supervised ML algorithm for the study of impact-to-injury link in SCI, and it will be discussed further in later sections of this document.

1.6.3. Supervised ML algorithms

As discussed in previous sections, the analysis of complex mechanical data derived from FE models of SCI presents challenges, particularly when complemented with experimental injury data. In this context, supervised ML algorithms emerge as valuable tools, offering a systematic and data-driven approach to discern subtle patterns and relationships [103] between the mechanical outcomes of FE models and experimental injury data [105]. The following sections explore the general aspects of four supervised ML algorithms: logistic regression, decision trees, support vector machines, and k-nearest neighbors, that were selected to explore their classification capabilities to enhance our understanding of impact-to-injury link in SCI.

Logistic regression

Logistic regression (LR) is a statistical and supervised ML algorithm that is particularly well-suited for scenarios where the goal is to predict a binary outcome [98], [99], [103], [106]. This method specializes in binary classification tasks, where the dependent variable, usually denoted as Y, can only assume binary values that correspond to the absence (0) or presence (1) of a particular event or attribute [98], [99]. For example, in an email filter, Y might represent whether an email is spam (1) or not (0).

Logistic regression uses of a logistic function, often referred to as the sigmoid function [106], for the prediction or classification tasks:

$$P(Y = 1 \mid X) = \frac{1}{1+e^{-Z}} \qquad (2)$$

In the previous equation, $P(Y = 1|X)$ represents the probability of the dependent variable Y to be a positive case (1) of the event or attribute that it's been studied [106]. The term Z denotes a linear combination of the input features, or independent variables, and their corresponding weights [106]. The weights, or coefficients, of each feature are determined using the maximum likelihood estimation, that contributes to find the optimal values for these coefficients.

In other words, this function maps a set of input features to a probability value, ensuring that the outcome lies within the range of 0 to 1 [106]. To achieve this, LR defines a decision boundary, traditionally set at 0.5, which helps determine the classification outcome [98]. For instance, a probability exceeding 0.5 will be classified as a positive case, while values below 0.5 will be classified as a non-positive case. LR can also perform multiclass classification by employing techniques such as one-vs-all or softmax regression [107]. Additionally, it includes regularization methods, such as L1 and L2 regularization, that can be applied to enhance the model's generalization to new data and mitigate overfitting [107]. Reducing overfitting is an ideal practice in ML applications, since this issue can make ML algorithms excessively tuned to training data, preventing them from making accurate predictions or classifications based on new inputs [108].

Decision trees

Decision Trees (DT) are a widely used class of ML algorithms, known for their effectiveness in data classification and predictive modeling [91], [103]. They work by simplifying or breaking down complex problems into progressively manageable sub-problems or tasks [91], [103]. This logic unfolds in the form of a tree structure, characterized by multiple levels of nodes [91], [95], [98], [103]. The evaluation process starts at the top-level node, referred to as the root or parent node. Internal nodes, which contain at least one child node, represent the assessment of input variables or features, that is often performed by DT using criteria such as entropy and the Gini index [91], [103]. Depending on the outcome of this evaluation, the classification process branches to the appropriate child node, and this process is repeated until a stopping criterion, such as a

maximum tree depth, or a leaf node, the endpoint of decision-making, is reached [95], [98], [103]. These leaf or terminal nodes provide the final classification results [95], [98], [103].

One of the key advantages of decision trees is their interpretability and ease of learning, making them particularly valuable in fields like medical diagnosis [95], [98]. Their straightforward structure and transparent decision-making process contribute to their widespread use in various protocols for diagnostic applications [103]. Nonetheless, DTs can be prone to overfitting, particularly in DTs with large depths or multiple levels [109]. Still, there are techniques like pruning and setting appropriate hyperparameters that can help mitigate the overfitting issue in DT models [109].

Support vector machines

Support vector machines (SVMs) are versatile ML tools well suited for classification tasks [103]. SVMs work by identifying a hyperplane that can help segregate data points of distinct classes within a high-dimensional feature space [95], [96], [103]. In binary classification scenarios, SVMs try to identify an optimal hyperplane that can better separate data points into two categories. This hyperplane is meticulously selected to maximize the margin [95], [99], [103], term that refers to the spatial distance between the hyperplane and the nearest data points from each class [103].

SVMs employ kernel functions, such as linear, polynomial, and radial basis function (RBF) kernels, to evaluate the data in a higher-dimensional space where classification of samples can be more feasible than in its original feature space [96], [110]. A key concept in SVM is that of *support vectors*, which are the data points that reside closest to the hyperplane. They hold great importance for this algorithm since they influence the margin and the overall performance of the SVM model [110].

One main advantage of SVMs is their robustness in dealing with noisy data and outliers, as they prioritize the maximization of the margin [110]. For SVMs, the regularization parameter, C, plays a crucial role in adjusting the trade-off between achieving a wide margin and minimizing classification errors [96], [110]. SVMs can handle multiclass classification tasks through methods like one-vs-all or one-vs-one [110]. SVMs are implemented for applications in different areas, including image and text classification,

face recognition, bioinformatics, and more [96]. Their ability to effectively handle complex classification tasks and outliers underscores its status as a versatile and powerful ML tool.

K-nearest neighbors

In the supervised ML context, the k-nearest neighbors (KNN) method is known for its simplicity and applicability to both classification and regression tasks [95]. This algorithm relies on the concept of similarity [95], [103], [111]: when presented with a new data point, it identifies the k-nearest data points from the training dataset based on a chosen distance metric, such as Euclidean distance. These neighboring data points then play a pivotal role in determining the class label or value of the new data point. The selection of k significantly impacts the algorithm's behavior [95], [98], [111], with smaller k potentially leading to overfitting, while larger k values could result in smoother decision boundaries at the cost of overlooking local patterns.

One of the distinctive features of KNN is its flexibility in choosing distance metrics, allowing adaptability to different data types and problem domains [103], [111]. Common distance metrics include Euclidean, Manhattan, or Minkowski distances, depending on the specific characteristics of the data [111]. KNN is also often referred to as a "lazy learner" because it does not construct an explicit model during training; instead, it memorizes the training data and dynamically generates predictions during inference [99]. In practice, KNN finds applications in various domains, including recommendation systems, image recognition, and anomaly detection, where the notion of similarity plays a pivotal role [111]. It remains an attractive choice due to its ease of implementation and analytical tractability.

1.7. Thesis objectives and scope

The primary objective of this thesis is to enhance the reliability and clinical relevance of computational models for simulating SCI in NHPs. It has already been established that NHP models of SCI are one of the closest representations to human injury and could be an ideal intermediate platform for treatment testing before human trials. However, due to the difficult ethical, cost, and logistical challenges, their use in SCI research was limited, which reduces the information available to directly compare the findings or improve the experimental protocols. Computational or FE models can help circumvent some of these limitations only if they are a biofidelic representation of the mechanical interactions that occur during the experiments. Granted this, they can also

contribute to better understanding and even quantifying the correlation between the magnitude of those mechanical interactions and the spinal cord tissue damage that results in functional impairments.

In summary, this thesis endeavors to evaluate and enhance the reliability of computational models of SCI, with a focus on the CSF representation using SPH in a contusion model with preload, and the integration of supervised ML techniques for tissue damage identification. By addressing these critical aspects, the author aspires to contribute to advancing the clinical relevance of computational models, thereby accelerating the study and comprehension of spinal cord injury for potential clinical applications. The work presented in this document intends to bring computational models one step closer to this state through the methodologies of the following chapters.

Chapter 2: Methods for containing the cerebrospinal fluid in a computer simulation of large animal cervical spinal cord injury using smoothed particle hydrodynamics.

In this chapter, it is intended to refine the CSF boundary conditions in a computational model of NHP cervical SCI with preload. Previous studies have highlighted the pivotal role of CSF in spinal cord protection, and SPH method has demonstrated potential for accurately modeling its biomechanical effects in models of SCI. However, an important consideration arises from the different combinations of boundary conditions that have been used in previous studies to capture CSF's behavior during injury. The effect of these CSF boundary conditions on the mechanical outcomes of an FE model of SCI with preload has not been explored. Therefore, this chapter investigated the effect of four different boundary conditions for the SPH representation of the CSF in an NHP model of SCI. The influence of each boundary condition on the impact biomechanics, CSF pressure, stress and strain distribution, and computational cost in different spinal cord morphology scenarios was compared using FE models. The results can help guide the choice of CSF boundary conditions to improve the efficiency and biofidelity of computational models of SCI.

Chapter 3: Identification of injured elements in computational models of spinal cord injury using machine learning.

Chapter 3 aims to improve the predictive capabilities of computational models of SCI by integrating supervised ML algorithms. Our approach combined experimental data

of tissue damage from SCI experiments and computational mechanical outcomes, to train four supervised ML algorithms to identify injured elements based on the mechanical predictions of FE models of SCI. The injury classification performance of the ML algorithms was compared on three different datasets of elements representing the individual and combined sets of spinal cord tissues (i.e., GM, WM, and GM+WM) using different metric scores, such as the area under the ROC curve. This chapter extended the analysis to investigate the mechanical feature importance assigned by the best ML classifiers, and the range of mechanical values reported for classified samples with an injury probability above 50% on each dataset. This study provided useful data regarding the suitability of ML algorithms for injury identification based on FE mechanical predictions, and the different tissue damage susceptibility of the spinal cord tissues to stress and strain magnitudes. These findings could deepen our understanding of the impact-to-injury link in SCI, ultimately contributing to improved diagnostic and therapeutic strategies.

Chapter 2.

Methods for containing the cerebrospinal fluid in a computer simulation of large animal cervical spinal cord injury using smoothed particle hydrodynamics

Experimental animal models of SCI have proven the importance of including the CSF in physical and computational injury models. However, representing the CSF's biomechanical interactions during SCI simulations increases their computational cost and complexity. Computational techniques, such as SPH, have been successful in simulating the CSF in brain and spinal cord injury studies. However, different boundary conditions have been used to capture CSF's behavior during injury without properly assessing their effect in the mechanical outcomes of the models. Therefore, in this study we examined the implementation of four different methods to bound the CSF representation with SPH and their effect on the mechanical results of a computational model of SCI. An FE model of a NHP unilateral cervical contusion SCI experiment involving two phases: preload and impact phases was developed. Across three different spinal cord and column morphologies, the impactor's displacement, reaction forces, CSF pressures, stress/strain distribution, and computational times were compared between the evaluated CSF containment methods. It was observed that the implemented CSF constrains had a large effect in the calculated impactor displacement, and preload reaction forces. During impact, the models predicted reaction forces in the range of 18.25 - 28.61 N, with lower magnitudes and different force profiles in the small morphology resulting from the lateral shift of the spinal cord. The boundary conditions that allowed for more CSF displacement during the simulations resulted in CSF pressure values (0.07 – 0.14 MPa) within or close to those reported in other SCI experiments in large animals and showed minor influence from the morphology of the model. Lastly, the choice of CSF boundary conditions proved to affect the magnitudes of stresses and strains at the injury epicenter of the spinal cord. The distribution of these mechanical values, particularly of stress, shifted dorso-laterally as the spinal cord and dura mater sizes increased. The results of this study offer valuable insights regarding the effects of CSF boundary conditions in the biomechanical outcomes of FE models of SCI with preload and different cord morphologies. These results can serve as general guidelines for defining the CSF boundary conditions that better suit different SCI scenarios, enhancing the utility of computational models for studying SCI.

2.1. Introduction

Scientists and engineers continue working on new ways to understand spinal cord injury (SCI) and translate the findings from animal SCI models into effective treatments [3], [4], [5]. Finite element (FE) models of SCI have emerged as a complimentary tool to refine *in vivo* animal experiments without needing to include additional subjects; reducing some of the cost, ethical, and logistical challenges of SCI research [5], [17], [54]. This is particularly relevant in large animal models, which display greater intersubject variability and greater proportions of cerebral spinal fluid (CSF) than small animal models [47], [66]. Recent work in large animal SCI has emphasized the significant influence of the CSF in contributing to variability in injury outcomes [13], [56], [65], [66]. FE models can provide detailed mechanical data to study the correlation between mechanical loading and tissue damage after SCI [8], [9], [18]. However for FE models of SCI to be relevant, they need to accurately capture the experimental injury [5]. There has been substantial work developing and validating FE models of SCI including focus on material properties [9], [18], [112], morphology [18], [19], [57], and impact mechanisms [8], [17], [19] for both animal and human models. However, while there has been increasing focus on the contributions of CSF in large animal SCI experiments, there has been limited consideration or validation of FE modeling approaches for CSF in large animal SCI models.

The material representation of the CSF in FE models of SCI and traumatic brain injury (TBI) has evolved over several decades of research. In most recent FE models such as the ones proposed in [18], [57] and [19], the CSF is represented using SPH. This particle-based method has been successfully used in FE models of SCI to represent the CSF [8], [18], [19], [23]. Moreover, in a recent comparison by Rycman et al. [16] in an FE model of SCI based on *ex vivo* bovine experiments, SPH reported a better accuracy-to-efficiency ratio than previous methods to represent the CSF, such as traditional Lagrangian mesh, arbitrary Lagrangian-Eulerian mesh, and pressure cavity. However, the implementation of SPH for representing the CSF has not been validated against experimental data or explored in different SCI scenarios. For instance, the models in [18], [57] and [19], recreate injury experiments in NHPs that include a preliminary phase, called the preload [47]. Experimentally, this phase was meant to displace the CSF from the impact site and trap the spinal cord at the ventral section of the spinal column prior to the impact, helping deliver more consistent injuries in the NHP subjects. As such, the SPH

method needs to capture the preload CSF displacement, without neglecting its biomechanical effect during the impact phase.

Researchers have used different CSF boundary conditions to simulate the SCI experiments [8], [18], [19], [23], [57]. However, the biofidelity of these CSF boundary conditions or their effect on the mechanical outcomes of the models have not been explored. This is an important consideration since some of these boundary conditions significantly restrict the displacement of the SPH particles inside the FE model [18], [23], [57], while others allow the particles to free flow during the entire simulation [8], or only allow during a specific phase of the analysis [19]. These differences could influence the spinal cord's trapping during the preload phase, or they could under or overestimate the pressure exerted by the CSF on the spinal cord during impact. Jones et al. [13] SCI work in large animals has shown that the changes in CSF pressure during impact contributes to extend the damage in spinal cord sections close to the injury epicenter, meaning that properly capturing this pressure can provide more realistic outcomes in the FE models. However, overestimating the CSF pressure could result in larger peak stress and strain values in the spinal cord, as it was found by Arhiptsov et al. [23] in their work with an FE model of human SCI where the CSF pressure was increased to represent the effect of a pre-existing medical condition in patients. It is then important to properly capture the CSF pressure in FE models of SCI, so they can be a more reliable tool for understanding and refining in *vivo* experiments and provide accurate tissue-level mechanical data.

The primary objective of this study was to compare the effect of different CSF boundary conditions on impact biomechanics, tissue stresses and strains, and CSF pressure in a simplified unilateral cervical contusion injury model based on NHP experiments. NHPs are one of the closest representations to human injury available [17], [47], which makes FE models relevant, as their contributions can have a stronger impact in humans. However, there is large variability in the spinal cord and dural space morphologies of NHPs that has been found to affect the outcomes of experimental [47], [48] and computational [19], [57] studies of SCI. Moreover, these morphological variations define the CSF volume and the thickness of the CSF layer that surrounds the spinal cord, which has shown to affect the mechanical outcomes of injury experiments in other SCI studies in large animals [66]. Since different morphological cases can affect the CSF presence in the FE models, a secondary objective of this study was to compare the suitability of the CSF boundary conditions to capture the general and tissue-level SCI

mechanics of the experiments under different spinal cord and column morphologies. The results of this work will inform researchers on the appropriateness of different CSF boundary conditions to capture the behaviour of the CSF more accurately in computational models of SCI based on animal experiments. However, understanding how these different boundary conditions change the CSF behavior during the simulations can also have applications in the modelling of human SCI cases. As it has been done previously, FE models can simulate human SCI cases influenced by preexisting medical conditions [23] that change the CSF pressure. The boundary conditions evaluated in this study could provide an additional approach to study the effect of CSF changes related to neurological disorders or degenerative spinal changes, extending the clinical usability of FE models of SCI.

2.2. Methods

Different methods to contain the CSF inside a simplified FE model of unilateral cervical contusion SCI in NHPs were compared. Although previous work has shown that subject-specific FE models of SCI provide more biofidelic and detailed data [18], simplified models provide a more computationally efficient platform to compare these different CSF boundary conditions. Mechanical outcomes including the impactor's displacement, reaction forces, CSF pressure, and stress/strain distribution were compared against available experimental data [47]. This assessment helped to define the generalizability of each set of boundary conditions to capture the CSF's biomechanical effect during SCI experiments with preload. The CSF boundary conditions were also compared in FE models with different spinal cord and dural space (also referred to as subarachnoid space) dimensions, taken from experimental NHP subjects. This comparison assessed the suitability of the CSF boundary conditions to simulate FE models of SCI with different morphologies, which is a common source of variability in NHP subjects.

2.2.1. Unilateral cervical contusion FE model

A simplified NHP unilateral cervical contusion SCI model (Figure 2-1) was implemented in ABAQUS (Dassault Systèmes 2021) following the approach, materials, and dimensions detailed in Jannesar et al. [57]. Briefly, the model included the dura and pia maters, spinal cord's gray and white matters, and the CSF (Figure 2-1 A). The parts

representing these tissues were contained inside a spinal column segment representing three-vertebrae (Figure 2-1 B) [57]. The spinal column segment included a partial laminectomy of 8.5 x 8.5 mm in the dorsal surface, and the rostral and caudal ends were closed with a rigid surface (Figure 2-1 B). A 4 mm diameter rigid impactor impacted the cord on one side to simulate a unilateral impact (Figure 2-1 C). A 4 mm diameter rigid impactor impacted the cord on one side to simulate a unilateral impact (Figure 2-1 C). In the experiments [47], there was variance in defined mediolateral alignment of the impactor with respect to the spinal cord's midline, reporting values of 0-, 0.5-, and 1-mm. To account for this variance, preliminary FE modelling recreating the NHP experiments [17], [18] tunned the impactor's alignment to capture the experimental biomechanical outcomes more closely. The same approach was followed in our FE model, resulting in 0 mm alignment of the impactor with respect to spinal cord's midline in our simulations. Contact interactions were defined using the general contact algorithm instead of with the surface-to-surface approach used in [18] and [57] to minimize penetration between components. The friction coefficients reported in [18] were used for defining the interaction properties. The impact simulations were submitted and run using supercomputer cluster nodes with a CPU Intel E5-2683 v4 running at 2.1 GHz (Digital Research Alliance of Canada).

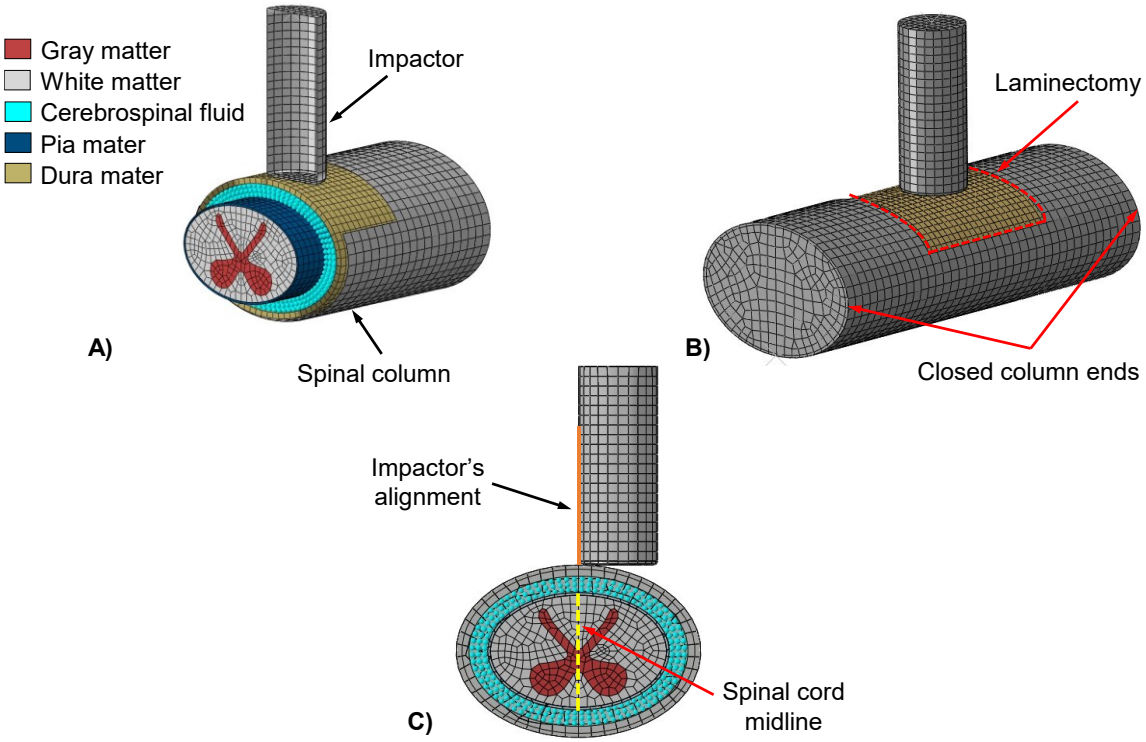

Figure 2-1. Cut view of generated FE model of cervical SCI and its constituent tissues (A), and spinal column closed ends (B). The closed ends work as a physical barrier to keep the SPH particles represeting the CSF between the dura and pia maters. Cross-section view of the impactor's mediolateral alignment with respect to the spinal cord (C).

Model's mesh details

The mesh pitch sizes for the white and gray matter solids were defined after a mesh convergence analysis. The quality of the mesh was also validated to facilitate the computation and accuracy of results [113]. The CSF solid was partitioned prior to meshing, to improve the homogeneity of the mesh elements, and the mesh pitch was also defined after a convergence analysis. The values for the specific meshes of each component in the model are included in Table 2-1.

Table 2-1. Mesh parameters and characteristics for the FE model.

Part	Part type	Element type	Mesh pitch	Number of elements
White matter	Deformable solid	Hexahedral (C3D8R)	0.45 mm	12320
Gray matter	Deformable solid	Hexahedral (C3D8R)	0.45 mm	4536
Pia mater	Skin	Quadrilateral shell (S4R)	0.45 mm	2912
Dura mater	Deformable shell	Quadrilateral shell (S4R)	0.45 mm	3762
CSF	Solid converted to particles	Particle element (PC3D)	0.35 mm	16188
Spinal column	Discrete rigid shell	Quadrilateral (R3D4)	0.65 mm	1990
Impactor	Discrete rigid shell	Quadrilateral (R3D4)	0.5 mm	648

To apply the SPH method to the CSF, the CSF was modeled first as a deformable solid filling the space located between the dura mater, pia mater, and the rigid column ends (Figure 2-2). In contrast to Jannesar et al. [18] and [57], the SPH method was defined using the CAE, which allowed the conversion of solid elements representing the CSF into SPH particles (Figure 2-2 C&D). The default values for the requested fields were defined for the SPH conversion: criterion - Time, threshold – 0 (i.e., the particle conversion will trigger at the beginning of the simulation), number of parts per local direction - 1, and kernel - cubic.

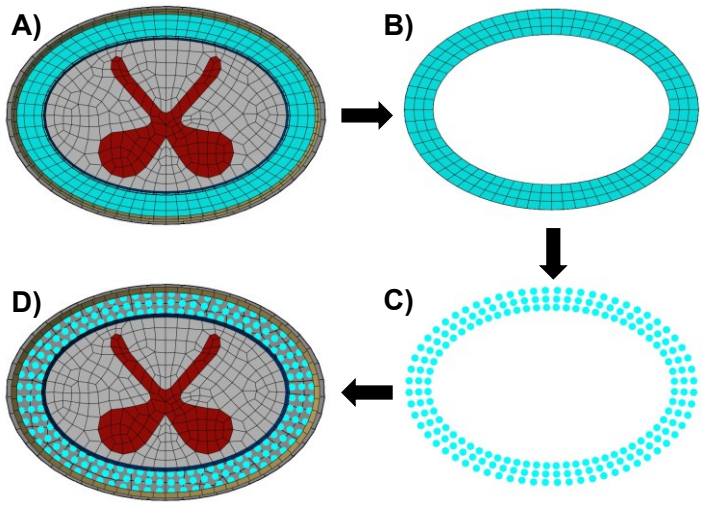

Figure 2-2. Diagram of the process to model the CSF using the SPH approach. A) Solid geometries defined for each instance of the model. B) Isolated solid elements representing the CSF. C) Conversion to particles of the solid CSF mesh. D) Final model with solid sections and CSF represented with SPH.

Model's material properties

The material properties included in all the FE models followed the reported values and constitutive material models by Jannesar et al. [18]. The constitutive models used for representing the material properties will be briefly discussed and the values of its constant will be included in Table 2-2. The pia mater was defined in ABAQUS as a linear isotropic elastic material. The required parameters for defining this material were the Young's modulus, E, the Poisson's ratio, υ [114]. The gray matter and dura mater material properties were defined as hyperelastic with quasi-linear viscoelastic (QLV) behavior. The hyperelastic properties of these two tissues were defined in ABAQUS with an Ogden model, whose equation is described next [115]:

$$U = \sum_{i=1}^{N} \frac{2\mu_i}{\alpha_i^2}\left(\bar{\lambda}_1^{\alpha_i} + \bar{\lambda}_2^{\alpha_i} + \bar{\lambda}_3^{\alpha_i} - 3\right) + \sum_{i=1}^{N} \frac{1}{D_i}\left(J^{el} - 1\right)^{2i} \quad (3)$$

In Eq. 3, U represents the strain energy per unit volume, $\mu_i, \alpha_i,$ and D_i are material parameters dependent on temperature, and N is a material parameter. $\bar{\lambda}_i$ are the deviatoric principal stretches, and J^{el} is the elastic volume ratio. For the QLV behavior, a three and four-term Prony series were used for the gray matter and dura mater, respectively. The Prony series were included as a time-domain table with g_i being the shear relaxation modulus ratio, and τ_i being the relaxation time [116].

For the CSF, its material properties were defined in ABAQUS using an equation of state. The implemented formulation was the linear Hugoniot form of the Mie-Grüneisen equation of state, that describes the relationship between pressure and density in solids and fluids [117], [118].

$$p = \frac{\rho_0 c_0^2 \eta}{(1-s\eta)^2}\left(1 - \frac{\Gamma_0 \eta}{2}\right) + \Gamma_0 \rho_0 E_m \qquad (4)$$

For this equation, p is pressure, ρ_0 is the reference density, c_0 is the bulk speed of sound, η is the nominal volumetric compressive strain, s is the linear Hugoniot slope coefficient, Γ_0 is the Grüneisen parameter at the reference state, and E_m is the internal energy per unit mass.

Finally, the white matter properties were set as a user-defined material with QLV behavior and conditional hyperelasticity [10]. The conditional model was used to capture the transverse isotropy of this tissue resulting from the set of aligned axonal fibers across the spinal cord's white matter. When there are not stretches in the fibers' direction, white matter's hyperelastic behavior can be described using a Mooney-Rivlin model [115] (U_{WM}), and if there are stretches in the fiber's directions, the U_{WM} equation is combined with the reinforcing function U_{Fibers} :

$$U_{WM} = C_{10}(\bar{I}_1 - 3) + C_{01}(\bar{I}_2 - 3) + \frac{1}{D_1}\left(J^{el} - 1\right)^2; \qquad (5)$$

$$U_{Fibers} = \frac{\gamma}{2}(\bar{I}_5 - 1)^2 \qquad (6)$$

In these equations, U represents the strain energy per unit volume, c_{10}, c_{01}, γ, and D_1 are specific parameters of the material, J^{el} is the elastic volume ratio, and $\bar{I}_1$, $\bar{I}_2$ and $\bar{I}_5$ are deviatoric strain invariants. The conditional material model was implemented in ABAQUS using the user subroutine previously developed in [10], [18], and the QLV behavior was defined using a four-term Prony series. These material properties were assigned to all the elements corresponding to the WM part in our FE models, and the material orientation for considering the reinforcing function was defined along the rostral-caudal direction for the WM elements.

Table 2-2. Material specifications used in the FE models taken from [18].

Tissue	Required constants	Viscoelastic constants	Density
White matter	C_{10} =3.27E-3 [MPa] C_{01} =0.91E-3 [MPa] D =0.2393 [MPa] γ =6.172E-03 [MPa] υ =0.4995	g_1 =0.5256 g_2 =0.3163 g_3 =0.1250 g_4 =0.0071 τ_1 =0.01 s τ_2 =0.02 s τ_3 =0.2 s τ_4 =2.0 s	ρ =1041[$\frac{\mathrm{kg}}{\mathrm{m}^3}$]
Gray matter	μ_0 =4.454E-2 [MPa] α =10.57 D =0.045 [MPa] υ =0.49	g_1 =0.4793 g_2 =0.2854 g_3 =0.0732 τ_1 =0.64 s τ_2 =6.40 s τ_3 =64.0 s	ρ =1045[$\frac{\mathrm{kg}}{\mathrm{m}^3}$]
Dura mater	μ_0 =1.2 [MPa] α =16.2 υ =0.45	g_1 =0.329 g_2 =0.128 g_3 =0.086 g_4 =0.086 τ_1 =0.009 s τ_2 =0.081 s τ_3 =0.564 s τ_4 = 4.69 s	ρ =1174[$\frac{\mathrm{kg}}{\mathrm{m}^3}$]
Pia mater	E =39.3 MPa υ =0.3	-	ρ =1075[$\frac{\mathrm{kg}}{\mathrm{m}^3}$]
CSF	c_0 =1381.7 $\frac{\boldsymbol{m}}{\boldsymbol{s}}$ s =1.979 Γ_0 =0.11	-	ρ =1007[$\frac{\mathrm{kg}}{\mathrm{m}^3}$]

Loading and boundary conditions

Following the NHP cervical unilateral contusion injury experimental protocol [47], each simulation was divided into two steps: preload and impact (Figure 2-3). During the experiments, the impactor descends towards the dura mater at a rate of ~0.33 mm/s to trap the spinal cord against the ventral portion of the spinal canal. In our simulations, replicating the experimental preload displacement rate was not computationally feasible, since it exceeded the allowed run time in the computer cluster the simulations were

submitted to. As such, the preload rate was adjusted to a rate 40 mm/s, which allowed us to run the simulations within the allowable time. The preload step was defined to stop once the reaction force reached the threshold value of 0.36 N, following the experimental mean of the data available [47]. After reaching the threshold, the impactor position was held constant for 0.2 s to allow the viscoelastic materials to relax, similar to the experimental protocol. The impact step was then triggered. The impactor's impact displacement was defined using tabular data from one NHP experiment. This experiment was selected to match the displacement magnitude closest to the overall mean displacement value observed in the injury experiments. The experimental displacement curve showed a closer behavior to the predefined displacement curve. The impact displacement was then defined as 3.6 mm with a speed of 0.4 m/s.

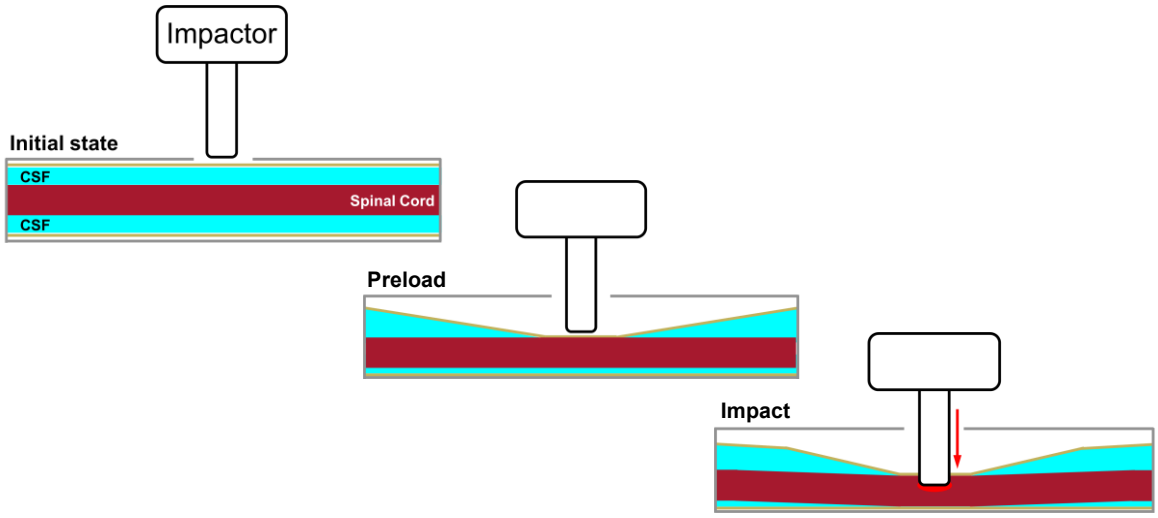

Figure 2-3. Representation of the SCI experiment phases in NHPs recreated in the computational model (adapted from [47] - Fig. 1D). During the preload, the spinal cord and dura mater ends are allowed to displace in the impactor's direction, and they are pinned during the impact to minimize lateral shift of the spinal cord.

The boundary conditions for the spinal cord and dura matter were defined in two stages [18], [57]. During the preload phase, the rostral and caudal ends of the dura mater and the spinal cord had a symmetric condition along the rostral-caudal direction allowing movement of the spinal cord and dura in the dorso-ventral and mediolateral directions. At the impact phase, the condition was changed to restrict only the dorso-ventral displacement of both the dura and spinal cord sections. During both phases, the spinal column was fixed at its reference point using the encastre condition. Finally, for the impactor, a dorso-ventral displacement was defined for each step. During the preload

phase, it was defined as a conditional displacement interrupted once the impactor's reaction force reached the force threshold, and for the impact it was defined using tabular data from the actuator during the SCI experiments.

2.2.2. Boundary conditions for the CSF

We assessed four boundary condition approaches (Figure 2-4) in FE models of SCI in NHP with preload while representing the CSF using the SPH method. For this study, the boundary conditions were assigned the following names: 1) closed-boundary, 2) open-boundary, 3) alternating-boundary, and 4) volume reduction. Each one is explained more in detail in the following sections.

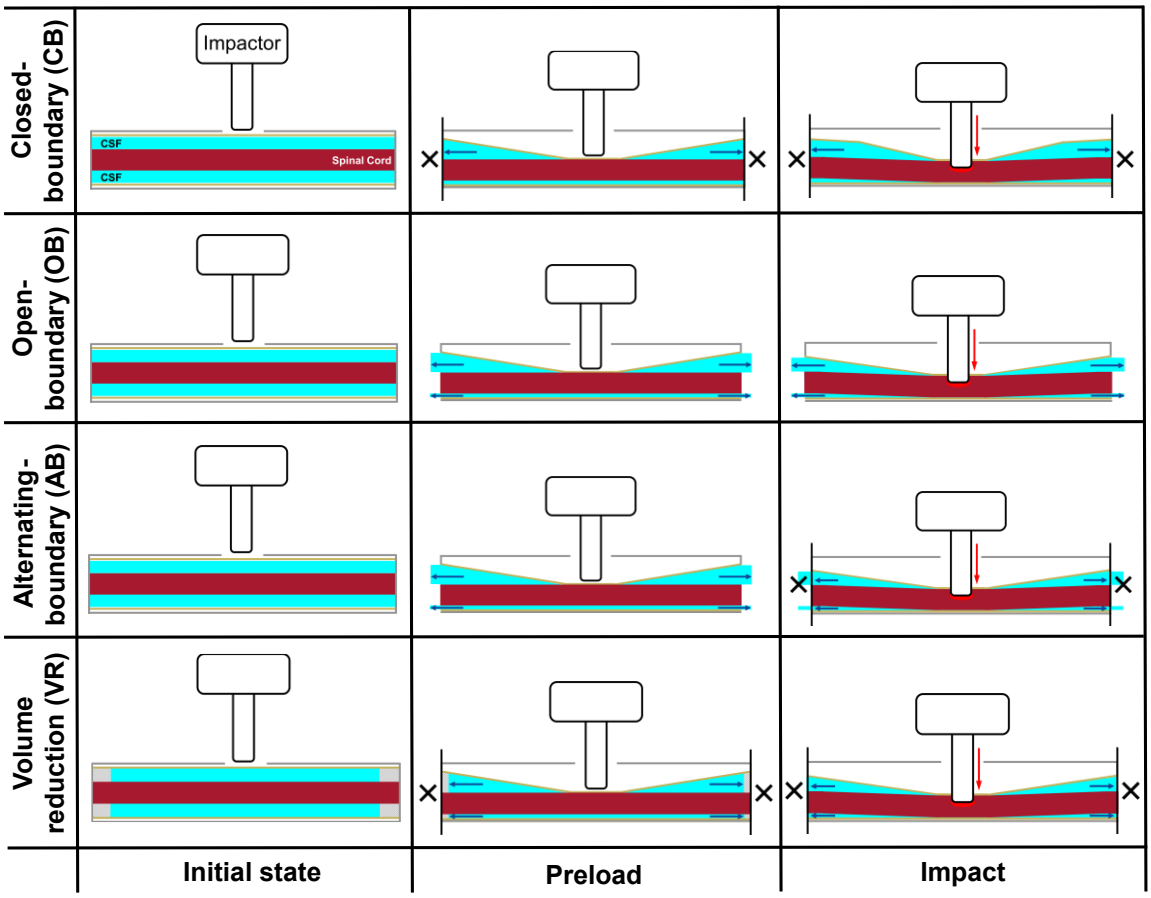

Figure 2-4. Diagrams of the evaluated approaches to constrain the SPH particles representing the CSF in computational models of cervical SCI throughout the different phases of the injury experiment. The blue arrows indicate the expected direction of CSF displacement, and the black lines with an 'X' sign at the end, represent the column edns preventing the CSF particles from leaving the dural space.

Closed-boundary (CB) approach

One of the most common modeling approaches is to constrain CSF inside the subarachnoid space. It was used in previous FE models of SCI based on NHPs [18], [57] and humans [23]. In this model, the interactions between the column ends and the CSF particles represented with SPH were defined using general contact, so that no fluid particles could exit the system.

Open-boundary (OB) approach

As the name suggests, this approach consists of having an open SCI model at the rostral and caudal ends, that allows for the CSF particles to leave the subarachnoid space during the impact. This approach has been reported in studies of rat cervical SCI by Russell et al. [8] and computational models recreating in-vitro experiments on bovine spinal cords [15].

Alternating-boundary (AB) approach

Following the procedure described in [19], the interactions between the column ends and the CSF particles were excluded from the general contact definition in the preload step, so that the particles could pass through the column rostral and caudal ends, similar to an open-boundary. During the impact step, the contact definition was changed so the column ends would interact again with the particles representing the CSF, similar to the closed-boundary. As a result, the particles displaced during the preload step remained outside of the dural cavity, effectively reducing the volume that would pressurize the spinal cord during the impact phase (Figure 2-4).

Volume reduction (VR) approach

This approach reduced the volume of CSF within a closed-boundary model by removing an equivalent volume of solid elements from the mesh before conversion to fluid particles (Figure 2-5 A & B). The initial CSF volume was reduced by approximately 86 mm^3, which corresponded to the equivalent volume the cylindrical impactor would occupy inside the model at the impact time. This equivalent volume was calculated using the impactor's displacement information from the NHP experiments of SCI, and its reported dimensions. The VR approach was proposed as an alternative to the OB and AB boundary conditions, where the CSF particles that leave the dural space still must be considered

during the entire simulation. By reducing the initial CSF volume, it was expected to provide additional space to capture the CSF preload displacement without discarding its mechanical effect during impact. Moreover, the lower number of particles in the model was expected to increase the computational efficiency of the simulations.

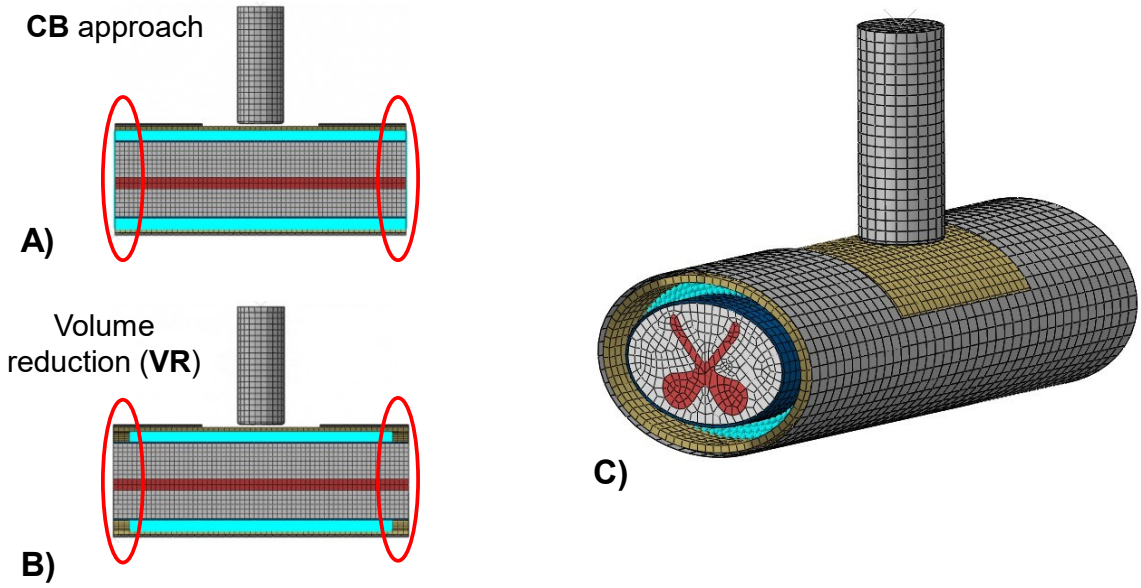

Figure 2-5. Visual examples of the VR apporach implemented in the FE model of SCI. A) Cut side-view of the FE model with the CB approach, as reference, and B) of the FE model with the VR approach. Elipsoidal figures highlight the differences in the amoun of SPH particles representing the CSF in the CB and VR methods. C) Isometric view of the FE model using the VR method as the CSF boundary conditions. The closed column end was hidden for better visualization of the empty space at the rostral end of the model.

2.2.3. Case study models

To determine the interaction of the different CSF modeling approaches and different cord and column morphologies on resulting injury mechanics, two additional models with different spinal cord and subarachnoid space dimensions were included. The dimensions for the models defined based on Jannesar et al. [57] combinations of minimum and maximum dorso-ventral and mediolateral dimensions measured from the spinal cord and dural space of NHP subjects (Figure 2-6).

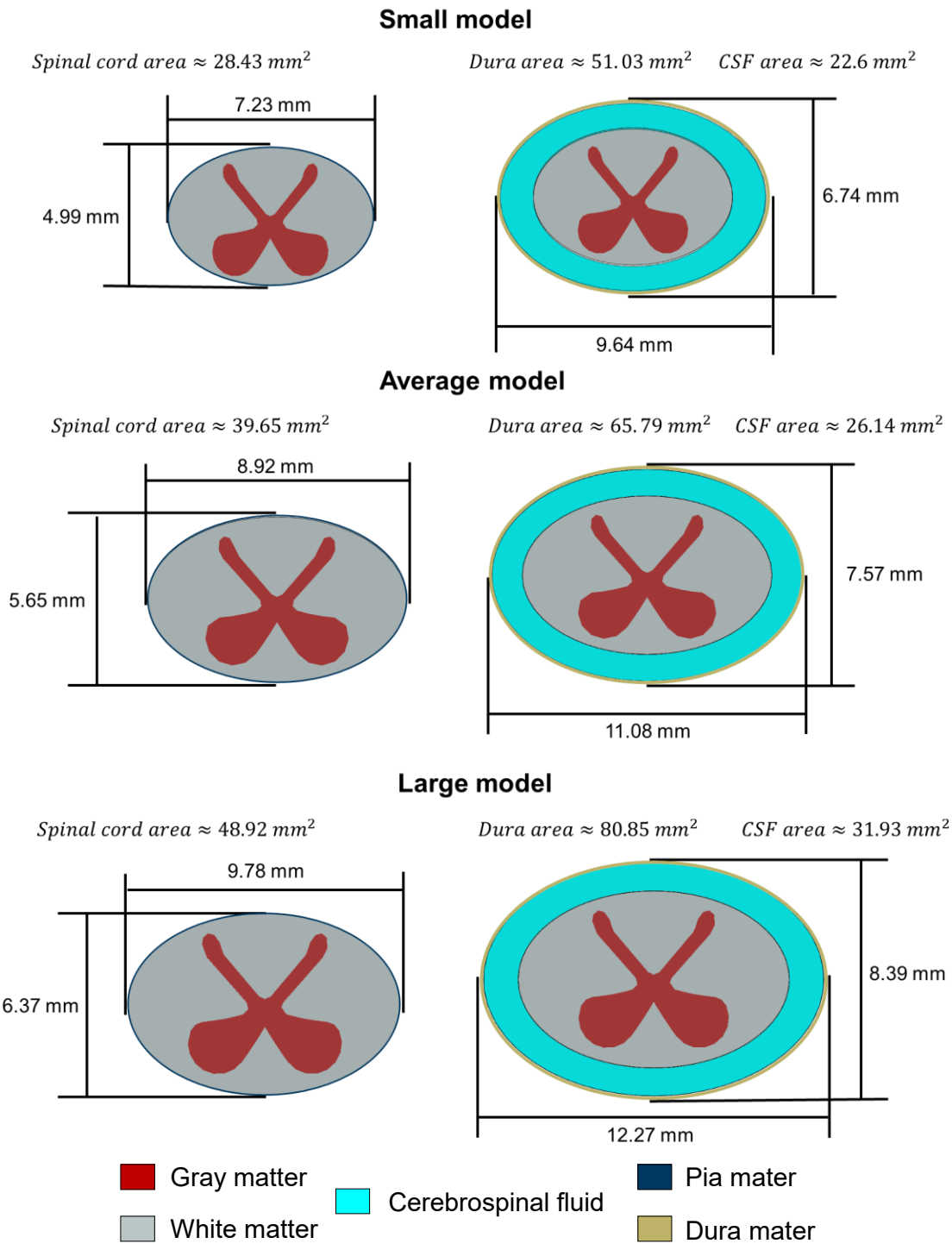

Figure 2-6. Small, average, and large FE models dimensions for the spinal cord, dural space, and CSF layer area. All the cross-sections are on the same scale.

For the smaller and larger spinal cord and dural space morphologies, the mesh pitch used for the average model resulted in reduced mesh quality, particularly at the

interface between the gray and white matter sections. To maintain an optimal aspect ratio and geometric deviation factor in the spinal cord meshes of the small and large models, their mesh pitches were refined, resulting in an increased number of elements representing these tissues. The mesh parameters and number of elements are reported in the Appendix A.

2.2.4. Reported output parameters

The evaluated outputs from the models included the impactor's displacement and reaction forces during both preload and impact. Each simulation was also checked for particle penetration, and their computational times were reported. The individual pressure values experienced by the SPH particles in the simulation were averaged through the entire CSF volume at every time increment to make the pressure readings comparable to experimental data. The results were used to evaluate the behavior of the entire particle cluster in the different simulated scenarios during the impact phase. In [19], lateral shift of the spinal cord at the time of impact was shown to affect the force outcomes in FE models of SCI. Following [19] procedure, the spinal cord's lateral shift was calculated by determining the change in the vertical position of the center of the spinal cord relative to the impactor (Figure 2-7). This measurement was taken vertically, since the lateral shift induces rotation of the spinal cord, translating its midpoint to a higher vertical position relative to the starting point at the end of the preload [19]. Lastly, the distribution of Tresca stress, and strains (maximum & minimum logarithmic strain) in the spinal cord cross-section located at the epicenter of the impact was assessed to determine the effect of CSF modeling approaches on tissue level mechanics. These mechanical parameters have been used in previous studies to correlate mechanics to tissue damage [8], [9], [18], making it relevant for FE models to appropriate approximations of these values.

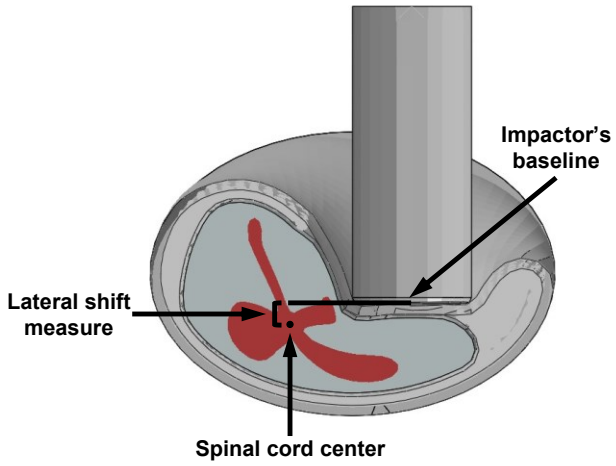

Figure 2-7. Diagram of the lateral shift measurement taken following [19] methods.

2.3. Results

2.3.1. Impactor's displacement and reaction forces

Overall, all computational simulations behaved in a similar way. The impact forces followed similar profiles, while the preloads showed small variability in preload displacement associated with the preload force condition and the displacement of SPH particles representing the CSF. In all simulations the spinal cord showed limited deformation during the preload stage where CSF movement predominated. In the impact phase, there was large deformation of the spinal cord as well as lateral displacement of the cord due to the unilateral impact. No overlapping or penetration between structures in the model or instances or leaking of SPH particles through the dura mater or the spinal column was observed in the simulations, confirming the suitability of the contact definitions.

During the preload and impact phases, the VR approach predicted the largest impactor displacements, followed by the OB and AB methods (Table 2-3). These two methods reported identical impactor displacements, which were shorter than the VR ones by 30%, 6%, and 6.1% in the small, average, and large models respectively. The CB method reported the shortest displacement values. These observations were consistent throughout all three morphologies. On preload reaction forces, there was no observable trend between the results on different morphologies, other than the estimated values with the CB approach were among the lowest ones in all cases. Regarding peak impact forces,

the VR method predicted the highest values in the three morphological cases, while the lowest values were calculated by different approaches depending on the morphology. On average, largest preload and impact displacements were observed in the large model, followed by the average, and then the small morphologies. Meanwhile, for the preload and impact reaction forces, the average model reported higher mean values than the large and small morphologies, in that order.

Table 2-3. Predicted values for the impactor's dispalcement and peak reaction forces during preload and impact phases for each evaluated CSF approach and morphology scenario.

Morphology	CSF containment approach	Impactor's displacement		Impactor's peak reaction force	
		Preload (mm)	Total (mm)	Preload (N)	Impact (N)
Small	CB	1.31	4.95	0.30	22.11
	OB	1.49	5.13	0.35	18.25
	AB	1.49	5.13	0.30	20.17
	VR	2.13	5.77	0.33	22.80
Average	CB	1.43	5.07	0.32	24.89
	OB	1.86	5.49	0.35	27.29
	AB	1.86	5.49	0.35	28.17
	VR	1.98	5.62	0.34	28.35
Large	CB	1.57	5.20	0.33	25.47
	OB	2.00	5.64	0.33	22.46
	AB	2.00	5.64	0.33	24.60
	VR	2.13	5.78	0.36	28.61

The impact force profiles of the CB, OB, AB, and VR approaches were similar in shape between morphologies and with respect to experimental data (Figure 2-8). In the small model, all the CSF containment methods predicted reaction forces with similar or lower peak values than the experimental sample; the largest percentage error between predicted and experimental force was observed with the OB method (21.7%). In the average and large morphologies, all three methods reported higher peak force values than the experiment, particularly with the VR approach. In those cases, the largest error percentage also corresponded to the VR predicted forces, with values of 21.7 and 22.8% for the average and large morphologies, respectively. The peak impact forces in the small model showed the lowest range of reaction forces among the evaluated morphologies, and different force profile shapes in comparison with the other models (Figure 2-8).

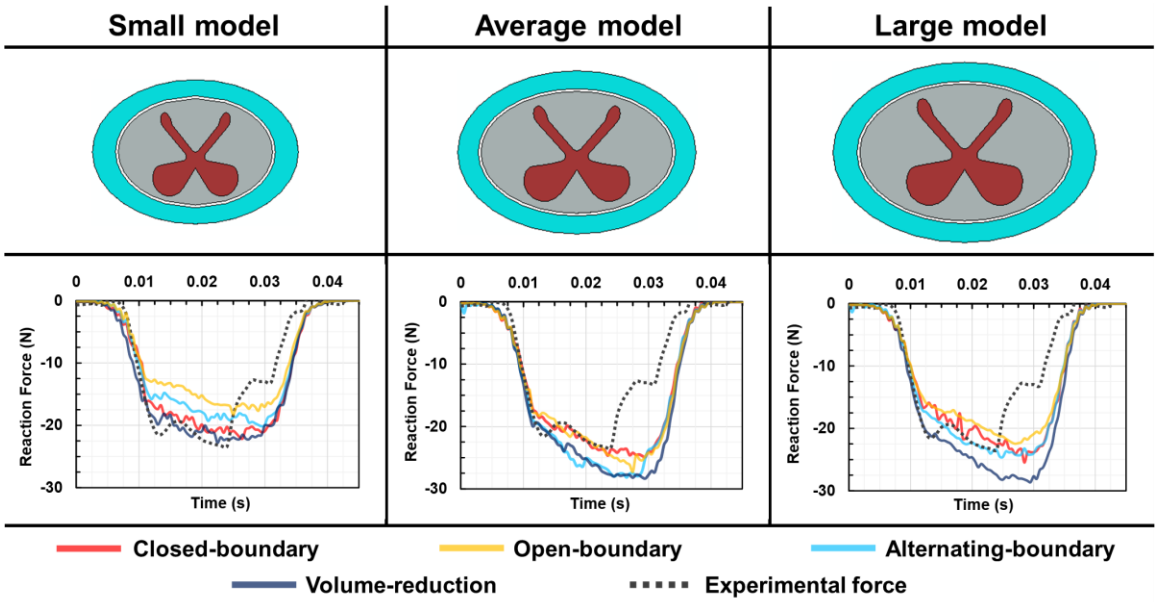

Figure 2-8. Impact reaction forces for each evaluated CSF containment approach and morphology scenarion. The three graphs include the reaction force profiles of the same NHP experiment that reported the highest peak force value (23.2 N) among five experiments following the same impact protocol as in the simulations.

At the time of maximum compression, more spinal cord lateral shift was observed in the small morphology, regardless of the CSF containment technique (Table 2-4). For each morphology, the largest lateral shifts were measured using the VR method, and the smallest with the CB approach. The largest percentage difference between the largest and smallest lateral shift values due to different boundary conditions was observed in the small model (~194%). The OB and AB techniques reported lateral shift values lower than the mean in each morphological case. Additionally, it was observed that for all the CSF boundary conditions, the spinal cord's lateral shift decreased as the model's dimensions increased. Cut-view images at the time of maximum compression for all the simulations are included in the Appendix B, where it is possible to observe the lateral shift of the spinal cord.

Table 2-4. Spinal cord's lateral shift calculated for each morphology case and compared between CSF containment techniques. Positive values indicate larger lateral shifts, while negative values indicate less lateral shift and more spinal cord tissue engaged under the impactor.

Magnitude	Morphology	CSF containment approach			
		CB	OB	AB	VR
Spinal cord midpoint's vertical position with respect to the impactor (mm)	Small	0.02	0.22	0.25	1.28
	Average	-0.91	-0.30	-0.29	-0.06
	Large	-1.50	-0.92	-1.00	-0.76

Variability in the preload reaction force profiles between the different CSF boundary conditions and morphologies was also found (Figure 2-9). The preload force curves of the CB method were consistent in their shape between morphologies. The OB and AB approaches showed an identical preloading behavior in the average and large models, however in the small morphology the similarities stopped after the transition to the relaxation part. The VR method showed more inconsistent curves across models, yet it was consistently the approach that took the longest to finish the preloading phase due to a lower system stiffness.

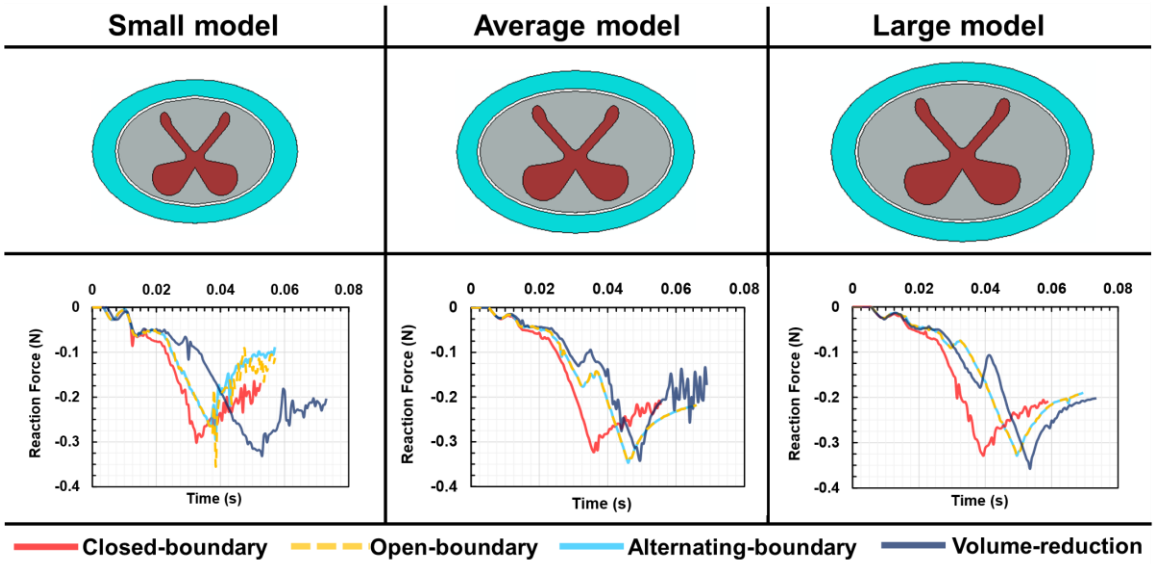

Figure 2-9. Preload reaction forces for each evaluated CSF containment approach and morphology scenarion. The OB line was dashed since it overlapped to the AB method's results. After reaching forces close to the predefined threshold (0.36 N) there were oscilations in the measurements during the relaxation time for most of the approaches and morphology models resulting from the re-arrangement of the SPH particles around the spinal cord.

Magnitude-wise, the largest percentage error between the peak preload force and the predefined threshold value was around 17%, and it was observed in the small model using the CB and AB approaches. After that, for the other CSF constrain techniques and morphology dimensions, the error ranged between 0 and 11%. To further study the effect of these preload force magnitude differences in the subsequent steps, the deformation of the spinal cord cross-section at the end of the preload was also compared between model scales and boundary conditions (Table 2-5).

Table 2-5. Percental change in dorso-ventral diameter of the spinal cord cross-section during impact for each evaluated CSF approach and morphology scenario.

Magnitude	Morphology	CSF containment approach			
		CB	OB	AB	VR
Dorso-ventral spinal cord diameter change after preload (%)	Small	-6.10	-5.58	-5.17	-9.49
	Average	-6.92	-7.74	-7.74	-7.95
	Large	-6.01	-6.72	-6.72	-7.34

By comparing the dorso-ventral diameter of the spinal cord cross-sections on each model before and after the preload, it was possible to identify the level of spinal cord compression before the impact. The percentages in Table 2-5 show that the largest spinal cord compression after the preload resulted from using the VR method, regardless of the morphological case. The differences between the largest and smallest dorso-ventral compression change were approximately 59%, 14%, and 20% for the small, average, and large models, respectively. In the small model, both the CB and AB reported similar preload force magnitudes, with larger levels of compression observed for the CB approach. In the average and large morphologies, the OB and AB maintained the similarities observed in the preload forces curves on Figure 2-9. Figures of the deformed shapes of the spinal cord cross-section at the end of the preload can be found in Appendix C.

2.3.2. CSF pressure distribution

The peak CSF pressure values calculated with each CSF constraint approach ranged between 0.07 and 0.21 MPa across the three morphologies (Table 2-6).

Table 2-6. Predicted peak CSF pressures during impact for each evaluated CSF approach and morphology scenario.

Magnitude	Morphology	CSF containment approach			
		CB	OB	AB	VR
Peak CSF pressure (MPa)	Small	0.21	0.07	0.12	0.12
	Average	0.17	0.09	0.13	0.14
	Large	0.13	0.07	0.10	0.14

The lowest pressures were predicted by the OB method in all the models, while the highest values belonged to the CB method in the small and average models, and to the VR in the large morphology. The CB approach also showed a clear trend of calculating lower peak CSF pressures as the dimensions of the model increased (Figure 2-10). As such, the percentage difference between the maximum and minimum peak pressures

predicted by the CB approach was larger (47%) than the observed ones for the OB (25%), AB (26%), and VR (15%) approaches across morphological models. These variations and trends between peak pressures can be visually observed in Figure 2-10.

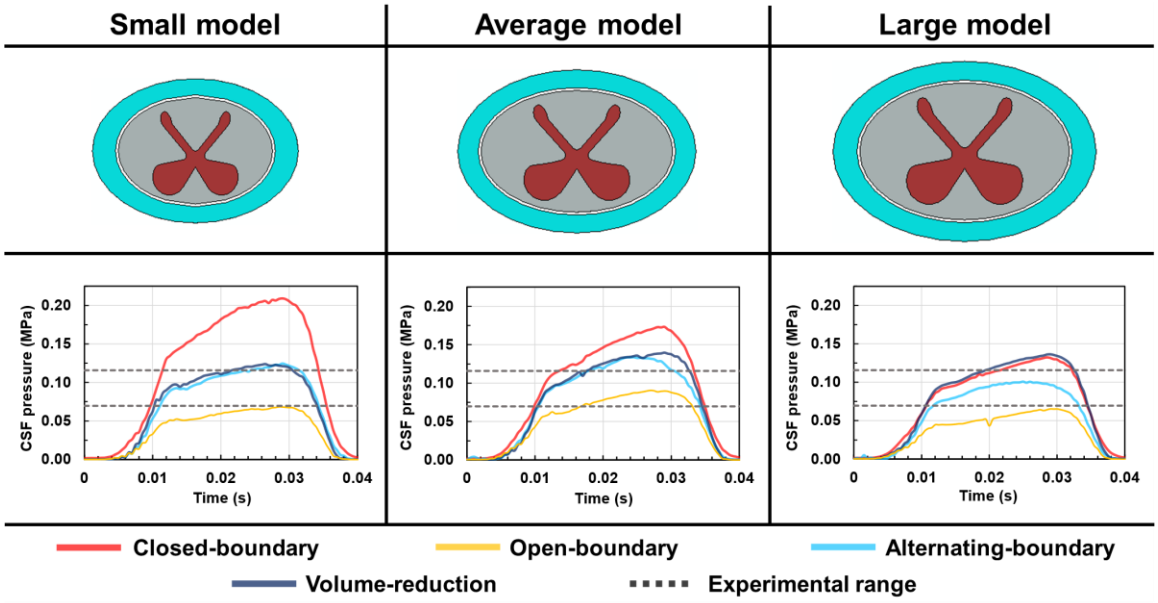

Figure 2-10. Mean pressure values in the SPH particles for each evaluated CSF containment approach and morphology scenarion during the impact phase of the simulations.

The predicted CSF pressures were compared against the CSF data from weight-drop experiments performed by Jones et al. [13] in a porcine model of thoracic SCI. This comparison was possible since morphology studies performed have shown that porcine thoracic and NHP cervical regions can exhibit similar CSF-to-spinal cord ratios regardless of their differences in size [57], [66]. Jones and colleagues [13] reported CSF peak pressures ranging from 0.07 to 0.12 MPa. The predicted pressures from the OB and AB approaches in all three morphologies fell within or close to this experimental range, while for the VR method only the peak pressure in the small model was found between the range proposed by Jones et al. [13]. In the other two morphologies (i.e., average, and large), the VR peak pressures were close to the upper limit of the experimental range, showing only a 15% difference. For the CB approach, the only peak CSF pressure close to the experimental range was reported in the large model (0.13 MPa). For the small and average models, this approach overestimated the pressure magnitude in comparison with the experimental observations by 75 and 42%, respectively.

2.3.3. Stress and strain distribution in the spinal cord

The predicted tissue-level stresses and strains were influenced by the choice of CSF boundary conditions and the cord and column size. In Table 2-7, the 95th percentile values of stress and strain observed in the elements of the spinal cord cross-section at the impact epicenter for the average model were included.

Table 2-7. 95th percentile value and standard deviation (SD) for each mechanical parameters at the time of maximum compression in the small model for each evaluated CSF approach.

Magnitude	CSF containment approach			
	CB	OB	AB	VR
Tresca stress (MPa)	0.50 [0.17]	0.62 [0.21]	0.59 [0.20]	0.93 [0.29]
Max principal strain	0.65 [0.14]	0.72 [0.15]	0.70 [0.14]	0.75 [0.16]
Min principal strain	-1.15 [0.26]	-1.22 [0.29]	-1.19 [0.28]	-1.30 [0.30]

The 95th percentile values were used instead of the mean values since the mean values were similar between CSF boundary conditions and did not properly capture their effect in the tissue-level mechanics. Largest 95th percentile Tresca stress and principal strains (maximum and minimum) were predicted by the VR approach in the small morphology, followed by the OB, AB, and CB methods, respectively. For these mechanical features: Tresca stress, maximum and minimum principal strain, the percentage difference between the VR predicted values and the CB values were 60%, 14%, and 12%, respectively. The distribution of stress and strain values was relatively consistent among the CB, OB, AB, and VR approaches in the small morphology (Figure 2-11).

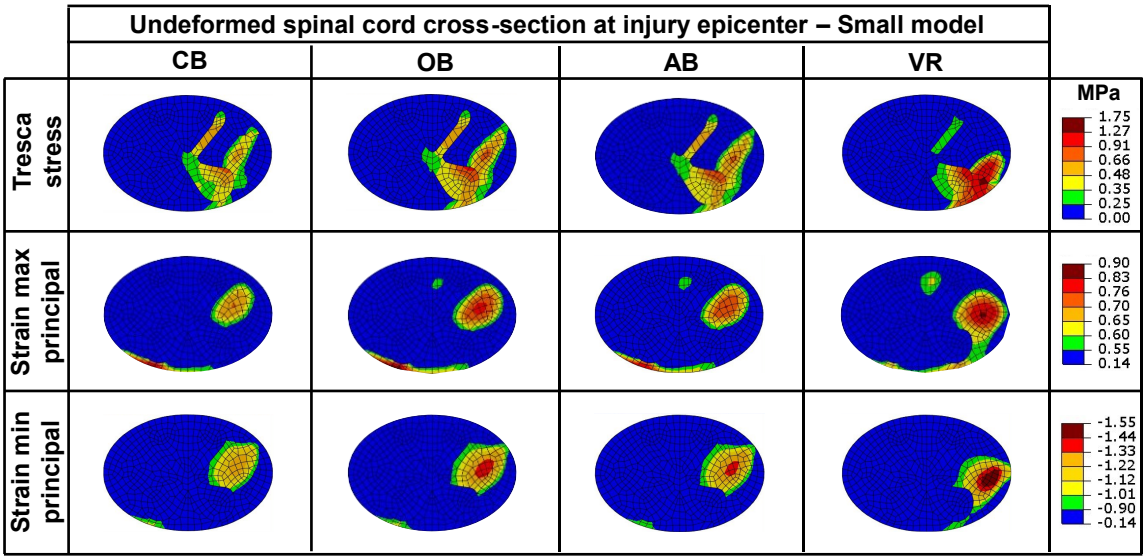

Figure 2-11. Stress and strain distribution at injury epicenter for each evaluated CSF boundary conditions in the small morphology model. Areas in blue experienced low magnitudes of stress or strain, while colored regions reported higher magnitudes. Tresca stresses were concentrated in specific regions: dorsal and ventral horns in GM, and ventral and lateral columns in WM. Higher max and min strain values were particularly observed in the lateral WM column, and in small ventral WM sections on the contralateral impact side.

In the average model, once again the largest 95th percentile Tresca, max and min principal strain were predicted by VR method (Table 2-8), with the OB values as a close second (percentage differences between 0.9 - 12%). The CB also reported the lowest values in all three mechanical parameters. The percentage difference between the CB and VR predicted Tresca, max and min principal strain values were 46, 15, and 14%, respectively.

Table 2-8. 95th percentile value and SD for each mechanical parameters at the time of maximum compression in the average model for each evaluated CSF approach.

Magnitude	CSF containment approach			
	CB	OB	AB	VR
Tresca stress (MPa)	0.45 [0.20]	0.64 [0.23]	0.62 [0.22]	0.72 [0.25]
Max principal strain	0.60 [0.12]	0.69 [0.14]	0.69 [0.14]	0.70 [0.14]
Min principal strain	-1.02 [0.23]	-1.16 [0.28]	-1.15 [0.27]	-1.17 [0.29]

Like the small morphology results, the distribution of stresses and strains at the impact epicenter in the average model was similar between CSF approaches (Figure 2-12).

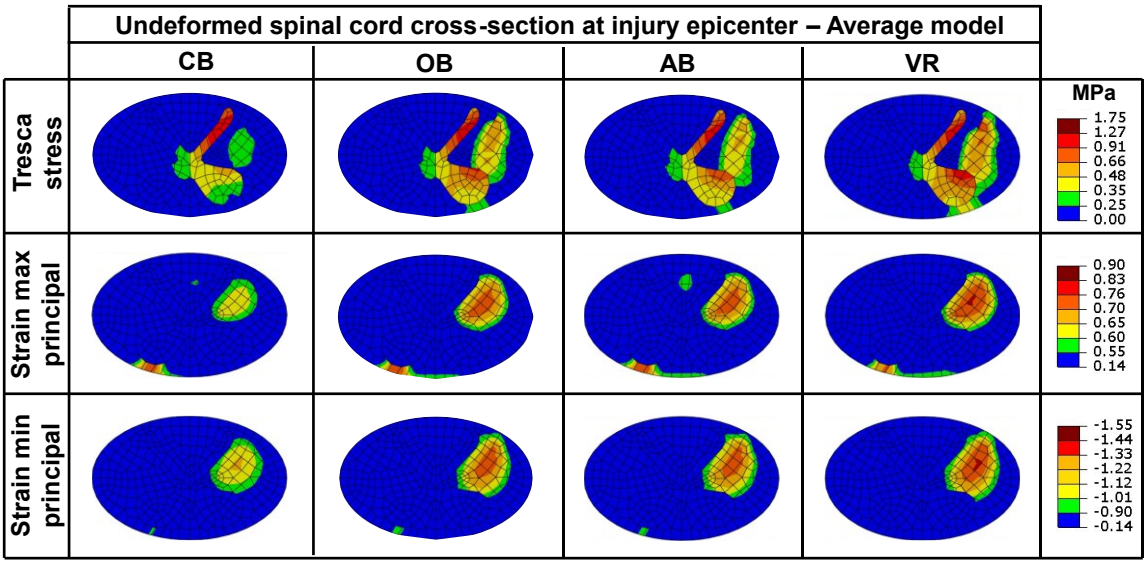

Figure 2-12. Stress and strain distribution at injury epicenter for each evaluated CSF boundary conditions in the average morphology model. Areas in blue experienced low magnitudes of stress or strain, while colored regions reported higher magnitudes. Larger stress values were observed in the dorsal and ventral GM horns, and in the lateral WM column. Higher max and min strains were mostly located in the lateral WM column, adjacent to the dorsal GM horn.

Following the trend of the previous models, the highest and lowest 95th percentile values of stresses and strains were found with the VR and CB approaches (Table 2-9), respectively. In the large morphology, the AB approach showed higher values in all four mechanical parameters than the OB technique, with the percentage differences between their values ranging from 2 to 17%; the greatest difference found in the Tresca stress values, and the smallest in the minimum principal strains. The percentage difference between the highest (VR results) and lowest (OB results) were 28, 12, and 14% for the Tresca stress, max and min principal strain, in that order.

Table 2-9. 95th percentile value and SD for each mechanical parameters at the time of maximum compression in the large model for each evaluated CSF approach.

Magnitude	CSF containment approach			
	CB	OB	AB	VR
Tresca stress (MPa)	0.40 [0.19]	0.42 [0.20]	0.50 [0.25]	0.53 [0.24]
Max principal strain	0.55 [0.12]	0.58 [0.13]	0.60 [0.13]	0.62 [0.13]
Min principal strain	-0.94 [0.22]	-1.01 [0.25]	-1.03 [0.24]	-1.08 [0.25]

Some of the stress and strain distribution trends identified in the small and average cases where also observed in the large morphology model (Figure 2-13).

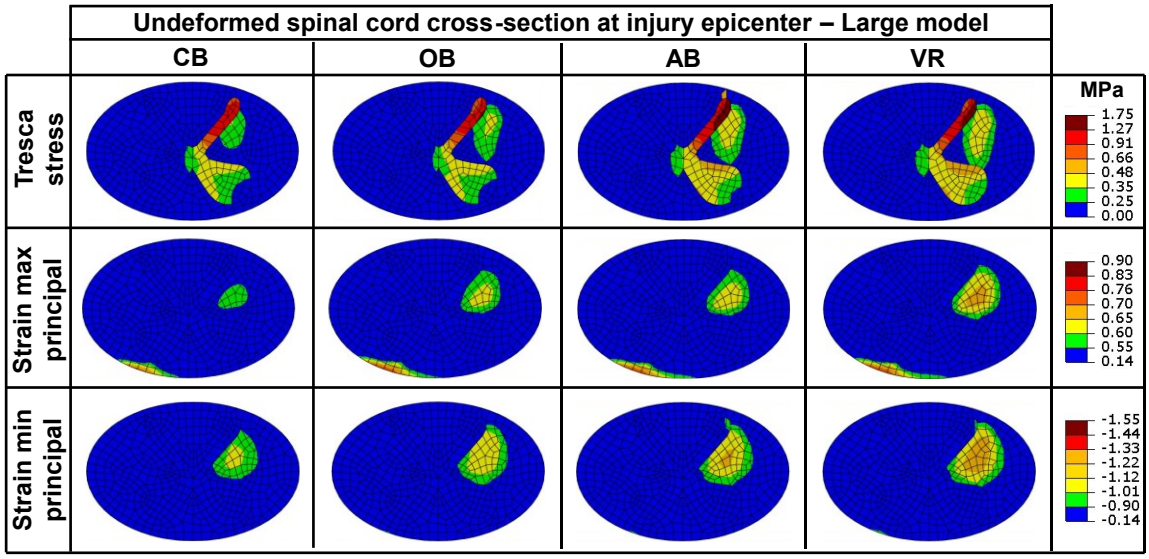

Figure 2-13. Stress and strain distribution at injury epicenter for each evaluated CSF boundary conditions in the large morphology model. Areas in blue experienced low magnitudes of stress or strain, while colored regions reported higher magnitudes. Highest stresses were observed in GM's dorsal horn, with large values also located in nearby regions of the ventral GM horn and the lateral WM column. Most large maximum and minimum strains were located in lateral WM sections immediately under GM's dorsal horn.

The mean 95th percentile values predicted by the CSF containment approaches were also compared across morphologies (Table 2-10). On average, the highest Tresca, maximum and minimum principal strain values were found in the small model, followed by

the average and large morphologies. The standard deviation in mean 95th percentile stress values decreased as the column and spinal cord morphologies increased in size, while the SD values in the evaluated strains showed low variation across morphologies. Moreover, the percentage difference between mean values in the small and large models, which predicted the highest and lowest magnitudes on every parameter, were larger for the Tresca stress (36%) and lower for the maximum principal strain (18%).

Table 2-10. Mean 95th percentile values and SD for each mechanical parameter across morphologies.

Magnitude	Morphology		
	Small	Average	Large
Tresca stress (MPa)	0.66 [0.19]	0.61 [0.11]	0.46 [0.06]
Max principal strain	0.71 [0.04]	0.67 [0.05]	0.59 [0.03]
Min principal strain	-1.22 [0.06]	-1.12 [0.07]	-1.01 [0.06]

2.3.4. Computational times and efficiency

There was substantial variability in computational times for each of the evaluated CSF boundary methods with no consistent trend (Table 2-11). The shortest computational time in the small morphology was obtained with the OB methods, while for the average and large models, the CB provided the shortest computational times. The OB method reported both the shortest (47.9 hrs) and longest (127 hrs) run times across all simulations in the small model and large models, respectively. Meanwhile, the VR method took longer to finish computing than the other approaches in the small (102 hrs) morphology scenario, except in the average model, where the AB method took longer to compute (101.8 hrs). Still, the AB approach showed similar computational times to the CB method in the small (61.1 hrs) and large (71.5 hrs) cases, with a percentage increase in the number of hours no greater than 12.5% between morphologies. Looking at the individual times for each simulation step, it was noticed that preload's computational times comprised between 48 - 59% of the total simulation time for all the models. No other trend was identified.

Table 2-11. Computational times of the FE simulations ran for this study. The percent change between the open-boundary (OB), alternating-boundary (AB), and volume-reduction (VR) approaches was calculated with respect to the close-boundary (CB) method.

Morphology	CSF containment approach	Preload computational time (hours)	Impact computational time (hours)	Total computational time (hours)
Small	CB	27.9	29.7	57.6
	OB	24.0	23.9	47.9
	AB	30.3	30.8	61.1
	VR	55.2	47.1	102.3
Average	CB	27.3	27.2	54.5
	OB	54.0	38.3	92.4
	AB	55.2	46.6	101.8
	VR	44.7	38.5	83.2
Large	CB	32.9	30.7	63.6
	OB	72.6	54.3	127.0
	AB	40.4	31.1	71.5
	VR	62.9	46.1	109.1

2.4. Discussion

FE models are useful tools for understanding SCI biomechanics and recreating injury experiments without running into different logistical and ethical challenges [5], [17], [18], [52], [68]. Based on previous studies [11], [15], for FE models of SCI to be biofidelic and provide more accurate results they should include the CSF. Moreover, the outcomes of other studies have proposed that SPH is an appropriate method for representing the CSF in computational models of SCI [8], [16], [23]. In the literature, SPH has been implemented under different boundary conditions meant to capture the CSF's behavior during impact and its influence in the distribution of forces in the spinal cord [8], [18], [19]; however, the effects of these CSF boundary conditions on the mechanical outcomes of the FE models have not been analyzed. Since FE models are a complementary tool for studying the correlation between tissue-level mechanics and damage after SCI [8], [9], [18], it is critical to understand if modelling choices, such as the definition of boundary conditions to constrain the CSF, are affecting the predicted results. Motivated by this need, and the observations from [57] and [66] in their large animal studies regarding the effect of morphology on SCI injury outcomes, in this work we compared both the effect of

different CSF boundary conditions and spinal cord and column morphology on the mechanical outcomes of FE models of SCI based on NHP experiments.

2.4.1. Impactor's displacement and reaction forces

In the NHP contusion experiments [47] with similar impact parameters as the simulations, the reported mean preload and total displacements were 2.8 and 6.4 mm. Comparing these values with the calculated displacements in the FE models, it is observed that the simulations underestimated the impactor's displacement. Among the evaluated approaches and morphologies, VR showed the largest preload displacements, which were still between 24-29% shorter than the experimental mean. Since the preload step defines the starting point for the impact, and the results indicated that it stops at shorter displacements than the experimental mean, this difference is carried on to the calculated total displacement too. One possible explanation for these variations is that the actual preload step in the experiments occurs at a slower rate than in the simulated preload step [47]. The same rate was not implemented in the models, as it significantly increased the computational time (>350 hrs). Given the viscoelastic nature of most included materials, this is a likely that increasing the preload rate will affect the behavior and response of the model. Another reason, perhaps related to the previous point, could be that the material properties included in the FE models predict a stiffer response from the spinal cord and meninges system during the preload phase. The stiffer response makes the FE models reach the preload force threshold sooner, which triggers the impact step from a higher location.

The difference in results could also be related to the experimental variability observed during the injury procedures. In [47] and previous computational studies recreating the NHP experiments [18], [19], [57], it has been suggested that the variability in the acquired results during the injury process can be related to both the morphological differences in the subjects, and the impact protocol choices. Although these experiments are performed by carefully following the established protocol, the surgeons and technicians involved still need to make some manual decisions, such as visually defining the spinal cord midline, or stopping the impactor after reaching the preload force threshold. These manual parts of the procedure can introduce variability in the experimental results that may not be captured by the FE model. Moreover, some observations from the surgical procedures of the NHP experiments indicate that there could be a small degree of

displacement of the animal subject's body during the impact experiments due to issues with the clamping mechanism that holds their spinal column. This displacement would prevent the impactor from reaching the preload force threshold sooner, since it would move the spinal cord and column in the same direction and would affect the displacement reported after the impact.

The variability in the displacement and force results (Table 2-3) reflected the adaptability of each CSF constraint method to the morphology scenario. For example, while the CB and VR approaches have fixed amounts of particles representing the CSF that do not change throughout the phases of the simulations, the number of particles that leave the subarachnoid space during the preload phase in the OB and AB approaches was different depending on the morphology and specific mesh size. Based on the acquired results, the OB and AB methods allowed for a faster preload step than the VR method, yet they predicted shorter impactor's displacements during this phase of the simulations. Despite the VR method calculating impactor's displacements closer to the experimental data, it was noticed that the fixed amount of CSF volume reduction of 86 mm3 had a particularly large effect in the small morphology compared to the larger morphology models. Even though this volume reduction only represented the 17% of the original CSF volume in the small morphology, the overall behavior of the model was significantly less stiff. This resulted in additional spinal cord compression during the preload and lateral shift during the impact, suggesting that to improve the implementation of the VR approach it would be necessary to adjust the CSF volume reduction to the morphological case, particularly with smaller cord and column dimensions. It was observed at least one layer of SPH particles under the spinal cord before the impact, which could have contributed to increasing the reported peak impact forces. For the OB, AB, and VR methods, this is an area of future improvement since a better displacement of these particles could help better recreate the preload and impact phases of the experiments.

Our calculated force values were also compared against other computational studies that have recreated the NHP experiments proposed by Salegio et al. [47] using FE models. For instance, in Jannesar et al. [18], the range of impact reaction forces calculated by their generic models were found approximately between 12 and 18 N. It is likely that the modifications explained in the methods section are the cause of the variance in results. For example, the location of the spinal cord with respect to the subarachnoid space, that in [18] was defined at the bottom of this area in order to facilitate the preload

step, in the present work it was defined at the middle of the subarachnoid space, since it was a more biofidelic choice. Still, this choice implies more movement for both the SPH particles and spinal cord, which would be different depending on the CSF containment approaches and would affect the preload and impact results and as a result, increased computational time. Additionally, Jannesar and colleagues [18] used the input file methodology to define the SPH conversion for the CSF solid, which could introduce some variability in the calculation of the volume of the SPH particles. For SPH, it is recommended to have a uniform mesh, since the characteristic length used to calculate the particle's volume is constant for all the elements. Having the spinal cord at the bottom of the dura mater would result in a moon-shape solid for the CSF, where it could be difficult to have a uniform mesh, resulting in disproportionate particle volume depending on the characteristic length used for the analysis.

In Obaid et al. [19], the reported peak forces for their FE models using impactors of 4 and 5 mm, and with a mediolateral alignment of 0.5 and -1 mm, ranged from 15 to 23 N. Although there were some overlapping values between Obaid and colleagues results with the range of predicted forces from the FE models of this study (20.17 - 28.61 N), it was noticed that our models showed overall larger peak forces. However, it is important to point out that the models in [19] included a homogenous cord, which means that the same material properties, taken from Maikos et al. [9] experiments in rats, were assigned to the entire cord. Meanwhile, the models described in this study included individual material properties and mesh elements for the GM, WM, and pia mater. Based on the findings of previous studies, these differences in material properties and mesh elements are likely responsible for the differences in peak reaction force values. For example, the research in [112] highlighted that including the pia mater around the spinal cord on FE models recreating bovine SCI experiments resulted in a maximum compression reduction of 9% on average during impact. Moreover, the material model used for the WM in this study was developed in [10] to capture the transverse anisotropy observed in this spinal cord tissue because of the aligned set of axons. It is possible that the two combined effects had an influence on predicting higher reaction forces than the results in [19].

It was also noticed that preload peak forces influenced the level of dorso-ventral compression in the spinal cord before the impact (Table 2-5). The VR and CB methods, which reported the highest and lowest preload forces respectively, also predicted the largest and lowest amounts of dorso-ventral compression for the spinal cord. This is a

relevant observation, since subjecting the spinal cord to different amounts of preload dorso-ventral compression, implies that the final compression results will also vary and will influence the magnitudes of strains in the spinal cord tissue. These variations in preload forces seemed to be mostly related to the CSF containment method employed, which highlights the relevance of evaluating and carefully choosing the boundary conditions defined for the CSF to improve the accuracy of the FE results. Still, morphology also plays a role in these outcomes. For instance, the results in the small morphology showed that the CSF containment approaches stopped at lower preload force magnitudes before transitioning to the relaxation time than in the other two morphologies. It is possible that the smaller dimensions in the spinal cord and meninges of this model, in combination with the smaller thickness of the CSF layer, contribute to have a faster force increase that was not captured with the sampling rate defined. Oscillations were also observed in the preload force profiles and were found to be caused mostly by the movement of SPH particles, which was influenced by the reshaping of the spinal cord during the relaxation phase, and the degree of lateral displacement in the spinal cord experienced as the impactor moved towards it.

2.4.2. CSF pressure distribution

The implemented CSF boundary conditions and the spinal cord and dural space morphology had influence in the predicted CSF pressure in the FE models. For example, the CB approach reported the highest peak pressure values in two out of the three morphologies studied. This was expected since the CB approach limited the displacement of the CSF particles during the preload, which resulted in additional pressure during the impact. However, the effect of this accumulated pressure was reduced as the spinal cord and dural space dimensions increased. A possible explanation for this trend is the effect of using the same impact parameters for each morphology case. In a model with a smaller cord and dural space, the impactor will occupy a larger proportion of space in the model after its final displacement than it would in a larger morphology, contributing to a larger accumulation of pressure. Meanwhile, the OB method predicted the lowest CSF peak pressures in all three morphologies. It was expected this boundary condition would predict lower CSF pressure values than other methods, since the OB approach allows the free flow of the particles representing the CSF during both preload and impact phases. The

results were consistent across morphologies, showing that this boundary condition was not highly affected by the dimensions of the spinal cord or dural spaces.

Regarding the AB and VR methods, they predicted similar CSF peak pressures in the small and average morphologies. In the large model, the VR method calculated a larger peak CSF pressure than the AB approach. Even though these two methods account for the CSF displacement during the preload while still considering its mechanical effect during the impact, the CSF pressure results highlight important differences between the two. For instance, it was observed that the VR pressure predictions between the average and large models were almost identical, despite their differences in cord and subarachnoid space sizes. This similarity in pressure outcomes can be related to having reduced the same amount of CSF volume for all the models. For the small, average, and large models, the volume reduction of ~86 mm^3 represented only a 17, 15, and 12% of the starting CSF amount, respectively. Since in an FE model with larger morphological dimensions the number of particles will be larger, it is possible that the 15 and 12% volume reduction in the average and large models lead to equivalent amounts of CSF, resulting in similar pressure outcomes. This observation suggests that more accurate CSF pressure results can be obtained with the VR approach if the CSF volume reduction is tunned to the morphological dimensions prior to the simulation. Although, it is possible that similar outcomes can be accomplished by implementing the AB method instead. This method is strongly influenced by the preload step, that can behave differently depending on the morphology of the FE model and the rate of preload application. As such, the number of particles that will get displaced outside of the dural space will change depending on the morphology, without the need of additional adjustment prior to submitting a simulation.

Depending on the morphology of the model, different boundary conditions predicted CSF peak pressures close or within the experimental observations in large animal SCI by Jones et al. [13]. In the small morphology, none of the boundary conditions predicted CSF peak pressures within the experimental range, although the AB & VR, and the OB pressures were close to the upper and lower limit of the range, respectively. These discrepancies can be linked to the use of the same impact parameters regardless of the morphology. They might be too severe for a small morphology, resulting in overestimation in the CSF pressure even with the boundary conditions that allow for the CSF displacement during the preload. In the average model, the predicted CSF pressure by the OB approach was found between the range, while for the large model it was the CSF

pressure predicted by the AB method. The capabilities of the evaluated boundary conditions to predict CSF pressures within the experimental data available can be a key criterion for selecting the CSF boundary conditions to implement in FE models of SCI.

Even though not all the different CSF containment approaches captured its biomechanical pressure effect during the simulated SCI scenario, more exploration could be done to validate if they could be useful for recreating other clinical conditions related to SCI. For example, research has found that after the age of 60, there is a significant reduction of CSF pressure in humans [119], while at the same time there has been an increase in the proportion of SCI patients above 50 years of age [6]. Based on the lower predicted CSF pressures, boundary conditions such as the ones defined for the OB or AB approaches could help better recreate SCI in older adults, where the CSF pressure would be lower. On the other side, medical conditions like degenerative cervical myelopathy, can induce an increase in patients the intracranial pressure exerted by the CSF to the CNS [120], making them predisposed to SCI resulting from low-energy impacts [121]. The resulting increase in CSF pressure resulting from this condition could be represented with the CB approach or with an adapted version of the VR approach, given that these two methods showed to overestimate the CSF pressure during SCI depending on the morphological dimensions.

2.4.3. Stress and strain distribution in the spinal cord

The predicted tissue-level stresses and strains of our FE models based on NHP experiments were compared against other computational SCI studies. Maikos and coworkers [9] simulated a weight-drop injury on the thoracic spinal cord of rats and predicted maximum principal strains below 0.28. These strain values were lower than the predicted values of our FE model based on NHPs. Russell and colleagues [8] reported values of maximum principal strain no greater than 0.6 in their rat cervical contusion FE models. These strain values were closer to the findings of this study, although their predicted magnitudes were still lower than the peak values in our FE model based on NHP experiments. Other FE studies of SCI in rats also reported stress values [9],[122], however it was not possible to compare against their findings, since they only reported Von Mises stress values. In our FE models the Von Mises stress was not evaluated, since the material properties for the WM capture the non-linearity and anisotropy of this tissue [10], and the

Von Mises is meant only for linear isotropic materials [123], and has shown limited capabilities to capture the anisotropic nature of other biological tissues [123].

Comparing against FE models based on NHP experiments, it was also observed that our simulations predicted stress and strain values in similar orders of magnitude. Sparrey et al. [17] model of cervical SCI on NHPs reported peak maximum principal strains above 0.2 on the ipsilateral impact side at similar locations as our FE models. In these areas, it was observed that the predicted strains in our models ranged between 0.23-0.3, close to the results in [17]. Jannesar et al. [18], using their subject-specific FE models of SCI in NHPs, reported similar values for the minimum (0 to -1.5) and maximum logarithmic strain (0 – 0.8). However, their values for Tresca stresses (0 – 1.0 MPa) were lower than the predicted ones in this document. The differences in the tissue-level mechanical outcomes between our study and [17] or [18] are related to the differences in material properties, the definitions of contact properties, the method for representing the CSF, the complexity of the models' geometries (i.e., simplified vs subject-specific), and the CSF boundary conditions.

It was observed that the CSF boundary conditions had limited effect in the magnitude or location of the stresses and strains in the spinal cord. Still, the VR method predicted the largest peak values for all the evaluated mechanical parameters in every morphology scenario. These outcomes were most likely linked to the larger impactor displacement that was predicted by this boundary condition across all morphologies. The impactor's displacement during the impact step was the same for all the models, however, the preload displacement varied for each morphology as it took different amounts of displacement to reach the force threshold. Using the VR approach in the small model, resulted in more spinal cord lateral shift during the impact, which changed the location of stresses and strains in comparison with the other boundary conditions. These discrepancies were not observed in the average or large models.

The morphology of the FE models affected the location and magnitude of stress and strain values in the spinal cord cross-section. These results were influenced by the impact parameters, since depending on the morphology, the spinal cord was subjected to different amounts of compression. For the same impact parameters, more compression was observed in the spinal cord cross-section of the small model (Appendix B). This amount of compression decreased as the cord dimensions grew larger and resulted in

lower strain values. These differences in compression, as well as the lateral shift of the spinal cord, contribute to the dorso-lateral change in the location of stress values depending on the evaluated morphology. Dorso-lateral shift in the strain values was observed between the small and average models, but it was less evident between the average and large morphologies.

The changes in the location of higher stress and strain values through the spinal cord cross-section between morphologies is an important point of discussion. It is known that the location of the tissue damage in the spinal cord would determine the functional impairments [3], [36]; additionally, previous research has suggested the correlation between high levels of stress/strain and tissue damage after SCI [4], [5], [8], [9], [18], [94]. Based on that information, the different locations of high stress and strain values in the spinal cord cross-section suggest that using the same impact parameters could result in different functional outcomes for NHP subjects with different morphologies. Previous studies have already pointed out that there is large variability in spinal cord morphology across NHPs [47], [48]. As such, our results suggest that accounting for the morphology of the subjects in the SCI experiments could help to improve the consistency of the injury and functional outcomes in the animals, so it can be possible to better assess the efficacy of potential treatments. One possible way to address this variability can be to define subject-specific impact parameters, which has been previously proposed by other researchers doing FE models to recreate SCI experiments in animals [49]. Subject-specific impact parameters could allow scientist to generate injuries located in the desired spinal cord sections regardless of the spinal cord and subarachnoid space dimensions of the NHP subject.

2.4.4. Computational time and efficiency

The observed differences in computational times between the simulated models can be linked to both the implemented CSF boundary condition and the evaluated morphologies. For instance, the CB, OB, and AB approaches include the same amount of SPH particles representing the CSF in the FE models. However, the number of interactions or the amount of displacement the particles experienced was different depending on the boundary condition. In contrast, the VR approach always started with a lower number of particles representing the CSF, which was expected to make this method more efficient than the PB approach. The results showed that this was only achieved for

the average morphology, since in the small and large models, the PB was more computationally efficient. These observations suggest that in most of the morphological cases, it was more computationally efficient to account for the set of particles that left the subarachnoid space of the FE model, than to compute the additional displacements and interactions of the particles resulting from the VR method.

The effect of morphology in the computational times was most likely associated with its influence in the number of CSF particles and the changes in mesh pitch size in the FE models. For instance, it was observed that the number of particles needed for representing the CSF increased as the spinal cord dimensions grew larger. This had a particular effect in the computational time of the models using the OB approach, where it was observed that the computational time increased as the number of CSF particles increased. In the small and large models, the spinal cord meshes were refined in comparison to the average model to avoid some mesh quality issues reported by ABAQUS. However, a finer mesh in these models resulted in an increased number of elements, which could have further influenced the time required for computing. Although, it appeared like the increased number of elements in the spinal cord had limited influence in FE models using the CB approach, as the computational times were similar across morphological cases.

Based on the acquired results, it was noticed that the SPH mechanisms have a strong influence in the computational times of the simulations. The analyzed mechanical outcomes and the previous observations of the SPH performance in other FE models [8], [18], [19] highlight that this method can accurately capture CSF behavior in computational models of SCI. Still, the accuracy of this method showed to come at a computational efficiency cost. Unlike other FE methods, SPH cannot be readily parallelized in ABAQUS [21], resulting in considerable computational costs. This reduces its current suitability for conducting large, parameterized simulations of SCI, such as subject-specific models, or its implementation in a more clinical setting, where outcomes would be expected in a shorter period. Although computational time should not be the only factor to consider, it can be a useful metric to account for when selecting the CSF boundary conditions to implement in a FE model of SCI with preload.

2.5. Conclusions

The findings of this work provide useful information regarding the choice of CSF boundary conditions and its effect on the biomechanical response of FE models of SCI with preload using SPH to represent the CSF. The acquired results showed that the CSF pressure and computational times were closely influenced by the choice of boundary conditions. The morphological dimensions of the model had a strong effect in the impact reaction forces, and the magnitude and location of tissue-level stresses and strains in the spinal cord. Overall, the AB boundary condition proved to be a better option for capturing the CSF biomechanical effect in FE models of SCI with preload based on NHP experiments. Even though this approach did not provide the best results in all the evaluated scenarios, its adaptability to the morphological dimensions of the models without the need for changes in FE model prior to simulation is a great advantage. The VR method also showed promising results in some scenarios, however, it was usually more computationally expensive than the AB method. Using the same impact parameters for different morphological scenarios resulted in variance in the general and tissue-level mechanical outcomes of the models. These variations in the results suggest that more consistent injury outcomes could be acquired by defining subject-specific impact parameters, that could be defined with the help of FE models of SCI. These advances will contribute to making computational models a better tool for assisting in the development or improvement of injury protocols in animals, and helping to the study of SCI.

Chapter 3.

Identification of injured elements in computational models of spinal cord injury using machine learning

Effective SCI prevention design requires knowledge of the magnitudes of mechanical loading that result in tissue damage. FE models of SCI provide detailed information of tissue-level mechanics and can be used in combination with histopathological data to define the link between load and injury. As such, the purpose of this study was to correlate tissue mechanics and damage in a computational model of NHP SCI. Three datasets corresponding to GM, WM, and the combination of gray and white matter tissues were used to train ML algorithms to identify tissue damage based on the mechanical outputs of FE models. The datasets were built from the comparison of histological images from SCI experiments in NHPs and subject-specific FE models. The classification performance of four ML algorithms (logistic regression, decision trees, support vector machines, and k-nearest neighbours) were evaluated and compared using cross-validation and the area under the receiver operating characteristic curve (AUC). After hyperparameter tuning, the AUC mean values for the algorithms ranged between 0.79 and 0.82, with a standard deviation no greater than 0.02. K-nearest neighbors and logistic regression algorithms were better at identifying injured elements based on FE mechanical predictions than support vector machines and decision trees. The outcomes suggest that the ML algorithms have different sensitivity to the skewed distribution of classes in the studied datasets, and that identifying damage simultaneously in the gray and white matter tissues showed no advantages over studying each dataset separately. Minimum principal strain and logarithmic strain in the axonal direction had the strongest influence on tissue damage identification for the GM and WM, respectively. Correctly classified healthy and injured elements in both GM and WM sets showed wide and overlapping ranges of mechanical values, yet it was possible to identify mechanical values corresponding only to injured samples that could work as ‘thresholds’ for identifying tissue damage after SCI. These thresholds indicated that the GM tissue is more susceptible to minimum and maximum principal strain values than the WM, while the last one has a lower tolerance to Tresca stress and logarithmic strains in the axonal direction than the GM. These approaches will contribute to improving the current understanding of the

relationship between mechanical loading and tissue damage during SCI and will have implications for the development of prevention strategies for this condition.

3.1. Introduction

SCI is triggered by mechanical loading, which causes a series of biological responses resulting in irreversible functional damage to the neurological system [4]. Understanding the relationship between mechanical loading and tissue damage would help to establish design criteria for protective equipment, and for clinicians to select the most appropriate treatment to implement [8], [17], [18]. In addition, the relationship between tissue mechanics and injury can inform the design of animal model systems and improve the consistency in injury outcomes for variable animals [17], [18]. Having a preliminary insight into the mechanical loading distribution in the spinal cord and the subsequent injury outcomes could provide useful information to define mechanical threshold values that will result in tissue damage.[8], [17], [18] For these reasons, several studies have looked to establish the relationship between mechanical loading and tissue damage in the spinal cord [8], [9], [18], [94]. However this relationship is not yet well defined, particularly in large animal models, that are more representative of human injury [3], [6], [47].

Integrating computational FE models with histopathological findings from SCI experiments provides the opportunity to correlate mechanical loading and tissue damage [9], [17], [18], [54]. Previous studies, using rat [8], [9] and NHP [18] models, utilized statistical methods such as linear and logistic regression to establish correlations between mechanical features — such as maximum principal strain [8], [9], [94], and Von Mises and Tresca stresses [18] — and biological damage in the spinal cord tissue. Notably, these endeavors underscored the association between these mechanical features and damage in the GM and WM tissues of the spinal cord. However, establishing clear injury thresholds has proven challenging, since research findings have indicated different levels of correlation and tolerance between each spinal cord tissue and different mechanical features [8], [9], [18]. Moreover, threshold values reported from animal models have varied across species [8], [18] or the results have not suggested a clear value after which it is possible to identify tissue damage [8].

Current applications of artificial intelligence on SCI research [97], [124], [125] and as a tool for integrating FE and experimental data in other engineering scenarios [90], [91], [92], suggest it can help with some of the challenges of studying the complex correlation between mechanical loading and tissue damage. ML algorithms have been used in combination with imaging technologies, such as MRI, to identify lesions and damage to the spinal cord [97]. Other applications of ML algorithms have used clinical data to predict changes in functional outcomes after treatment [97], [125], and to assess the pain in patients with SCI [124]. These studies leverage the advantages of ML algorithms to understand complex relationships between SCI-related variables [97], [124], [125]. Additionally, the methodologies presented in [90] and [92], where experimental or clinical data were employed along with mechanical results from FE simulations to train different ML algorithms for bridge damage and hip fracture detection, further motivates and supports the exploration of ML in establishing a relationship between tissue mechanics and tissue damage in SCI.

Within these research studies, a broad range of ML algorithms have been applied. Each algorithm has capabilities and advantages worth exploring for the purposes of the study. For instance, LR was used in previous SCI work to fit mechanical estimations from FE models with injury status [9], [18], which would facilitate comparisons across studies. DT are versatile and have the potential to be upgraded to a Random Forest classifier. SVM is capable of discerning complex decision planes between several features [95], [96], which could be highly relevant since studies have suggested that SCI is most likely the product of the combined effect of multiple mechanical parameters [126]. Lastly, KNN is both adaptable [103] and can provide insights regarding the spread and similarity [95], [103] of values between injured samples.

We hypothesized that using different ML algorithms could improve the identification of injured elements in both the GM and WM tissue based on mechanical loading predictions from FE models of SCI. This is because depending on the ML algorithm, the criteria or approach to analyze the data provided will be different, providing a flexible approach to find correlations between variables [100]. Furthermore, employing different ML algorithms could help circumvent the different levels of correlation between the mechanical features and the damage in the GM and WM, since it is possible that different methods will prove to be better at identifying damage for a specific tissue. By using ML approaches, our study aims to contribute to a comprehensive understanding of

tissue damage identification post-SCI, with implications for clinical practice and further research.

3.2. Methods

An experimental NHP cervical spinal cord contusion dataset [18] trained four classification ML algorithms from the scikit-learn library [127]: LR, DT, SVM, and KNN to identify damaged or healthy tissue. The classification performance of each model was evaluated using the area under the ROC curve (AUC) score for the spinal cord GM, WM, and whole cord. This score was also used to select the best algorithm for identifying injured elements on each dataset. The relevance of the included mechanical features and the mechanical values reported for samples with an injury probability equal or greater than 50% for each of the selected algorithms were also requested and compared against findings in the literature.

3.2.1. Dataset details

Pre-injury MRI scans taken from three NHP subjects were used to develop subject-specific FE models matched to *in vivo* experiments (Figure 3-1 C) [18]. The results from the FE models of the spinal cord tissue were segmented into WM and GM elements (Figure 3-1 E). The dataset consisted of five mechanical features with the most relevance and correlation with tissue damage [18]: min/max principal logarithmic strain (LEP), logarithmic strain in the longitudinal or axonal direction (LEAXON), Tresca stress (TRESCA), and strain energy density (ESEDEN). Structural tissue damage in the spinal cord was observed from cross-sectional histological slices from each subject at a mean time of 20 weeks post injury (Figure 3-1 B), with a standard deviation of 0.47 [47]. Overlaying the histology data on element slices from the computational models, each element was assigned into one of two target classes: injured (1) or healthy (0).

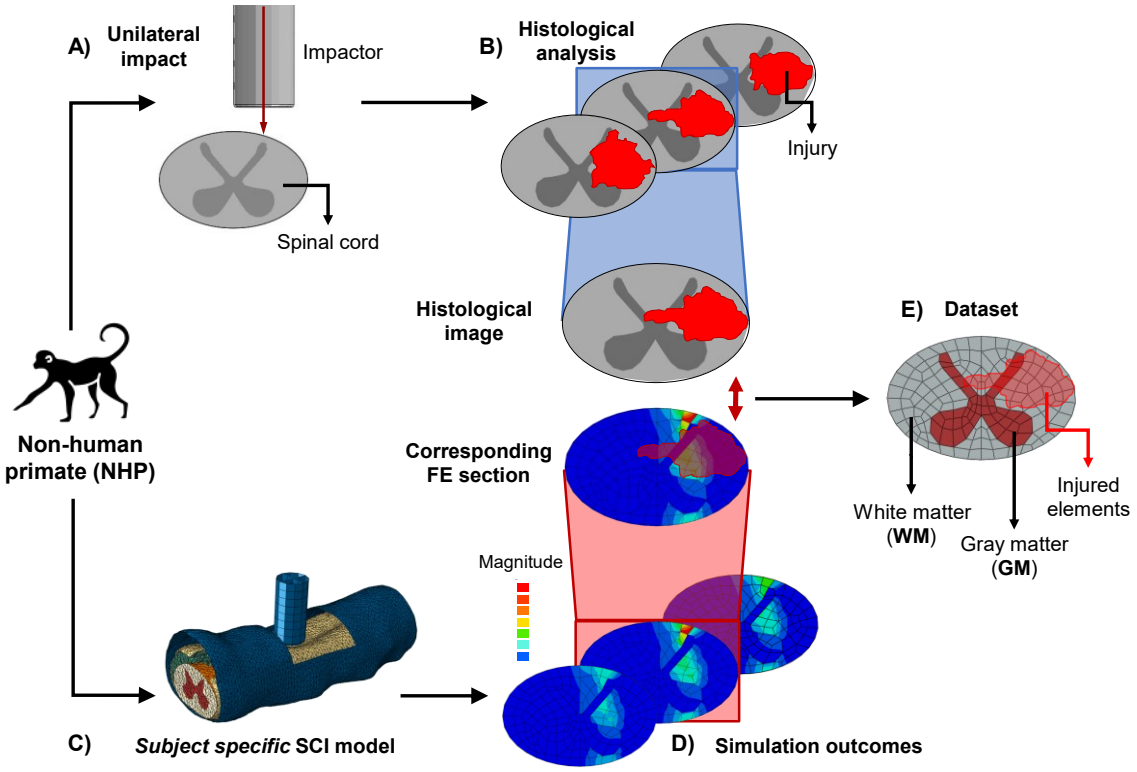

Figure 3-1. Diagram of the spinal cord tissue datasets generation for training the ML algorithms. Weeks after unilateral impact SCI experiments (A), a histological analysis was performed on the spinal cord of NHP subjects in [47] (B). The experiments were recreated using subject-specific FE models (C), and the simulation outcomes (D) compared against histological images. For the gray and white matter sections, the elements located inside the injury area were labeled as injured, and their values were exported as coma separated files.

After having been assigned to a target class, the elements from the FE models were used to create three datasets across all subjects: GM elements (GM-only), WM elements (WM-only), and combined GM & WM elements (GM&WM) to explore the differences in predicting tissue damage in the spinal cord based on evaluating GM-only or WM-only, or combined tissue elements, GM&WM. The experimental SCI were unilateral and mild, resulting in more healthy elements in the datasets than injured elements. In addition, there were more WM than GM elements in the dataset due to the tissue distribution in the cervical spinal cord. These uneven distributions of data per tissue type and target value (healthy/injured) were accounted for in the training and implementation of the ML algorithms using their internal method to balance the class weights.

3.2.2. Data pre-processing

The datasets were imported and converted into data frames (pandas' library, Python). The datasets were checked for duplicate values and redundant features, and then split into train, validation, and test datasets with 70%, 20%, and 10% of the original dataset respectively, using the train_test_split_ function [127]. To keep the original class distribution in the split datasets, the 'stratify' parameter was set (Table 3-1). Datasets from GM-only and WM-only were concatenated into a new dataset as GM&WM dataset. To distinguish GM and WM, a new feature column 'TissueType' was included in the dataset. This new feature had binary values, with '0' representing the GM and '1' the WM samples.

Table 3-1. Number of *healthy* and *injured* elements after each dataset split.

Dataset	Train		Validation		Test	
	Healthy	Injured	Healthy	Injured	Healthy	Injured
GM-only	965	553	276	158	138	79
WM-only	3952	1202	1129	344	565	172
GM&WM	4916	1755	1406	502	703	251

3.2.3. Parameter tuning and cross-validation

To compare the performance of the four ML models on each dataset, a 10-fold cross-validation (CV) [127] and the AUC metric were employed. K-fold was combined with shuffle splits to generate randomized sets that preserved the class distribution of the original set. Each algorithm was first fitted to the training portion of the data and then the validation set was used to find the best hyperparameters for each ML algorithm using a randomized search CV function [127]. In this context, the term hyperparameter refers to the set of internal and tunable parameters characteristic to each ML algorithm [128]. These hyperparameters were set before the learning process began and they affected the training of the algorithms [128], which made it important to properly define their values to have reliable classification or prediction results. To avoid overfitting during the hyperparameter optimization, an additional 5-fold stratified shuffle split was included in the CV parameter of the randomized search function (Table 3-2).

Table 3-2. The range of randomized search parameters evaluated for each ML Algorithm during hyperparameter tuning.

General & algorithms' parameters			
n_iter = 50		scoring = roc_auc	
LR	**DT**	**SVM**	**KNN**
C: loguniform (1e-5, 100)	Criterion: gini, entropy	C: loguniform (1e0, 4e2)	n_neighbour: range(1, 100)
Solver: liblinear, lbfgs, newton-cg	min_samples _split: range (2, 80)	Gamma: auto, scale	Weights: uniform, distance, none
Class_weight: balanced, none	Splitter: best, random	Kernel: rbf, poly, sigmoid	-
-	Class_weight: balanced, none	Class_weight: balanced, none	-

The mean and standard deviation (SD) values for the balanced accuracy, precision, recall, F1 score, and AUC metrics were calculated for each algorithm after the 10-fold CV. Only the AUC values were reported since it was selected as the decisive metric. For each dataset, the algorithms and set of tuned parameters with the highest mean AUC score after the 10-fold CV were selected for the final test. Each dataset was split again into new training and test sets, where the initial validation and test sets were combined into a larger evaluation set (30% of the original data) and used to train and test the best performing algorithms with tuned parameters. The accuracy, precision, recall, F1 score, and AUC metrics were calculated.

3.2.4. Feature importance and range of values on injured elements

From the results of the selected and tuned ML algorithms for the GM and WM datasets, the mechanical values of all the samples correctly classified with an injury probability above 50% were requested using inverse prediction, as well as the coefficient of importance for each mechanical feature. The combined GM&WM set was excluded from this analysis, since the spinal cord tissues do not share the same mechanical features, and it would be difficult to isolate the effect of mechanics on the gray and white matters and their different tolerances to stress and strain values. The predicted probability for each sample of the test set to be classified into one of the two classes was requested. After, the index of all the samples with a predicted probability of injury greater than 50% were located, saved, and compared against the index number of the samples that were indeed injured samples. By doing so, the final list of index numbers corresponded only to

the ones belonging to the samples correctly predicted as injured. Using built-in scikit learn functions, the maximum, minimum, mean, and standard deviation values were calculated from the final list of samples for each mechanical feature.

Feature importance was extracted using available Python functions for the LR and DT algorithms. Since KNN and SVM algorithms do not support the same functions for requesting feature importance, an iterative approach followed the method of other medical classification studies [129] to determine which features had a higher contribution in the calculated AUC score [129]. This approach consisted of training the KNN and SVM algorithm after hyperparameter tunning with one mechanical feature at a time, then proceed with the testing of the algorithm and requesting the AUC score at the end of each iteration. The AUC values acquired by the algorithms with each individual mechanical feature were reported, and the one with the highest score was selected as the more relevant one.

3.3. Results

3.3.1. Parameter tuning and cross-validation

The AUC values acquired with each ML algorithm were relatively similar across datasets (Table 3-3). The KNN algorithm was most effective for the GM-only set while LR showed the best classification performance for both the WM-only and GM&WM sets, although with different hyperparameter values (Table 3-3).

Table 3-3. CV Mean [SD] AUC values for each ML algorithms after hyperparameter tuning.

	LR	DT	SVM	KNN
GM-only	0.82 [0.01]	0.82 [0.01]	0.82 [0.01]	0.83 [0.01]
WM-only	0.81 [0.01]	0.79 [0.02]	0.80 [0.02]	0.79 [0.02]
GM&WM	0.82 [0.01]	0.80 [0.02]	0.80 [0.02]	0.80 [0.02]

The KNN algorithm best performed when considering 32 neighbors around the point of interest, and with distance-based weight for the class labeling (Table 3-4). For the LR algorithm, the C parameter value represents the strength of the regularization executed on the data before classification.

Table 3-4. Best performing ML algorithms for each dataset with the corresponding set of hyperparameters.

	Dataset		
	GM-only	**WM-only**	**GM&WM**
ML algorithm	KNN	LR	LR
Tuned parameters	n_neighbors: 32	C: 3.756	C: 50.745
	weights: distance	solver: newton-cg	solver: liblinear
	-	class_weight: balanced	class_weight: balanced

Comparing the best algorithms' performance on each dataset and the evaluated metrics (Figure 3-2): accuracy, precision, recall, F1 score, and the AUC show that most of the metrics scores obtained by the LR algorithms for the WM-only and GM&WM datasets were similar in magnitude. In contrast, the KNN algorithm used for the GM-only set showed better scores in all the metrics, particularly in precision and F1 score.

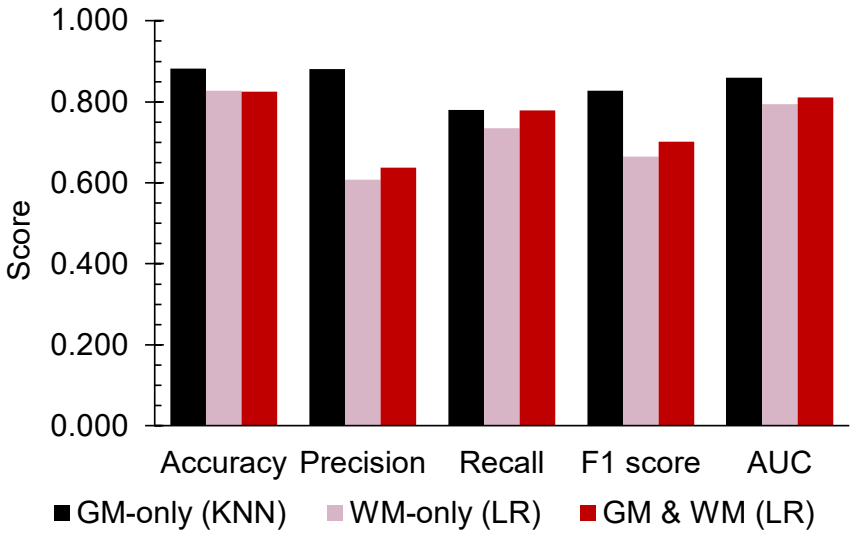

Figure 3-2. Metrics scores of the best performing algorithms for each dataset after CV and hyperparameter tuning, using the 30% test set.

3.3.2. Feature importance and range of values on injured elements

For the GM-only dataset with the KNN algorithm, the recursive analysis of feature importance showed that the top three mechanical features that provided the highest AUC score were minimum logarithmic strain (Min LEP), followed by the maximum logarithmic

strain (Max LEP) and Tresca stress (TRESCA). The AUC values scored by the KNN algorithm with each individual mechanical feature are displayed in Table 3-5.

Table 3-5. Results from the feature importance analysis on the GM-only dataset and KNN classifier using the AUC score. A heat map of feature importance is included (darker color – higher importance).

Dataset	Criteria	Mechanical Feature				
		Min LEP	Max LEP	LEAXON	TRESCA	ESEDEN
GM	AUC value	0.82	0.81	0.72	0.81	0.79

The range of mechanical values for the all the GM-only samples that were correctly classified by the KNN algorithm as injured or healthy are summarized in Table 3-6. 'Threshold' values observed between injured and healthy elements were also included.

Table 3-6. Maximum, mean, minimum, and SD values of the GM-only samples correctly predicted with an injury probability >50% (injured - red) and <50% (healthy – white).

Mechanical feature	Injury probability	Sample class	Min	Mean	Max	SD	Threshold
Min LEP	>50%	Injured	-0.36	-0.62	-0.95	0.12	-0.53
	<50%	Healthy	-0.11	-0.30	-0.53	0.09	
Max LEP	>50%	Injured	0.26	0.35	0.48	0.05	0.34
	<50%	Healthy	0.11	0.21	0.34	0.05	
LEAXON	>50%	Injured	0.10	0.26	0.44	0.08	0.32
	<50%	Healthy	0.00	0.10	0.32	0.07	
TRESCA	>50%	Injured	0.13	0.42	1.95	0.24	0.30
	<50%	Healthy	0.03	0.09	0.30	0.06	
ESEDEN	>50%	Injured	0.01	0.07	0.43	0.05	0.14
	<50%	Healthy	0.00	0.02	0.14	0.02	

The data in Table 3-6 show that the spread of mechanical values in injured GM tissue sections always showed larger maximum magnitudes than the spread of feature values in the healthy areas. The largest differences between maximum magnitudes in healthy and injured GM elements were observed for the TRESCA and ESEDEN features,

with 147% and 102% of percentage difference, respectively. Consequently, most mechanical magnitudes found on healthy samples of the GM-only set overlapped with the range of values reported for the injured ones. These ranges were more overlapped for the ESEDEN and LEAXON features, since approximately 93 and 69% of the values were shared. An overlap of only 35% of the Max LEP values was identified between the healthy and injured samples. The standard deviation on GM injured elements indicated a larger spread of magnitudes than in the healthy samples for all mechanical features, particularly for the TRESCA and ESEDEN.

For the WM-only dataset, the best classifier algorithm was LR. By requesting the coefficients of importance calculated by the ML algorithm, the logarithmic strain in the axonal direction (LEAXON) was found to have the largest effect on increasing the probabilities of a sample to be classified as injured, followed by the Tresca stress and Min LEP (Table 3-7).

Table 3-7. Results from the feature importance analysis on the WM-only dataset and LR classifier using the feature's coefficients. A heat map of feature importance is included (darker color – higher importance).

Dataset	Criteria	Mechanical Feature				
		Min LEP	Max LEP	LEAXON	TRESCA	ESEDEN
WM	Coefficient of importance	3.74	-1.29	7.47	5.24	3.12

The thresholds and ranges of mechanical values for the injured and healthy samples correctly classified in the WM-only set are displayed in Table 3-8. Like the GM, the injured WM samples also showed larger maximum magnitudes than the healthy elements. The largest percentage differences between maximum values in healthy and injured samples were 147.7% and 92.4%, for the TRESCA and ESEDEN features, in that order. There was also a significant overlap between the range of LEAXON and ESEDEN values, since 100 and 96.9% of these features' magnitudes in healthy WM elements were also found on injured samples (Table 3-8). The standard deviation on mechanical values associated with injured samples was also larger than deviation on healthy samples, specially for the TRESCA and ESEDEN.

Table 3-8. Maximum, mean, minimum, and SD values of the WM-only samples correctly predicted with an injury probability >50% (injured - red) and <50% (healthy – white).

Mechanical feature	Injury probability	Sample class	Min	Mean	Max	SD	Threshold
Min LEP	>50%	Injured	-0.28	-0.69	-1.20	0.19	-0.77
	<50%	Healthy	-0.05	-0.32	-0.77	0.12	
Max LEP	>50%	Injured	0.12	0.41	0.76	0.11	0.68
	<50%	Healthy	0.04	0.27	0.68	0.09	
LEAXON	>50%	Injured	0.00	0.28	0.45	0.07	0.26
	<50%	Healthy	0.00	0.06	0.26	0.06	
TRESCA	>50%	Injured	0.02	0.18	0.93	0.13	0.14
	<50%	Healthy	0.00	0.02	0.14	0.02	
ESEDEN	>50%	Injured	0.01	0.07	0.87	0.09	0.32
	<50%	Healthy	0.00	0.01	0.32	0.02	

Different threshold values were observed for each spinal cord tissue. GM's LEAXON and TRESCA thresholds were found after larger magnitudes than the WM ones. However, the roles inverted when looking at the Min/Max LEP and ESEDEN WM thresholds, whose values were larger than the proposed values for the GM. The most significant differences between the threshold values of the two tissues were found in the ESEDEN and TRESCA features (78.3 and 72.7%, respectively), while the closest thresholds were the LEAXON and Min LEP ones (20.7 and 36.9%).

3.4. Discussion

Mechanical data from FE models in combination with histopathology results from SCI experiments have shown the correlation between injury mechanics and tissue damage [9], [17], [18], [54], [126], [130], [131]. Still, it has not been possible to quantify this relationship, or to identify clear mechanical threshold values after which the spinal cord tissue will be damaged. As such, in this study it was proposed to explore the capabilities of different ML algorithms to classify injured elements in computational models of SCI, based on the mechanical outputs of the injury simulations. It was expected that including different classifiers, which follow different approaches to find patterns in the data,

would leverage some of the challenges encountered when studying the effect of mechanics on tissue damage.

Our results show that the ML algorithms have different classification capabilities for identifying injured elements based on the input data coming from FE models and histopathology. Each algorithm assigned distinct levels of importance to the mechanical features in the tissue datasets, which affected the minimum magnitudes at which each algorithm classified a sample as injured. Based on those observations, evaluating the performance of other ML classifiers that would use different criteria to analyze the input data could further validate the classification results, and the observed patterns between the mechanical feature magnitudes and the probability of an element to be injured. At the same time, it would be ideal to increase the number of available samples, since currently the data available belonged to only three primate subjects. Having data from more animal subjects would help to confirm our findings are not only representative of the observed cases and would strengthen the conclusions discussed in this document. These improvements in the proposed methodology could contribute to enhance the relevance of FE models as a clinical tool for the prediction of injury patters on animal experiments.

3.4.1. Parameter tuning and cross-validation

The AUC scores achieved by the evaluated ML algorithms differed depending on the evaluated dataset, still the values fell within the narrow range of 0.79 and 0.83. These results agree with other biomedical binary classification studies [100], [132], where the performance of ML algorithms was linked to the ability to find patterns in the data [100]. In this study, differences in sample sizes and distribution of classes could further affect the algorithms' sensitivity. For instance, the WM-only set had more than three times the number of samples than the GM-only one (Table 3-1). At the same time, this smaller sample size increased the percentage of injured elements in this set. Around 36% of the GM-only dataset were injured elements, in contrast with the 23% and the 26% included in the WM-only and GM&WM datasets, respectively. The similar proportion of injured elements between the WM-only and the GM&WM sets might explain the similarities in the metrics scores calculated by their LR classifiers; it also suggests that evaluating for tissue damage simultaneously for the gray and white matter does not facilitate the classification task.

The variance in number of injured elements per data set was related to the structural differences in the GM and WM tissues and the distribution of tissues across the spinal cord. The differences in material properties for GM and WM have been found to affect their mechanical response during injury, and therefore the distribution of damage [9], [55]. GM is a homogeneous and blood vessel-dense tissue [9], while WM shows anisotropic behavior due to the highly aligned set of axonal fibers [18]. Particularly in the WM it has been difficult to correlate mechanical parameters with tissue damage. Axonal fibers located in the WM are distributed with different densities throughout the tissue and can exhibit different calibre (diameters) depending on their location [34]. Future work on improving the material models implemented in FE models of SCI could investigate better capturing the variable characteristics of the axonal fibers in different sections of the WM tissue to gain a better insight at the distribution of stresses and strains. These observations highlight the classification challenges of the data and justify the interest in exploring the use of ML to better identify injured sections in the spinal cord tissues.

The unbalanced distribution of injured and healthy elements was one of the reasons the AUC score was selected as the comparison metric. In other ML applications the accuracy score determines the classification potential of an algorithm [132], however, in this study, the skewed class distribution limited this metric's relevance. Based on the findings of [133], [134], using other available metrics such as precision and recall, could result in prioritizing the classification of only one of the available classes. Consequently, the AUC score was selected as the metric to evaluate, since the results found in [132], [135] also showed it is robust for both balanced and unbalanced datasets, even those with a greater imbalance compared with these data.

The differences between the algorithms' performance on each tissue dataset were more evident when looking at several metrics. As shown in Figure 3-2, the accuracy, recall, and AUC scores were similar between datasets. However, precision and F1 scores were significantly lower in the WM-only and GM&WM datasets compared to the GM-only set, indicating there is a greater number of false-positive (healthy samples classified as injured) cases in the classification. These results might be related to the smaller number of injured samples available in the sets for the ML algorithms to learn from and the differences in correlation between mechanical features and the damage in GM or WM tissue found in [8], [9], [18]. Although is important to mention that one of the reasons why the WM tissue damage has shown a weaker correlation to mechanical parameters than

the GM, could be due to the anisotropy of the material resulting from the uneven distribution of axonal fibers and the different diameters they can exhibit, that to the author's knowledge, has not been captured in the WM definition of FE models of SCI. Another factor that should be consider is the that the histology used to characterize tissue damage was obtained around 20 weeks after the mechanical impact to the spinal cord [47]. This means that the resulting damage is a combination of the mechanical loading effect during the primary injury phase and the biological responses that follow during the secondary injury, which limits the ability of the algorithms to predict tissue level injury from mechanics alone.

When a similar methodology was followed using an FE model of rat SCI [9], experimental tissue damage data, and linear regression to correlate damage to maximum principal strain values, they reported AUC scores of 0.97 and 0.88 for the GM and WM, respectively. In this study, lower AUC scores were achieved, ranging between 0.82-0.83 for the GM-only dataset, 0.79-0.81 for the WM-only, and 0.8-0.81 for the combined GM&WM set. However, the higher AUC scores reported in [9] are most likely related to the larger injury generated in the animal subjects, since they were subjected to a bilateral injury, the shorter time between the injuries and the histology collection [136], and the analysis of one mechanical parameter. In [18], Jannesar and colleagues used LR to investigate the correlation between mechanical outcomes of FE models of non-human primate SCI and tissue damage on a larger version of the same data used for this study. The mean AUC values acquired in [18] ranged between 0.85-0.95 for the GM and 0.72-0.9 for the WM matter; which were also higher AUC scores than the acquired ones in this work.

The variance in AUC results with respect to Jannesar et al. [18] observations can also be explained by the differences between implemented approaches on each study. The AUC scores reported by Jannesar and coworkers were generated after analyzing the data one mechanical feature at a time, while in this study, the training and testing of the LR algorithm included the values of the five relevant features. The features were not studied individually since other researchers support that tissue damage after SCI might be the result of a combination of stresses and strains, rather than by the individual effects of one of these parameters [126]. Additionally, in this study collinear features and outlier experimental data were removed from the input samples. In [18], the data of an FE model corresponding to a NHP subject whose experiment deviated from the expected outcomes

due to an undiagnosed medical condition was included. The results from this experiment and FE model were significantly different than the ones found in other subjects, therefore those samples were excluded from the input data used in this study. Moreover, during the data pre-processing of the datasets, the Von Mises and Tresca features had a Pearson correlation coefficient of 1, indicating collinearity between the variables. In the context of ML, collinearity indicates that two or more features are closely correlated to each other, and they provide similar or redundant information regarding the prediction or classification task [137]. Researchers try to avoid the use of highly collinear features in ML applications since they increase the dimensionality of the problem without providing relevant information, thus reducing the model's performance and efficiency [137], [138]. Consequently, the datasets used in this study only included the TRESCA feature data. This choice was taken both to avoid the collinearity issue between the Tresca and Von Mises stress features, and the limitations of the Von Mises criterion to properly calculate stress values in non-linear and non-isotropic materials [123], such as the ones used to represent the GM and WM in the spinal cord of our FE models. Lastly, on [18], random sets with equal number of injured and healthy samples were used to fit the statistical model, while in this study the proportion of samples was kept the same. To account for the unbalanced datasets the "class weight" was included as part of the ML algorithms. These changes were proposed to improve the quality of the data and mitigate sources of variability, which can allow us to draw more reliable conclusions regarding the relationship between mechanical loading and tissue damage during SCI.

3.4.2. Feature importance and range of values on injured elements

The best performing algorithms for each spinal cord tissue dataset also provided different results regarding the mechanical features' importance for identifying damage. For the GM-only elements classified with the KNN algorithm, the Min LEP followed by Max LEP and TRESCA were the best injury predictors based on the AUC scores obtained when classifying samples using each individual feature (Table 3-5). The differences between AUC scores ranged between 1 and 13%, which indicates similar contributions of the mechanical parameter to the injury identification in this dataset. These findings are similar to the reported ones on Jannesar et al. [18], where using the Nagelkerke R^2 to measurement the injury-predicting capabilities of each feature, reported that TRESCA,

MaxLEP, and MinLEP were the most relevant features for the GM, with a percentage difference in their R^2 value no larger than 24%.

Meanwhile, LEAXON, TRESCA, and Min LEP showed the highest coefficients of importance for the LR classifier used with the WM-only dataset (Table 3-7). Percentage differences between the features' coefficients of importance ranged from 18 to 283%. This suggests that the most relevant mechanical features had larger contributions in the classification of injured samples for the WM dataset evaluated with the LR algorithm and highlights the importance of carefully selecting the features included on the datasets. In [18], the same mechanical features showed the highest relevance for tissue identification however the order was: TRESCA, Min LEP, and LEAXON, and the largest difference between the R^2 values of each parameter was approximately 48%. The observed variance in the order of feature importance's rankings between Jannesar findings and our results could be related to the differences in the included data, included features, and the fitting process for the algorithms previously explained. Still, other studies such as the one performed by Czyz et al. [113], agree with the results from the WM-only set, where the LEAXON feature showed the highest coefficient of importance for identification of tissue damage. They evaluated the predictive roles of stress and strain values in the horizontal (X), sagittal (Y), and longitudinal (Z) axis of the spinal cord of FE models reconstructed from human SCI cases. Using a multiple logistic regression model, they found that stress and strains in the longitudinal or axonal direction were more significant indicators of neurological damage than the values in other directions.

The observed differences in threshold values of the most relevant features, presented in Table 3-6 and Table 3-8, provided information regarding the susceptibility of each spinal cord tissue to damage after impact. GM-only samples with an injury probability >50% showed to be more susceptible to Min/Max LEP magnitudes than the WM samples. Inversely, WM samples results indicated they are more susceptible to TRESCA stress and LEAXON strains than the GM. These could be key observations to account for during the interpretation of mechanical outcomes from FE models recreating animal SCI experiments. Particularly since depending on the impact parameters and morphological dimensions of the animal subjects, both the distribution and magnitude of stresses and strains will vary [17], [18], [55], [122]. Accounting for the susceptibility of each spinal cord tissue to different mechanical parameters could provide insights to better control the spread of damage in the experiments, by carefully tunning the levels of spinal cord

compression or applied force, which could improve the consistency of injury outcomes between subjects.

Comparing the proposed thresholds against the ones in [18], the magnitudes of their values differ with the findings of this work by at least 32%. Yet, their results show similar trends to the ones found in this study regarding the susceptibility of each spinal cord tissue to the mechanical features. As such, Jannesar et al.'s GM results indicated it was less susceptible to Tresca stress than the WM, and the opposite behavior was observed for when comparing the Min/Max LEP thresholds. The differences in the proposed threshold magnitude can be explained by the fact that Jannesar et al. used the samples right at the 50% probability mark, while in this work, both the correctly classified healthy and injured samples were studied and the 'thresholds' were defined after finding a value that was not shared between the healthy and injured elements. This approach was followed to have a closer look at the range of mechanical values that the ML algorithms related only to tissue damage, since based on the findings of Russel et al. [8], it was possible to find ranges where even small magnitudes of stress or strain were also related to injury. Additionally, according to the author's understanding of the ML algorithms, the samples classified as injured with probabilities close to the 50% boundary represent samples that the algorithm was less certain about during the classification. As such, defining thresholds from those samples might not be optimal, since it is likely that the algorithms were not able to draw strong conclusions about the correlation of mechanical features and tissue damage. It is also suggested that future stages of this work consider these facts when using the inverse prediction method to define thresholds, since it was shown in this study that even considering the correctly classified injured GM and WM samples with more than 50% of injury probability, there are wide ranges of values for the different mechanical features that can even be found on the healthy samples (Table 3-6 and Table 3-8).

The findings of other researchers regarding possible mechanical thresholds were also compared against our results. As it was previously mentioned, Russell and colleagues [8] reported that maximum principal strains in the cervical spinal cord of rats above 0.1 were correlated to tissue damage after a contusion injury. Czyz et al. [113] work with reconstructed FE models from human cervical SCI cases described values of 0.0081 MPa stress and 0.01 strain in the longitudinal or axonal direction as the cut off magnitudes for neurological deficit risk in the spinal cord. In other studies, such as the one of Fradet

et al. [130] performed in harvested porcine spinal cords, they detected mechanical damage to the cervical spinal cord tissue after engineering strains of 0.74 – approximately equivalent to a logarithmic strain of 0.55 - using similar compression rates to the ones followed in the NHP experiments studied in this paper. The threshold values proposed in [8] and [131] were considerably lower in magnitude than the thresholds suggested in the current paper, similar to the observations in Jannesar et al. [18]. The proposed strain magnitude indicating mechanical damage by Fradet and colleagues [130] was closer to the Max LEP thresholds proposed for the GM and WM samples in this study. Still, it is worth noting that they did not look at histopathological evidence to identify tissue damage, instead they defined their threshold at the point of material failure they observed during the compression of the porcine spinal cord samples.

Although we were able to isolate and propose individual mechanical threshold values for the GM and WM, it is important to consider that tissue damage can be correlated to the combined effects of both stresses and strains [114], as opposed to the individual effect of a specific mechanical parameter. This idea was proposed in the earlier work of Galle et al. [114], where they studied the correlation between stress and strain values at the tissue level in WM samples of guinea pig spinal cord using single and multiple regression analyses. Their analyses indicated that the strongest correlation between tissue damage in the WM was linked with a combination of normal (σ_x, σ_y, and σ_z) and shear (τ_{xy}) stresses, and a combination of in-plane strains (ε_x, ε_y, and ε_{xy}). Even though Galle and coworkers' conclusions resulted from the observation exclusively in the WM, it its possible that this behavior could extend to the GM, involving a different combination of mechanical parameters. This observation could also highlight one of the main advantages of using the methodology proposed in this study for the classification of injured elements in FE models of SCI. The selected ML algorithms were trained with the data from multiple mechanical features, and they use it simultaneously to construct a multidimensional decision boundary that allowed for the classification of the injured elements. Their classification process accounts for the collective effect of the including mechanical features, following the idea proposed by Galle et al. Future stages of this work could concentrate on recovering the multi-variable thresholds defined by these algorithms, and studying their correlation with spinal cord tissue damage.

The implementation of ML algorithms showed promise at classifying and analyzing the range of mechanical values of injured and healthy samples of the spinal cord based

on FE modeling and histopathological data. The classification capabilities measured with the AUC scores fell within the scores reported in previous studies [9], [18]. Additionally, looking at the range of mechanical values of the correctly classified healthy and injured elements of the FE models, it was possible to identify ranges of values for each mechanical feature that corresponded exclusively to the injured elements. Something that was not observed in previous studies, since the range of values of the healthy elements were not studied [9], [18], or they overlapped with the magnitudes observed on the injured elements not allowing to identify a specific separation [8]. While it will be needed to work on some of the limitations to make stronger conclusions on these findings, such as accessing earlier to the histopathology data to isolate the effect of mechanics on the tissue damage, or looking at the combined effect of stresses and strains to define multi-variable thresholds, these preliminary results should justify the further exploration of using ML algorithms as a tool to study the correlation between injury mechanics and the damage to the spinal cord tissue.

3.5. Conclusion

This study explored the use of supervised ML algorithms to establish relationships between mechanical features and tissue damage in SCI using histological data from animal experiments and FE outcomes. Classification performance of the ML algorithms varied for GM, WM, and combined (GM & WM) datasets as the distribution of samples, relevant features, and target values varied across the tissue datasets. The best performing classifier for the GM-only dataset was the KNN algorithm, while LR worked better for both the WM-only and GM&WM datasets. This suggests that using different classifiers to explore the correlation between the mechanical outputs and tissue damage in the gray and white matters could be beneficial to leverage some of the differences in the tissue responses during injury. Minimum/maximum logarithmic strain (Min/Max LEP) and Tresca stress (TRESCA) were the most relevant features for identifying injury in the GM. For the WM, strain in the axonal direction (LEAXON), followed by the Tresca and minimum logarithmic strain showed the highest coefficients of importance. Mechanical values that corresponded only to the correctly classified injured samples and could be considered as approximate thresholds to identify tissue damage based on the outcomes of FE models of SCI. These results also suggested that the GM exhibited a larger tolerance to Tresca stress and to strains in the axonal direction than the WM. The opposite was found for the

injured WM samples, which were classified after larger magnitudes of minimum/maximum logarithmic strain, and strain energy density (ESEDEN) than the injured GM samples. Leveraging ML to quantify the relationship between mechanical loading and tissue damage will improve the reliability of computational models, and open new avenues for the implementation of ML algorithms to identify SCI damage.

Chapter 4.

Discussion and Conclusion

4.1. Discussion

SCI is closely related to mechanical loading [3], [4], [6]. As such, understanding how the impact mechanics result in neurological damage in the spinal cord is a key step towards the development of prevention technologies, or potential treatments that will allow patients to recover motor and sensory function [3], [4]. Computational models of SCI based on experimental procedures in animals can help in this matter, since they provide a closer look at the tissue-level distribution of different mechanical parameters in the spinal cord [8], [9], [17], [18]. Still, the clinical usage of FE models of SCI is limited since the provided mechanical data that is yet to be translated or linked to experimental or functional outcomes so it can be used in a clinical SCI setting [4], [5], [18]. Attempts have been made to link these two areas (computational and clinical SCI methodologies) using FE mechanical outcomes in combination with tissue damage data acquired through imaging scans or histological procedures post injury, and statistical methods to investigate correlation between variables [8], [9], [18]. These attempts have helped understand the correlation of deformations and stresses to the tissue damage in the spinal cord that affects the neurological functions. Regardless, these methodologies are yet to be improved and streamlined so they can be used more efficiently as part of the SCI workflow.

Motivated by this, the studies in this thesis aimed to improve the reliability and clinical relevance of computational models to study the effects of impact mechanics in SCI. To achieve this, the effect of different CSF boundary conditions and spinal cord morphology in the mechanical outcomes of FE models of SCI were compared (Chapter 2). It was expected that this study could provide relevant data for guiding FE modeling choices, enhancing the accuracy and biofidelity of the computational models, while also considering computational efficiency. Subsequently, it was proposed to use ML algorithms to link FE mechanical outcomes and tissue damage data (Chapter 3), which could contribute to stronger conclusions regarding the correlation between mechanical loading and SCI. It was hypothesized that this methodology could help quantify specific limits or

tolerances of the spinal cord tissue for mechanical loading, which would be a useful contribution for SCI prevention.

The findings of these thesis chapters proposed interesting implications for the use of both FE models and ML algorithms to study SCI. For instance, Chapter 2 underscored the relevance of properly defining CSF boundary conditions in computational models of SCI to better capture the injury experiments, and accounting for the spinal cord morphology to define impact parameters that provide consistent outcomes. These insights highlighted important considerations for improving the accuracy of FE models and provided additional information to improve the experimental procedures in animals. These findings can be linked to the work in Chapter 3. In that chapter, it was mentioned that some of the challenges encountered by the ML algorithms during the classification of injured elements in the GM and WM dataset could be linked to the input data acquired from the computational models. Based on the observations reported in Chapter 2, this is a reasonable hypothesis, given that previous computational models of SCI have implemented some of the evaluated CSF boundary conditions without having completely validated their effect on the mechanical outcomes. For instance, effects of morphology and CSF boundary conditions, such as the changes in the magnitudes and location of the stresses and strains, could have affected the comparison between histological images and the FE element slices used to build the tissue datasets. While it is true there are other sources of variability in the generated tissue datasets other than the calculated mechanical values, such as the time delay between the injury and the histological data collection, improving the accuracy of FE models of SCI is a good step towards more reliable data that can be used for studies like the one proposed in Chapter 3.

Conversely, the findings from Chapter 3 regarding the mechanical features' importance for injury identification provide useful information for guiding the selection of requested mechanical features in the simulations of FE studies, like the one in Chapter 2. Moreover, the proposed threshold values for injured samples in Chapter 3 could be used as preliminary benchmarks to translate the FE results into approximations of injury outcomes. For example, Tresca stress figured among the top three most relevant features for injury identification for both the GM and WM (Chapter 3), with their respective injury thresholds of 0.30 and 0.14 MPa. Figure 2-11, Figure 2-12, and Figure 2-13 in section 2.3.3 show the Tresca stress magnitudes and locations in the spinal cord cross-sections of the simulated FE models. In all these figures, the Tresca stress color plots started at

the 0.25 MPa mark, meaning that every bright colored element located in sections of the WM could be considered potentially injured based on the 0.14 MPa threshold. The same analysis could be performed for the Tresca values located in the GM horns, where the elements with values above 0.3 MPa could also be considered as injured. This comparison can be implemented for every relevant mechanical parameter, and by identifying the location of the mechanical values above the thresholds with respect to the spinal cord regions, researchers could speculate about the functional outcomes that might be affected after the simulated injury. The preview of the possible injury distribution and neurological outcomes could inform researchers and clinicians on whether the followed injury protocol will generate suitable injury outcomes for the purpose of the study. This can contribute to further leverage the executed experiments on animals, and to this thesis objective of improving the reliability of FE models as a complementary tool for SCI research.

Using the trained ML models and FE outcomes could provide an approximation of the injury distribution after an SCI experiment. Motivated by the results of chapter 2 showing that the same impact parameters resulted in different general, and tissue-level mechanical outcomes, FE models could be used to define subject-specific impact parameters to improve the consistency of the injury outcomes. Systematically exploring subject-specific impact parameters in a large animal experimental model is not ethical or feasible. Leveraging the non-invasive nature of FE models of SCI to evaluate different combinations of impact parameters for a specific subject and predict mechanical tissue loading. The mechanical outcomes of the simulations could be later analyzed using the tissue damage thresholds defined with the ML algorithms in Chapter 3, and the potential injuries could be compared to determine the best combination of impact parameters for each subject.

Furthermore, the assessment of the location of above-threshold values in the spinal cord of the FE models could be automated by including the ML methodology introduced in Chapter 3. The ML algorithms from Chapter 3 have already been trained on both mechanical FE predictions and histological results and could be used to classify the data samples from other FE models. These models would account simultaneously for the evaluated mechanical features, which can improve the injury identification, since tissue damage in the spinal cord after SCI is likely the product of the combined effect of stresses and strains [114]. After classification, it would be possible to modify the Python scripts to provide the IDs of every element classified as injured and used them to create a display

group in ABAQUS of the injured elements. From there it would be possible to provide a three-dimensional view of the injury and its volume, helping to have a better idea of the distribution of the damage further away from the injury epicenter. This approximation of the injury could be further validated against ultrasound observations of the injury, that can be now taken within minutes after the impact and can further separate mechanical effects on tissue from biological responses to injury. By performing this comparison, it would be possible to assess the accuracy of the injury classification capabilities of the ML algorithms and identify possible areas of improvement.

Even though implementing the previously described methodology could make the FE models more versatile tools for SCI research, there are still limitations to overcome before this can be done. One of the biggest limitations is the long computational times required to run computational models of SCI. In Chapter 2 it was shown that depending on the morphology and CSF boundary conditions of the FE models, the computational times could vary between 48 and 127 hours. This is in large part attributed to the inability to conduct parallel computations on SPH elements. Although the SCI experiments are scheduled beforehand, which would provide with time to prepare a computational model in case it was needed, for unexpected situations the current FE models would not be able to provide a quick preview of the results. Consequently, finding ways to make the SCI simulations more efficient while maintaining the accuracy and level of detail in the results is one of the priorities for researchers working in this area [18]. Nonetheless, balancing the trade-off between computational efficiency and depth of the provided results can be complicated. For instance, there are faster computational models of SCI that have simplified the material properties of the spinal cord and other meninges [9], [17], [19], [55] or have not included them in the simulations [52], [68]. Despite these simplifications, those models have been able to predict values such as reaction force or impactor/pellet displacement within experimental observations. However, for some of the suggested approaches, such as the one in Chapter 3, a more accurate estimation of the tissue-level stresses and strains in the spinal cord is needed, and that could be hard to acquire in more simplified models.

In the context of our research and the described FE models, the trade-off is currently more inclined towards providing detailed results rather than computational efficiency, and it is partially related to the implementation of SPH for representing the CSF. Despite the efficiency and accuracy described in other studies of traumatic brain injury

and SCI [8], [16], [22], [23], the SPH computations in ABAQUS are performed in a single processor, since the method has some limitations in the use of multiple processors depending on the characteristics of the analysis [21]. As a result, despite having access to the computational resources, it was not possible to breakdown the SCI simulations into multiple domains (multiple processors), which would help to reduce the computational time of the models. Although our results suggest that different combinations of spinal cord and column morphologies and CSF boundary conditions provide better computational times, it would be important to look for more efficient alternatives of the implemented FE techniques in the computational models of SCI. This idea is not limited to SPH, since other areas of our models such as the preload step could be further improved to make the simulations more computationally efficient. Successfully reducing the computational times of FE models of SCI may be particularly important for both enabling a faster analysis of more complex SCI models, like the more detailed subject-specific models, and allowing for the implementation of the combined workflow of FE models and ML algorithms for injury estimation.

4.2. Contribution and relevant findings

As described in section 1.7, the general goal of the work presented in this document was to contribute to advancing the reliability and clinical relevance of computational models of SCI, by evaluating the CSF representation with SPH under different boundary conditions in a contusion FE model with preload, and the integration of supervised ML techniques for tissue damage identification. These specific contributions are listed next, starting with the findings from the methods described in Chapter 2:

1. The choice of CSF boundary conditions in a computational model of cervical SCI with preload based on NHP experiments has a great influence in the predicted impactor displacement, preload reaction forces, and computational times. Most importantly it affected the magnitude of the stresses and strains calculated in the spinal cord cross-section at the epicenter of the injury.

2. Spinal cord and spinal column morphologies showed a considerable effect in the impact force outcomes and the stress and strain distribution at the injury epicenter. The results showed that for the same impact parameters, increasing

the morphological dimensions shifted the location of higher stresses and strains in the spinal cord dorsolaterally.

3. The closed boundary (CB) approach, which is a common boundary condition employed for the CSF in FE models of SCI, can overestimate the CSF pressure in small and average morphologies. These deviations in the CSF pressure can affect the stress and strain values calculated in the spinal cord, and as such, it would be suggested to implement another CSF containment approach for these morphological cases.

Moving on to Chapter 3, the relevant findings were:

1. Using mechanical data from FE models of SCI and histological results to train them, the supervised ML algorithms k-nearest neighbors and logistic regression showed to be better classifiers than decision trees and support vector machines for injured elements in the GM, WM, and combined tissues datasets.

2. Classifying injured samples simultaneously in the gray and white matter elements showed to have limited improvements in the classification outcomes. As such, it is recommended that each spinal cord tissue is evaluated individually, as their mechanical response will be related to their specific material characteristics and distribution of injured/healthy samples.

3. The feature importance analysis depicted that for the GM dataset classified with the KNN algorithm, the top three relevant features were minimum principal strain, maximum principal strain, and Tresca stress. For the WM set classified with LR, the strain in the axonal direction, Tresca stress, and minimum principal strain were the three most relevant features for injury identification.

4. Looking at the injury probabilities predicted by the ML algorithms on the classified samples, it was possible to identify mechanical ‘threshold’ values corresponding only to correctly classified injured elements. The calculated thresholds indicated that the GM is more susceptible to minimum and maximum principal strain magnitudes than the WM samples. Meanwhile, it was

observed that the WM was more susceptible to the strains in the axonal direction and the Tresca stress than the GM.

4.3. Future research questions

The work presented in this thesis contributed to the initial objective of refining computational models of SCI for improving their reliability and expanding their applications. However, the work also motivated many new questions and areas that warrant further exploration. While the scope of the thesis was constrained to be achievable as a master's thesis, the results highlight opportunities for ongoing research to deepen our understanding of SCI biomechanics and the implementation of both FE models and ML algorithms for its study. Consequently, in the following section opportunities for future investigation that could continue to expand our understanding of SCI and lead to better interventions and treatments for these medical conditions will be discussed.

Starting with Chapter 2, the observed variability in the mechanical outcomes of the evaluated FE models during the preload constitutes a subject for future investigation. The preload is a fundamental part of the SCI simulations, as it influences the impactor's preload displacement, which is also linked to the initial spinal cord compression and the total impactor's displacement. The preload step accounts for at least 50% of the simulations' computational time. Making sure the preload's performance is consistent and efficient in both computational and experimental models of SCI could be critical to have better mechanical and injury outcomes. The current preload step is force-controlled, which explains its sensitivity to the different CSF boundary conditions and morphologies of the models. Still, it was consistently observed that the predicted impactor's displacements were below the experimental mean in our models. Since our simulations shown that these variations in the preload displacement can have an effect in the impact force and stress and strain magnitudes, it proposed to follow the next research directions:

- Evaluate the difference between a force-controlled and a displacement-controlled preload phase. Implementing the preload as a displacement-controlled step could help to reduce the sensitivity of this approach and improve the mechanical outcomes such as impactor's preload displacement, and the trapping of the spinal cord at the bottom of the subarachnoid space. The comparison between the force-controlled and displacement-controlled

preloading could be implemented computationally, and the results could provide interesting insights, possibly transferable to the experimental procedures. This could be particularly relevant since the preload's variability is not exclusive of the FE models. The peak preload forces and displacements reported in the experiments also show certain degree of variability.

- Compare the computational efficiency and FE outcomes accuracy of the preload step when implemented with an implicit solver. The computational times required for the simulations are a persistent constraint for widening their used in the SCI research workflow. For this reason, making the simulations more efficient while maintaining their biofidelity would be a great contribution to this field of study. Given the low deformations of the different instances of the SCI models during the preload step, it could be possible to run this step using an implicit solver instead of an explicit one. Although the distribution of computational times was even between the preload and impact steps in most simulations, this change could contribute to reducing the overall computational time of the simulations.

The results from our FE models showed that using different CSF boundary conditions in our computational models it is possible to provide different ranges of CSF pressure values during impact. From previous computational and experimental models, we know the importance of properly capturing the CSF pressure, so it does not skew the mechanical FE outcomes, yet it captures its protective role during SCI [11], [15], [56]. Nonetheless, as shown in the work of Arhiptsov et al. [23], there are situations where SCI can be further influenced by medical conditions, such as intracranial hypertension, that increases the CSF pressure [120]. There are other conditions that show changes in the CSF pressure of the affected population, which also makes them more susceptible to SCI. This is the case of when the CSF volume is reduced as seen in older adults [119], and the effects of degenerative cervical myelopathy [121]. Consequently, the following research question is stated:

- Investigate the feasibility of some of the proposed CSF boundary conditions for effectively recreating SCI scenarios influenced by other medical conditions, such as intracranial hypertension, spine degeneration/CSF volume reduction in older adults, and degenerative cervical myelopathy. Implementing the CSF

boundary conditions could be a computationally efficient substitute to adding loading conditions in FE models of SCI for capturing the influence of other medical conditions in the CSF pressure, particularly when using SPH as the CSF's modelling approach.

Shifting gears into the work presented in Chapter 3, the implementation of ML for injury classification showed additional challenges when evaluating the WM samples. The difference between the precision and recall scores in the WM samples classification suggest that it was harder for the LR algorithm to properly label healthy elements than injured ones. One of the possible factors related to these differences in classification could be the spread of the injury far away from the epicenter. The histological analysis in [47] showed that the rostral-caudal spread of the tissue damage from the injury epicenter was not uniform. Additionally, it was observed that in spinal cord regions further away from the injury epicenter, most of the damage was in discontinuous areas of the WM. In the sections of the FE models corresponding to those areas, perhaps the mechanical values of injured elements are lower than in other regions and given the limited number of injured samples available for the ML classifier, these lower mechanical values affected the classification boundary for WM elements. As a result of these observations, a future research suggestion is:

- Modify the tissue datasets and the ML algorithms' implementation to account for the mechanical values of neighbouring elements and the distance from the injury epicenter. These changes could help differentiate between WM sections that showed low mechanical values in the FE models, but still presented damage either due to compromises in adjacent tissue structures (e.g., disruption of blood vessels and limited blood supply) or the non-uniform distribution of the injury in the rostral and caudal directions.

From the combined observations reported in Chapter 2 and 3, there are other research directions worth exploring. Studies such as the one of Fradet et al. [118], showed the change in the stress-strain curves in samples of porcine spinal cord after reaching the 'failure' value. This could imply that during the experiments, certain sections of the spinal cord reach these 'failure' values before the impact step finishes, which would effectively change their mechanical response during the rest of the experiment. In our current models, the behavior of the spinal cord will remain constant during the simulated process,

however, it is likely that more accurate results would be calculated if it were possible to capture failure modes of the materials. This methodology is already implemented in other computational studies studying mechanical structures in ABAQUS [139] and rupture in soft tissues [140], so it would be feasible to implement. Moreover, either available experimental data or threshold values, like the ones proposed in Chapter 3, could be useful for triggering the failure mode in the computational models. In summary, the research suggestion is:

- Upgrade the computational models of SCI to capture the damaged-based failure of the spinal cord tissues to improve the mechanical response and outcomes from the models.

4.4. Concluding remarks

In this thesis, we have aimed to enhance the reliability and clinical relevance of computational models of SCI through a comprehensive exploration of numerous factors influencing mechanical FE outcomes and the integration of ML techniques for tissue damage identification. Our work provided valuable insights into the intricate relationship between biomechanical parameters, spinal cord morphology, and computational methodologies, with implications for both model refinement and clinical applicability. For instance, the importance of accurately representing CSF boundary conditions in computational models of SCI was demonstrated. Our findings underscored the substantial influence of CSF containment approaches on the predicted mechanical outcomes, impact parameters (i.e., impactor displacement and reaction forces), and stress and strain magnitudes within the spinal cord. Moreover, we identified potential limitations of commonly used CSF boundary conditions, suggesting the need for alternative approaches, particularly for cases involving small or average morphologies. Furthermore, our exploration of spinal cord and spinal column morphologies elucidated their significant impact on injury outcomes, with variations in dimensions resulting in distinct stress and strain distributions. This highlights the importance of considering subject-specific anatomical characteristics in computational modeling efforts, as they profoundly influence injury mechanisms and severity.

The integration of supervised ML algorithms for tissue damage identification presented promising avenues for enhancing the clinical relevance of computational

models. Through training on mechanical data from FE models and histological results, ML algorithms exhibited the ability to classify injured elements within gray and white matter tissues. Moreover, the feature importance analysis and the proposed mechanical injury 'threshold' values provided valuable insights to further our understanding of spinal cord tissue vulnerability to mechanical loading. Distinct susceptibility patterns observed between gray and white matter tissues emphasize the necessity of individualized evaluation, considering their unique material characteristics and response to mechanical stimuli.

Despite these advancements, challenges remain particularly regarding computational efficiency and model validation. The prolonged computational times associated with detailed FE models necessitate the exploration of strategies for balancing computational efficiency with result accuracy. Additionally, ongoing efforts are required to link computational predictions against clinical observations, ensuring the fidelity and applicability of modeling approaches in real-world scenarios. In conclusion, this thesis contributes to the ongoing quest for improving the understanding and management of SCI through the refinement of computational modeling techniques and integration of advanced ML methodologies. By elucidating the complex interactions between mechanical factors, anatomical considerations, and tissue responses, we move closer to the development of personalized, clinically relevant tools for SCI research and treatment.

References

[1] J. Bennett, J. M Das, and P. D. Emmady, “Spinal Cord Injuries,” in *StatPearls*, Treasure Island (FL): StatPearls Publishing, 2022. Accessed: Mar. 29, 2022. [Online]. Available: http://www.ncbi.nlm.nih.gov/books/NBK560721/

[2] Praxis Spinal Cord Institute, “Rick Hansen Spinal Cord Injury Registry - A look at traumatic spinal cord injury in Canada in 2019.,” Praxis, Vancouver, BC, 2021. [Online]. Available: https://praxisinstitute.org/?smd_process_download=1&download_id=10420

[3] A. Alizadeh, S. M. Dyck, and S. Karimi-Abdolrezaee, “Traumatic Spinal Cord Injury: An Overview of Pathophysiology, Models and Acute Injury Mechanisms,” *Front. Neurol.*, vol. 10, p. 282, Mar. 2019, doi: 10.3389/fneur.2019.00282.

[4] S. Mattucci, J. Speidel, J. Liu, B. K. Kwon, W. Tetzlaff, and T. R. Oxland, “Basic biomechanics of spinal cord injury — How injuries happen in people and how animal models have informed our understanding,” *Clinical Biomechanics*, vol. 64, pp. 58–68, Apr. 2019, doi: 10.1016/j.clinbiomech.2018.03.020.

[5] C. F. Jones and E. C. Clarke, “Engineering approaches to understanding mechanisms of spinal column injury leading to spinal cord injury,” *Clinical Biomechanics*, vol. 64, pp. 69–81, Apr. 2019, doi: 10.1016/j.clinbiomech.2018.03.019.

[6] C. S. Ahuja *et al.*, “Traumatic spinal cord injury,” *Nat Rev Dis Primers*, vol. 3, no. 1, p. 17018, Apr. 2017, doi: 10.1038/nrdp.2017.18.

[7] N. A. Silva, N. Sousa, R. L. Reis, and A. J. Salgado, “From basics to clinical: A comprehensive review on spinal cord injury,” *Progress in Neurobiology*, vol. 114, pp. 25–57, Mar. 2014, doi: 10.1016/j.pneurobio.2013.11.002.

[8] C. M. Russell, A. M. Choo, W. Tetzlaff, T.-E. Chung, and T. R. Oxland, “Maximum Principal Strain Correlates with Spinal Cord Tissue Damage in Contusion and Dislocation Injuries in the Rat Cervical Spine,” *Journal of Neurotrauma*, vol. 29, no. 8, pp. 1574–1585, May 2012, doi: 10.1089/neu.2011.2225.

[9] J. T. Maikos, Z. Qian, D. Metaxas, and D. I. Shreiber, “Finite Element Analysis of Spinal Cord Injury in the Rat,” *Journal of Neurotrauma*, vol. 25, no. 7, pp. 795–816, Jul. 2008, doi: 10.1089/neu.2007.0423.

[10] S. Jannesar, B. Nadler, and C. J. Sparrey, “The Transverse Isotropy of Spinal Cord White Matter Under Dynamic Load,” *Journal of Biomechanical Engineering*, vol. 138, no. 9, p. 091004, Sep. 2016, doi: 10.1115/1.4034171.

[11] C. F. Jones, S. G. Kroeker, P. A. Cripton, and R. M. Hall, “The Effect of Cerebrospinal Fluid on the Biomechanics of Spinal Cord: An Ex Vivo Bovine Model Using Bovine and Physical Surrogate Spinal Cord,” *Spine*, vol. 33, no. 17, pp. E580–E588, Aug. 2008, doi: 10.1097/BRS.0b013e31817ecc57.

[12] C. F. Jones, “CEREBROSPINAL FLUID MECHANICS DURING AND AFTER EXPERIMENTAL SPINAL CORD INJURY”. University of British Columbia, 2011.

[13] C. F. Jones, J. H. T. Lee, U. Burstyn, E. B. Okon, B. K. Kwon, and P. A. Cripton, “Cerebrospinal Fluid Pressures Resulting From Experimental Traumatic Spinal Cord Injuries in a Pig Model,” *Journal of Biomechanical Engineering*, vol. 135, no. 10, p. 101005, Oct. 2013, doi: 10.1115/1.4025100.

[14] C. Persson, S. W. D. McLure, J. Summers, and R. M. Hall, “The effect of bone fragment size and cerebrospinal fluid on spinal cord deformation during trauma: an ex vivo study: Laboratory investigation,” *SPI*, vol. 10, no. 4, pp. 315–323, Apr. 2009, doi: 10.3171/2009.1.SPINE08286.

[15] C. Persson, J. Summers, and R. M. Hall, “The Importance of Fluid-Structure Interaction in Spinal Trauma Models,” *Journal of Neurotrauma*, vol. 28, no. 1, pp. 113–125, Jan. 2011, doi: 10.1089/neu.2010.1332.

[16] A. Rycman, S. McLachlin, and D. S. Cronin, “Comparison of numerical methods for cerebrospinal fluid representation and FLUID–STRUCTURE interaction during transverse impact of a finite element spinal cord model,” *Numer Methods Biomed Eng*, Jan. 2022, doi: 10.1002/cnm.3570.

[17] C. J. Sparrey, E. A. Salegio, W. Camisa, H. Tam, M. S. Beattie, and J. C. Bresnahan, “Mechanical Design and Analysis of a Unilateral Cervical Spinal Cord Contusion Injury Model in Non-Human Primates,” *Journal of Neurotrauma*, vol. 33, no. 12, pp. 1136–1149, Jun. 2016, doi: 10.1089/neu.2015.3974.

[18] S. Jannesar, E. A. Salegio, M. S. Beattie, J. C. Bresnahan, and C. J. Sparrey, “Correlating Tissue Mechanics and Spinal Cord Injury: Patient-Specific Finite Element Models of Unilateral Cervical Contusion Spinal Cord Injury in Non-Human Primates,” *Journal of Neurotrauma*, vol. 38, no. 6, pp. 698–717, Mar. 2021, doi: 10.1089/neu.2019.6840.

[19] N. Obaid *et al.*, “Effect of Impact Parameters on a Unilateral Contusion Model of Spinal Cord Injury in a Virtual Population of Non-Human Primates,” *Neurotrauma Reports*, vol. 4, no. 1, pp. 367–374, Jun. 2023, doi: 10.1089/neur.2023.0006.

[20] J. L. Lacome, “Smooth Particle Hydrodynamics (SPH): A New Feature in LS-DYNA”.

[21] “Smoothed particle hydrodynamics.” Accessed: Mar. 31, 2022. [Online]. Available: https://abaqus-docs.mit.edu/2017/English/SIMACAEANLRefMap/simaanl-c-sphanalysis.htm

[22] H. Duckworth, D. J. Sharp, and M. Ghajari, “Smoothed particle hydrodynamic modelling of the cerebrospinal fluid for brain biomechanics: Accuracy and stability,” *Int J Numer Meth Biomed Engng*, vol. 37, no. 4, Apr. 2021, doi: 10.1002/cnm.3440.

[23] K. Arhiptsov and G. Marom, “Numerical Models of Spinal Cord Trauma: The Effect of Cerebrospinal Fluid Pressure and Epidural Fat on the Results,” *Journal of Neurotrauma*, vol. 38, no. 15, pp. 2176–2185, Aug. 2021, doi: 10.1089/neu.2021.0065.

[24] “Spinal Cord: Function, Anatomy and Structure,” Cleveland Clinic. Accessed: Jul. 03, 2023. [Online]. Available: https://my.clevelandclinic.org/health/body/21946-spinal-cord

[25] “Spine Anatomy, Anatomy of the Human Spine.” Accessed: Jul. 03, 2023. [Online]. Available: https://mayfieldclinic.com/pe-AnatSpine.htm

[26] Y. S. Khan and F. Lui, “Neuroanatomy, Spinal Cord,” in *StatPearls*, Treasure Island (FL): StatPearls Publishing, 2023. Accessed: Jul. 03, 2023. [Online]. Available: http://www.ncbi.nlm.nih.gov/books/NBK559056/

[27] L. Thau, V. Reddy, and P. Singh, “Anatomy, Central Nervous System,” in *StatPearls*, Treasure Island (FL): StatPearls Publishing, 2023. Accessed: Jul. 03, 2023. [Online]. Available: http://www.ncbi.nlm.nih.gov/books/NBK542179/

[28] “A Neurosurgeon’s Overview of the Anatomy of the Spine and Peripheral Nervous System.” Accessed: Jul. 03, 2023. [Online]. Available: https://www.aans.org/

[29] P. Klebine, “What does the spinal cord do? - Spinal Cord Injury Model System | UAB.” Accessed: Jul. 03, 2023. [Online]. Available: https://www.uab.edu/medicine/sci/faqs-about-spinal-cord-injury-sci/what-does-the-spinal-cord-do

[30] M. K. Ganapathy, V. Reddy, and P. Tadi, “Neuroanatomy, Spinal Cord Morphology,” in *StatPearls*, Treasure Island (FL): StatPearls Publishing, 2024. Accessed: Mar. 15, 2024. [Online]. Available: http://www.ncbi.nlm.nih.gov/books/NBK545206/

[31] N. Dafny, “Anatomy of the Spinal Cord (Section 2, Chapter 3) Neuroscience Online: An Electronic Textbook for the Neurosciences | Department of Neurobiology and Anatomy - The University of Texas Medical School at Houston.” Accessed: Jul. 03, 2023. [Online]. Available: https://nba.uth.tmc.edu/neuroscience/m/s2/chapter03.html

[32] “default - Stanford Medicine Children’s Health.” Accessed: Oct. 07, 2023. [Online]. Available: https://www.stanfordchildrens.org/en/topic/default?id=anatomy-of-the-spinal-cord-134-89

[33] D. Purves *et al.*, “The Internal Anatomy of the Spinal Cord,” in *Neuroscience. 2nd edition*, Sinauer Associates, 2001. Accessed: Sep. 14, 2023. [Online]. Available: https://www.ncbi.nlm.nih.gov/books/NBK11008/

[34] A. Saliani, B. Perraud, T. Duval, N. Stikov, S. Rossignol, and J. Cohen-Adad, “Axon and Myelin Morphology in Animal and Human Spinal Cord,” *Front. Neuroanat.*, vol. 11, p. 129, Dec. 2017, doi: 10.3389/fnana.2017.00129.

[35] J. L. Taylor, “Proprioception,” in *Encyclopedia of Neuroscience*, L. R. Squire, Ed., Oxford: Academic Press, 2009, pp. 1143–1149. doi: 10.1016/B978-008045046-9.01907-0.

[36] M. Harrow-Mortelliti, V. Reddy, and G. Jimsheleishvili, “Physiology, Spinal Cord,” in *StatPearls*, Treasure Island (FL): StatPearls Publishing, 2023. Accessed: Dec. 06, 2023. [Online]. Available: http://www.ncbi.nlm.nih.gov/books/NBK544267/

[37] G. Sengul and C. Watson, “Chapter 13 - Spinal Cord,” in *The Mouse Nervous System*, C. Watson, G. Paxinos, and L. Puelles, Eds., San Diego: Academic Press, 2012, pp. 424–458. doi: 10.1016/B978-0-12-369497-3.10013-5.

[38] P. Rea, “Chapter 8 - Spinal Tracts – Ascending/Sensory Pathways,” in *Essential Clinical Anatomy of the Nervous System*, P. Rea, Ed., San Diego: Academic Press, 2015, pp. 133–160. doi: 10.1016/B978-0-12-802030-2.00008-X.

[39] “Meninges | SEER Training.” Accessed: Sep. 13, 2023. [Online]. Available: https://training.seer.cancer.gov/brain/tumors/anatomy/meninges.html

[40] J. Y. Ghannam and K. A. Al Kharazi, “Neuroanatomy, Cranial Meninges,” in *StatPearls*, Treasure Island (FL): StatPearls Publishing, 2023. Accessed: Sep. 13, 2023. [Online]. Available: http://www.ncbi.nlm.nih.gov/books/NBK539882/

[41] “Meninges: What They Are & Function,” Cleveland Clinic. Accessed: Sep. 13, 2023. [Online]. Available: https://my.clevelandclinic.org/health/articles/22266-meninges

[42] “Cerebrospinal Fluid (CSF) Analysis: MedlinePlus Medical Test.” Accessed: Sep. 14, 2023. [Online]. Available: https://medlineplus.gov/lab-tests/cerebrospinal-fluid-csf-analysis/

[43] L. N. Telano and S. Baker, “Physiology, Cerebral Spinal Fluid,” in *StatPearls*, Treasure Island (FL): StatPearls Publishing, 2023. Accessed: Jun. 09, 2023. [Online]. Available: http://www.ncbi.nlm.nih.gov/books/NBK519007/

[44] L. Sakka, G. Coll, and J. Chazal, “Anatomy and physiology of cerebrospinal fluid,” *European Annals of Otorhinolaryngology, Head and Neck Diseases*, vol. 128, no. 6, pp. 309–316, Dec. 2011, doi: 10.1016/j.anorl.2011.03.002.

[45] J. H. T. Lee *et al.*, “A Novel Porcine Model of Traumatic Thoracic Spinal Cord Injury,” *Journal of Neurotrauma*, vol. 30, no. 3, pp. 142–159, Feb. 2013, doi: 10.1089/neu.2012.2386.

[46] J. H. Park *et al.*, “Analysis of equivalent parameters of two spinal cord injury devices: the New York University impactor versus the Infinite Horizon impactor,” *The Spine Journal*, vol. 16, no. 11, pp. 1392–1403, Nov. 2016, doi: 10.1016/j.spinee.2016.06.018.

[47] E. A. Salegio *et al.*, “A Unilateral Cervical Spinal Cord Contusion Injury Model in Non-Human Primates (*Macaca mulatta*),” *Journal of Neurotrauma*, vol. 33, no. 5, pp. 439–459, Mar. 2016, doi: 10.1089/neu.2015.3956.

[48] J. Liu *et al.*, “A Cervical Spinal Cord Hemi-Contusion Injury Model Based on Displacement Control in Non-Human Primates *(Macaca fascicularis)*,” *Journal of Neurotrauma*, vol. 37, no. 15, pp. 1669–1686, Aug. 2020, doi: 10.1089/neu.2019.6822.

[49] S. Jannesar, “The Mechanics of Contusion Spinal Cord Injury: Towards Patient-Specific Assessments of Mechanical Loading and Injury,” Simon Fraser University, 2019.

[50] I. Singhal *et al.*, “Finite element modeling of the human cervical spinal cord and its applications: A systematic review,” *North American Spine Society Journal (NASSJ)*, vol. 15, p. 100246, Sep. 2023, doi: 10.1016/j.xnsj.2023.100246.

[51] N. V. Olivera, “Modeling and Evaluation of a Finite Element Cervical Spinal Cord for Injury Assessment,” p. 61, 2020.

[52] M. Czyż, K. Ścigała, R. Będziński, and Włodzimierz Jarmundowicz, “Finite element modelling of the cervical spinal cord injury– clinical assessment,” *Acta of Bioengineering and Biomechanics; 04/2012; ISSN 1509-409X*, 2012, doi: 10.5277/ABB120403.

[53] C. Y. Greaves, M. S. Gadala, and T. R. Oxland, “A Three-Dimensional Finite Element Model of the Cervical Spine with Spinal Cord: An Investigation of Three Injury Mechanisms,” *Ann Biomed Eng*, vol. 36, no. 3, pp. 396–405, Mar. 2008, doi: 10.1007/s10439-008-9440-0.

[54] C. Persson, J. L. Summers, and R. M. Hall, “Modelling of Spinal Cord Biomechanics: In Vitro and Computational Approaches,” in *Neural Tissue Biomechanics*, vol. 3, L. E. Bilston, Ed., in Studies in Mechanobiology, Tissue Engineering and Biomaterials, vol. 3. , Berlin, Heidelberg: Springer Berlin Heidelberg, 2010, pp. 181–201. doi: 10.1007/8415_2010_38.

[55] M. Fournely, Y. Petit, E. Wagnac, M. Evin, and P.-J. Arnoux, “Effect of experimental, morphological and mechanical factors on the murine spinal cord subjected to transverse contusion: A finite element study,” *PLoS ONE*, vol. 15, no. 5, p. e0232975, May 2020, doi: 10.1371/journal.pone.0232975.

[56] C. Persson, J. Summers, and R. M. Hall, “The Effect of Cerebrospinal Fluid Thickness on Traumatic Spinal Cord Deformation,” *Journal of Applied Biomechanics*, vol. 27, no. 4, pp. 330–335, Nov. 2011, doi: 10.1123/jab.27.4.330.

[57] S. Jannesar *et al.*, “Natural variation of cervical spinal cord and canal morphometrics in non-human primates and its effect on spinal cord injury mechanics,” *J. Biomech.*, 2022.

[58] A. H. Khasawneh, R. J. Garling, and C. A. Harris, “Cerebrospinal fluid circulation: What do we know and how do we know it?,” *Brain Circ*, vol. 4, no. 1, pp. 14–18, 2018, doi: 10.4103/bc.bc_3_18.

[59] “Cerebrospinal Flow Dynamics,” Multiscale Flow Physics. Accessed: Oct. 09, 2023. [Online]. Available: http://asanchez.ucsd.edu/research/cerebrospinal-flow-dynamics/

[60] L. Howden *et al.*, “Three-dimensional cerebrospinal fluid flow within the human ventricular system,” *Computer Methods in Biomechanics and Biomedical Engineering*, vol. 11, no. 2, pp. 123–133, Apr. 2008, doi: 10.1080/10255840701492118.

[61] I. G. Bloomfield, I. H. Johnston, and L. E. Bilston, “Effects of proteins, blood cells and glucose on the viscosity of cerebrospinal fluid,” *Pediatr Neurosurg*, vol. 28, no. 5, pp. 246–251, May 1998, doi: 10.1159/000028659.

[62] H. Balasundaram, S. Sathyamoorthi, U. Fernandez-Gamiz, S. Noeiaghdam, and S. S. Santra, “Hydrocephalic cerebrospinal fluid flowing rotationally with pulsatile boundaries: A mathematical simulation of the thermodynamical approach,” *Theoretical and Applied Mechanics Letters*, vol. 13, no. 1, p. 100418, Jan. 2023, doi: 10.1016/j.taml.2022.100418.

[63] O. O. Adigun and M. A. Al-Dhahir, “Anatomy, Head and Neck: Cerebrospinal Fluid,” in *StatPearls*, Treasure Island (FL): StatPearls Publishing, 2023. Accessed: Oct. 09, 2023. [Online]. Available: http://www.ncbi.nlm.nih.gov/books/NBK459286/

[64] T. O. Wichmann, H. H. Damkier, and M. Pedersen, “A Brief Overview of the Cerebrospinal Fluid System and Its Implications for Brain and Spinal Cord Diseases,” *Front. Hum. Neurosci.*, vol. 15, p. 737217, Jan. 2022, doi: 10.3389/fnhum.2021.737217.

[65] C. F. Jones, J. H. T. Lee, B. K. Kwon, and P. A. Cripton, “Development of a large-animal model to measure dynamic cerebrospinal fluid pressure during spinal cord injury: Laboratory investigation,” *SPI*, vol. 16, no. 6, pp. 624–635, Jun. 2012, doi: 10.3171/2012.3.SPINE11970.

[66] K.-T. Kim *et al.*, “Differences in Morphometric Measures of the Uninjured Porcine Spinal Cord and Dural Sac Predict Histological and Behavioral Outcomes after Traumatic Spinal Cord Injury,” *Journal of Neurotrauma*, vol. 36, no. 21, pp. 3005–3017, Nov. 2019, doi: 10.1089/neu.2018.5930.

[67] J. Liu *et al.*, “Comparison of the anatomical morphology of cervical vertebrae between humans and macaques: related to a spinal cord injury model,” *Exp. Anim.*, vol. 70, no. 1, pp. 108–118, 2021, doi: 10.1538/expanim.20-0018.

[68] Y.-B. Yan, W. Qi, Z.-X. Wu, T.-X. Qiu, E.-C. Teo, and W. Lei, “Finite Element Study of the Mechanical Response in Spinal Cord during the Thoracolumbar Burst Fracture,” *PLoS ONE*, vol. 7, no. 9, p. e41397, Sep. 2012, doi: 10.1371/journal.pone.0041397.

[69] M. S. Chafi, V. Dirisala, G. Karami, and M. Ziejewski, “A finite element method parametric study of the dynamic response of the human brain with different cerebrospinal fluid constitutive properties,” *Proc Inst Mech Eng H*, vol. 223, no. 8, pp. 1003–1019, Nov. 2009, doi: 10.1243/09544119JEIM631.

[70] “What Is Fluid-Structure Interaction?” Accessed: Sep. 17, 2023. [Online]. Available: https://www.comsol.com/multiphysics/fluid-structure-interaction

[71] “Fluid-structure interactions | Fluid Mechanics Research Laboratory.” Accessed: Sep. 17, 2023. [Online]. Available: https://uwaterloo.ca/fluid-mechanics-research-lab/research/fluid-structure-interactions

[72] H. Zhang *et al.*, “Recent development of fluid–structure interaction capabilities in the ADINA system,” *Computers & Structures*, vol. 81, no. 8, pp. 1071–1085, May 2003, doi: 10.1016/S0045-7949(03)00009-9.

[73] J. Donea and A. Huerta, “Arbitrary Lagrangian-Eulerian Methods,” *ENCYCLOPEDIA OF COMPUTATIONAL MECHANICS*.

[74] T. Belytschko, W. K. Liu, and B. Moran, “Nonlinear Finite Elements for Continua and Structures,” 2000. [Online]. Available: https://api.semanticscholar.org/CorpusID:117989801

[75] “ALE Formulation.” Accessed: Mar. 27, 2024. [Online]. Available: https://2021.help.altair.com/2021/hwsolvers/rad/topics/solvers/rad/theory_ale_formulation_c.htm

[76] “Arbitrary Lagrangian-Eulerian Formulation (ALE).” Accessed: Mar. 27, 2024. [Online]. Available: https://doc.comsol.com/5.5/doc/com.comsol.help.comsol/comsol_ref_deformedmeshes.25.04.html

[77] K. E. Stoner, K. O. Abode-Iyamah, D. C. Fredericks, S. Viljoen, M. A. Howard, and N. M. Grosland, “A comprehensive finite element model of surgical treatment for cervical myelopathy,” *Clinical Biomechanics*, vol. 74, pp. 79–86, Apr. 2020, doi: 10.1016/j.clinbiomech.2020.02.009.

[78] Y. Lian, H. H. Bui, G. D. Nguyen, and A. Haque, “An effective and stabilised (u−pi) SPH framework for large deformation and failure analysis of saturated porous media,” *Computer Methods in Applied Mechanics and Engineering*, vol. 408, p. 115967, Apr. 2023, doi: 10.1016/j.cma.2023.115967.

[79] P. W. Cleary, M. Prakash, and J. Ha, “Novel applications of smoothed particle hydrodynamics (SPH) in metal forming,” *Journal of Materials Processing Technology*, vol. 177, no. 1, pp. 41–48, Jul. 2006, doi: 10.1016/j.jmatprotec.2006.03.237.

[80] Y. Wang, H. T. Tran, G. D. Nguyen, P. G. Ranjith, and H. H. Bui, “Simulation of mixed-mode fracture using SPH particles with an embedded fracture process zone,” *International Journal for Numerical and Analytical Methods in Geomechanics*, vol. 44, no. 10, pp. 1417–1445, 2020, doi: 10.1002/nag.3069.

[81] R. Vignjevic, M. Orłowski, T. De Vuyst, and J. C. Campbell, “A parametric study of bird strike on engine blades,” *International Journal of Impact Engineering*, vol. 60, pp. 44–57, Oct. 2013, doi: 10.1016/j.ijimpeng.2013.04.003.

[82] S. J. Lind, B. D. Rogers, and P. K. Stansby, “Review of smoothed particle hydrodynamics: towards converged Lagrangian flow modelling,” *Proc. R. Soc. A.*, vol. 476, no. 2241, p. 20190801, Sep. 2020, doi: 10.1098/rspa.2019.0801.

[83] L. D. G. Sigalotti, J. Klapp, and M. G. Gesteira, “The Mathematics of Smoothed Particle Hydrodynamics (SPH) Consistency,” *Frontiers in Applied Mathematics and Statistics*, vol. 7, 2021, Accessed: Dec. 07, 2022. [Online]. Available: https://www.frontiersin.org/articles/10.3389/fams.2021.797455

[84] W. Liu, Q. Hou, X. Lei, J. Lian, and J. Dang, “SPH modeling of substance transport in flows with large deformation,” *Front. Environ. Sci.*, vol. 10, Oct. 2022, doi: 10.3389/fenvs.2022.991969.

[85] Z. Tan, P.-N. Sun, N.-N. Liu, Z. Li, H.-G. Lyu, and R.-H. Zhu, “SPH simulation and experimental validation of the dynamic response of floating offshore wind turbines in waves,” *Renewable Energy*, vol. 205, pp. 393–409, Mar. 2023, doi: 10.1016/j.renene.2023.01.081.

[86] “Smooth Particle Hydrodynamics (SPH).” Accessed: Sep. 16, 2023. [Online]. Available: https://2021.help.altair.com/2021/hwsolvers/rad/topics/solvers/rad/smooth_particle_hydrodynamics_intro_c.htm

[87] “Abaqus - Mechanical and Civil Engineering Simulation.” Accessed: Oct. 10, 2023. [Online]. Available: https://www.3ds.com/products-services/simulia/products/abaqus/

[88] “Finite element conversion to SPH particles.” Accessed: Oct. 10, 2023. [Online]. Available: https://abaqus-docs.mit.edu/2017/English/SIMACAEANLRefMap/simaanl-c-sphconversion.htm

[89] M. V. Pathan *et al.*, “Predictions of the mechanical properties of unidirectional fibre composites by supervised machine learning,” *Sci Rep*, vol. 9, no. 1, p. 13964, Sep. 2019, doi: 10.1038/s41598-019-50144-w.

[90] M. Abedin, S. Mokhtari, and A. B. Mehrabi, “Bridge damage detection using machine learning algorithms,” in *Health Monitoring of Structural and Biological Systems XV*, P. Fromme and Z. Su, Eds., Online Only, United States: SPIE, Mar. 2021, p. 88. doi: 10.1117/12.2581125.

[91] B. M. Castro, U. A. Monteiro, R. H. R. Gutiérrez, D. H. C. D. S. S. Martins, and L. A. Vaz, “Numerical and experimental correlation of a catamaran’s vibration modes using supervised machine learning,” *Ocean Engineering*, vol. 259, p. 111838, Sep. 2022, doi: 10.1016/j.oceaneng.2022.111838.

[92] E. Villamor, C. Monserrat, L. Del Río, J. A. Romero-Martín, and M. J. Rupérez, “Prediction of osteoporotic hip fracture in postmenopausal women through patient-specific FE analyses and machine learning,” *Computer Methods and Programs in Biomedicine*, vol. 193, p. 105484, Sep. 2020, doi: 10.1016/j.cmpb.2020.105484.

[93] T. R. C. of Pathologists, “Histopathology.” Accessed: Sep. 20, 2023. [Online]. Available: https://www.rcpath.org/discover-pathology/news/fact-sheets/histopathology.html

[94] T. Bhatnagar *et al.*, “Relating Histopathology and Mechanical Strain in Experimental Contusion Spinal Cord Injury in a Rat Model,” *Journal of Neurotrauma*, vol. 33, no. 18, pp. 1685–1695, Sep. 2016, doi: 10.1089/neu.2015.4200.

[95] H. Das, B. Naik, and H. S. Behera, “An Experimental Analysis of Machine Learning Classification Algorithms on Biomedical Data,” in *Proceedings of the 2nd International Conference on Communication, Devices and Computing*, vol. 602, S. Kundu, U. S. Acharya, C. Kr. De, and S. Mukherjee, Eds., in Lecture Notes in Electrical Engineering, vol. 602. , Singapore: Springer Singapore, 2020, pp. 525–539. doi: 10.1007/978-981-15-0829-5_51.

[96] V. Filipović, “Optimization, Classification And Dimensionality Reduction In Biomedicine And Bioinformatics,” Jul. 2017, doi: 10.5281/ZENODO.827099.

[97] O. Khan, J. H. Badhiwala, J. R. F. Wilson, F. Jiang, A. R. Martin, and M. G. Fehlings, “Predictive Modeling of Outcomes After Traumatic and Nontraumatic Spinal Cord Injury Using Machine Learning: Review of Current Progress and Future Directions,” *Neurospine*, vol. 16, no. 4, pp. 678–685, Dec. 2019, doi: 10.14245/ns.1938390.195.

[98] M. M. Ali, B. K. Paul, K. Ahmed, F. M. Bui, J. M. W. Quinn, and M. A. Moni, “Heart disease prediction using supervised machine learning algorithms: Performance analysis and comparison,” *Computers in Biology and Medicine*, vol. 136, p. 104672, Sep. 2021, doi: 10.1016/j.compbiomed.2021.104672.

[99] V. Chaurasia and S. Pal, “Machine learning algorithms using binary classification and multi model ensemble techniques for skin diseases prediction,” vol. 34, no. 1, pp. 57–74, 2020.

[100] R. J. Urbanowicz *et al.*, “A Rigorous Machine Learning Analysis Pipeline for Biomedical Binary Classification: Application in Pancreatic Cancer Nested Case-control Studies with Implications for Bias Assessments.” arXiv, Sep. 08, 2020. Accessed: Feb. 11, 2023. [Online]. Available: http://arxiv.org/abs/2008.12829

[101] Q. A. Hathaway *et al.*, “Machine-learning to stratify diabetic patients using novel cardiac biomarkers and integrative genomics,” *Cardiovascular Diabetology*, vol. 18, no. 1, p. 78, Jun. 2019, doi: 10.1186/s12933-019-0879-0.

[102] P. Vurtur Badarinath, M. Chierichetti, and F. Davoudi Kakhki, “A Machine Learning Approach as a Surrogate for a Finite Element Analysis: Status of Research and Application to One Dimensional Systems,” *Sensors*, vol. 21, no. 5, p. 1654, Feb. 2021, doi: 10.3390/s21051654.

[103] A. Subasi, “Chapter 3 - Machine learning techniques,” in *Practical Machine Learning for Data Analysis Using Python*, A. Subasi, Ed., Academic Press, 2020, pp. 91–202. doi: 10.1016/B978-0-12-821379-7.00003-5.

[104] M. I. Jordan and T. M. Mitchell, “Machine learning: Trends, perspectives, and prospects,” *Science*, vol. 349, no. 6245, pp. 255–260, Jul. 2015, doi: 10.1126/science.aaa8415.

[105] C. Jimenez, C. J. Sparrey, and M. Narimani, “Identification of injured elements in computational models of spinal cord injury using machine learning,” *Annu Int Conf IEEE Eng Med Biol Soc*, vol. 2023, pp. 1–4, Jul. 2023, doi: 10.1109/EMBC40787.2023.10340243.

[106] “12.1 - Logistic Regression | STAT 462.” Accessed: Oct. 11, 2023. [Online]. Available: https://online.stat.psu.edu/stat462/node/207/

[107] “sklearn.linear_model.LogisticRegression,” scikit-learn. Accessed: Oct. 11, 2023. [Online]. Available: https://scikit-learn/stable/modules/generated/sklearn.linear_model.LogisticRegression.html

[108] “What is Overfitting? | IBM.” Accessed: Mar. 28, 2024. [Online]. Available: https://www.ibm.com/topics/overfitting

[109] “1.10. Decision Trees,” scikit-learn. Accessed: Oct. 11, 2023. [Online]. Available: https://scikit-learn/stable/modules/tree.html

[110] “1.4. Support Vector Machines,” scikit-learn. Accessed: Oct. 11, 2023. [Online]. Available: https://scikit-learn/stable/modules/svm.html

[111] “1.6. Nearest Neighbors,” scikit-learn. Accessed: Oct. 12, 2023. [Online]. Available: https://scikit-learn/stable/modules/neighbors.html

[112] A. Rycman, S. McLachlin, and D. S. Cronin, “A Hyper-Viscoelastic Continuum-Level Finite Element Model of the Spinal Cord Assessed for Transverse Indentation and Impact Loading,” *Front. Bioeng. Biotechnol.*, vol. 9, p. 693120, Aug. 2021, doi: 10.3389/fbioe.2021.693120.

[113] J. E. Akin, “Chapter 1: Finite Element Analysis Methods,” in *Finite Element Analysis Concepts Via SolidWorks*, World Scientific Publishing Co., 2010, p. 348.

[114] “Linear elastic behavior - SIMULIA User Assistance 2021.” Accessed: Apr. 29, 2024. [Online]. Available: https://help.3ds.com/2021/English/DSSIMULIA_Established/SIMACAEMATRefMap/simamat-c-linearelastic.htm?contextscope=all

[115] “Hyperelastic behavior of rubberlike materials - SIMULIA User Assistance 2021.” Accessed: Apr. 29, 2024. [Online]. Available: https://help.3ds.com/2021/English/DSSIMULIA_Established/SIMACAEMATRefMap/simamat-c-hyperelastic.htm?contextscope=all&id=90e204b2ec4244a9853e7af0999c9fbe#simamat-c-hyperelastic-strainenergy

[116] “Time domain viscoelasticity - SIMULIA User Assistance 2021.” Accessed: Apr. 29, 2024. [Online]. Available: https://help.3ds.com/2021/English/DSSIMULIA_Established/SIMACAEMATRefMap/simamat-c-timevisco.htm?contextscope=all

[117] L. Neron, R. Saurel, A. Chiapolino, and F. Fraysse, “Relaxation method for Mie–Grüneisen type equations of state,” *Physics of Fluids*, vol. 35, no. 11, p. 116112, Nov. 2023, doi: 10.1063/5.0169781.

[118] “Equation of state - SIMULIA User Assistance 2021.” Accessed: Apr. 29, 2024. [Online]. Available: https://help.3ds.com/2021/English/DSSIMULIA_Established/SIMACAEMATRefMap/simamat-c-eos.htm?contextscope=all&id=8db6894301ea46208c4e0fbd1f3ccc30

[119] D. Fleischman, J. P. Berdahl, J. Zaydlarova, S. Stinnett, M. P. Fautsch, and R. R. Allingham, “Cerebrospinal Fluid Pressure Decreases with Older Age,” *PLoS One*, vol. 7, no. 12, p. e52664, Dec. 2012, doi: 10.1371/journal.pone.0052664.

[120] N. Kheram *et al.*, “Cerebrospinal fluid pressure dynamics reveal signs of effective spinal canal narrowing in ambiguous spine conditions,” *Front. Neurol.*, vol. 13, p. 951018, Aug. 2022, doi: 10.3389/fneur.2022.951018.

[121] K. Soufi, A. Nouri, and A. R. Martin, “Degenerative Cervical Myelopathy and Spinal Cord Injury: Introduction to the Special Issue,” *JCM*, vol. 11, no. 15, p. 4253, Jul. 2022, doi: 10.3390/jcm11154253.

[122] R. Frantsuzov, S. Mondal, C. M. Walsh, J. P. Reynolds, D. Dooley, and D. B. MacManus, “A finite element model of contusion spinal cord injury in rodents,” *Journal of the Mechanical Behavior of Biomedical Materials*, vol. 142, p. 105856, Jun. 2023, doi: 10.1016/j.jmbbm.2023.105856.

[123] C. E. Korenczuk *et al.*, “Isotropic Failure Criteria Are Not Appropriate for Anisotropic Fibrous Biological Tissues,” *J Biomech Eng*, vol. 139, no. 7, pp. 0710081–07100810, Jul. 2017, doi: 10.1115/1.4036316.

[124] A. Barrios-Anderson, J. S. Fridley, D. A. Borton, and C. Saab, “Decoding nociception in the spinal cord: Computer modeling and machine learning,” in *Spinal Cord Injury Pain*, Elsevier, 2022, pp. 175–198. doi: 10.1016/B978-0-12-818662-6.00005-4.

[125] T. Inoue *et al.*, “XGBoost, a Machine Learning Method, Predicts Neurological Recovery in Patients with Cervical Spinal Cord Injury,” *Neurotrauma Reports*, vol. 1, no. 1, pp. 8–16, Jan. 2020, doi: 10.1089/neur.2020.0009.

[126] B. Galle, H. Ouyang, R. Shi, and E. Nauman, “Correlations between tissue-level stresses and strains and cellular damage within the guinea pig spinal cord white matter,” *Journal of Biomechanics*, vol. 40, no. 13, pp. 3029–3033, 2007, doi: 10.1016/j.jbiomech.2007.03.014.

[127] F. Pedregosa *et al.*, “Scikit-learn: Machine Learning in Python,” *Journal of Machine Learning Research*, vol. 12, no. 85, pp. 2825–2830, 2011.

[128] “Hyperparameter,” DeepAI. Accessed: Dec. 17, 2023. [Online]. Available: https://deepai.org/machine-learning-glossary-and-terms/hyperparameter

[129] R. Tri Prasetio, A. Akbar Rismayadi, N. Suryana, and R. Setiady, “Features Selection and k-NN Parameters Optimization based on Genetic Algorithm for Medical Datasets Classification:,” in *Proceedings of the 1st International Conference on Recent Innovations*, Jakarta, Indonesia: SCITEPRESS - Science and Technology Publications, 2018, pp. 3080–3086. doi: 10.5220/0009947130803086.

[130] L. Fradet, F. Cliche, Y. Petit, J.-M. Mac-Thiong, and P.-J. Arnoux, “Strain rate dependent behavior of the porcine spinal cord under transverse dynamic compression,” *Proc Inst Mech Eng H*, vol. 230, no. 9, pp. 858–866, Sep. 2016, doi: 10.1177/0954411916655373.

[131] M. Czyz, T. Tykocki, G. Miękisiak, K. Ścigała, R. Będziński, and W. Jarmundowicz, “Critical values of mechanical stress and strain during traumatic cervical spinal cord injury: Clinical study with the use of Finite Element Modelling,” *JBGC*, vol. 6, no. 2, p. p22, Sep. 2016, doi: 10.5430/jbgc.v6n2p22.

[132] C. Halimu, A. Kasem, and S. H. S. Newaz, “Empirical Comparison of Area under ROC curve (AUC) and Mathew Correlation Coefficient (MCC) for Evaluating Machine Learning Algorithms on Imbalanced Datasets for Binary Classification,” in *Proceedings of the 3rd International Conference on Machine Learning and Soft Computing*, Da Lat Viet Nam: ACM, Jan. 2019, pp. 1–6. doi: 10.1145/3310986.3311023.

[133] Q. Gu, L. Zhu, and Z. Cai, “Evaluation Measures of the Classification Performance of Imbalanced Data Sets,” in *Computational Intelligence and Intelligent Systems*, Z. Cai, Z. Li, Z. Kang, and Y. Liu, Eds., in Communications in Computer and Information Science. Berlin, Heidelberg: Springer, 2009, pp. 461–471. doi: 10.1007/978-3-642-04962-0_53.

[134] V. López, A. Fernández, S. García, V. Palade, and F. Herrera, “An insight into classification with imbalanced data: Empirical results and current trends on using data intrinsic characteristics,” *Information Sciences*, vol. 250, pp. 113–141, Nov. 2013, doi: 10.1016/j.ins.2013.07.007.

[135] S. Boughorbel, F. Jarray, and M. El-Anbari, “Optimal classifier for imbalanced data using Matthews Correlation Coefficient metric,” *PLOS ONE*, vol. 12, no. 6, p. e0177678, Jun. 2017, doi: 10.1371/journal.pone.0177678.

[136] J. T. Maikos and D. I. Shreiber, “Immediate Damage to The Blood-Spinal Cord Barrier Due to Mechanical Trauma,” *Journal of Neurotrauma*, vol. 24, no. 3, pp. 492–507, Mar. 2007, doi: 10.1089/neu.2006.0149.

[137] C. F. Dormann *et al.*, “Collinearity: a review of methods to deal with it and a simulation study evaluating their performance,” *Ecography*, vol. 36, no. 1, pp. 27–46, 2013, doi: 10.1111/j.1600-0587.2012.07348.x.

[138] L. L. Vercio *et al.*, “Supervised machine learning tools: a tutorial for clinicians,” *J. Neural Eng.*, vol. 17, no. 6, p. 062001, Nov. 2020, doi: 10.1088/1741-2552/abbff2.

[139] M. S. Khan, A. Abdul-Latif, S. S. R. Koloor, M. Petrů, and M. N. Tamin, “Representative Cell Analysis for Damage-Based Failure Model of Polymer Hexagonal Honeycomb Structure under the Out-of-Plane Loadings,” *Polymers (Basel)*, vol. 13, no. 1, p. 52, Dec. 2020, doi: 10.3390/polym13010052.

[140] S. N. S. H. Chittajallu, A. Richhariya, K. M. Tse, and V. Chinthapenta, “A Review on Damage and Rupture Modelling for Soft Tissues,” *Bioengineering (Basel)*, vol. 9, no. 1, p. 26, Jan. 2022, doi: 10.3390/bioengineering9010026.

Appendix A.

Mesh parameters for the evaluated small and large models of SCI

Table A.1. Small morphology meshing parameters

Part	Part type	Element type	Mesh pitch	Number of elements
White matter	Deformable solid	Hexahedral (C3D8R)	0.30 mm	31540
Gray matter	Deformable solid	Hexahedral (C3D8R)	0.30 mm	10790
Pia mater	Skin	Quadrilateral shell (S4R)	0.30 mm	5478
Dura mater	Deformable shell	Quadrilateral shell (S4R)	0.35 mm	5254
CSF	Solid converted to particles	Particle element (PC3D)	0.35 mm	13632
Spinal column	Discrete rigid shell	Quadrilateral (R3D4)	0.65 mm	1990
Impactor	Discrete rigid shell	Quadrilateral (R3D4)	0.5 mm	648

Table A.2. Large morphology meshing parameters

Part	Part type	Element type	Mesh pitch	Number of elements
White matter	Deformable solid	Hexahedral (C3D8R)	0.40 mm	22491
Gray matter	Deformable solid	Hexahedral (C3D8R)	0.40 mm	8316
Pia mater	Skin	Quadrilateral shell (S4R)	0.40 mm	4032
Dura mater	Deformable shell	Quadrilateral shell (S4R)	0.45 mm	4088
CSF	Solid converted to particles	Particle element (PC3D)	0.35 mm	17892
Spinal column	Discrete rigid shell	Quadrilateral (R3D4)	0.65 mm	1990
Impactor	Discrete rigid shell	Quadrilateral (R3D4)	0.5 mm	648

Appendix B.

Figures of spinal cord lateral shift at the time of maximum compression in the FE models of SCI

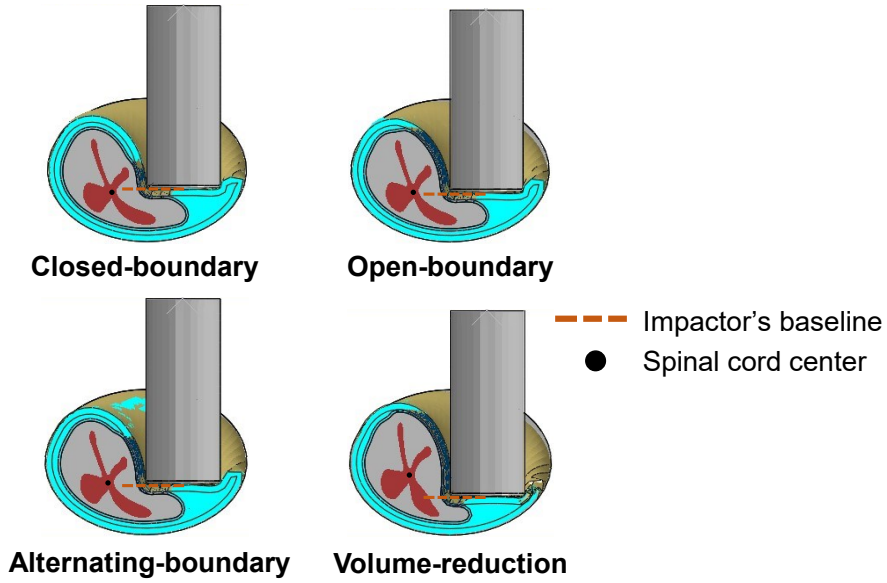

Figure B.1. **Comparison of the spinal cord's lateral shift for every CSF boundary condition evaluated in the small SCI model. The figure shows the cord's lateral shift with respect to the impactor's baseline at the impact epicenter.**

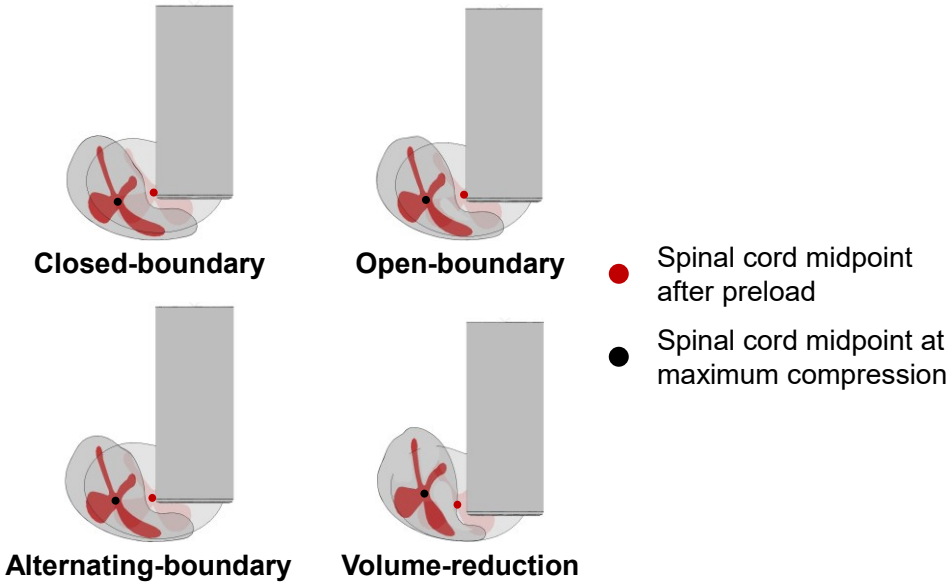

Figure B.2. **Comparison of the spinal cord midpoint's shift between the end of the preload (translucent shape in the back), and the time of maximum compression in the impact phase of the small SCI model for each evaluated CSF boundary condition.**

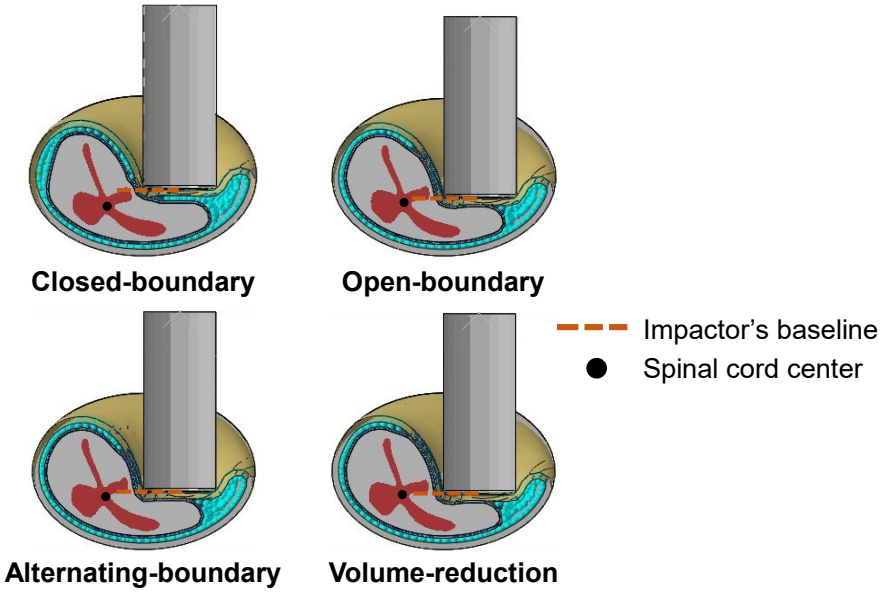

Figure B.3. **Comparison of the spinal cord's lateral shift for every CSF boundary condition evaluated in the average SCI model. The figure shows the cord's lateral shift with respect to the impactor's baseline at the impact epicenter.**

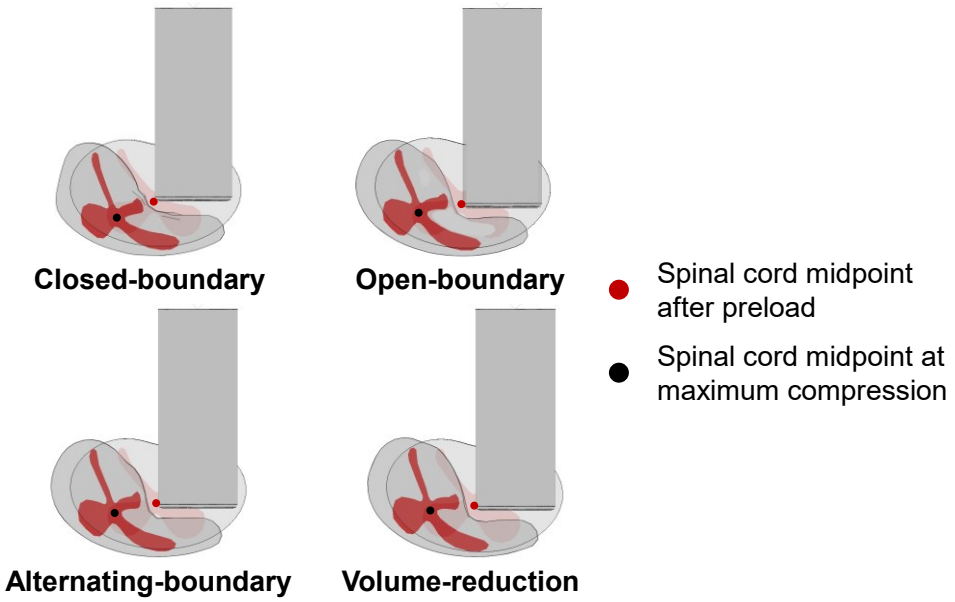

Figure B.4. Comparison of the spinal cord midpoint's shift between the end of the preload (translucent shape in the back), and the time of maximum compression in the impact phase of the average SCI model for each evaluated CSF boundary condition.

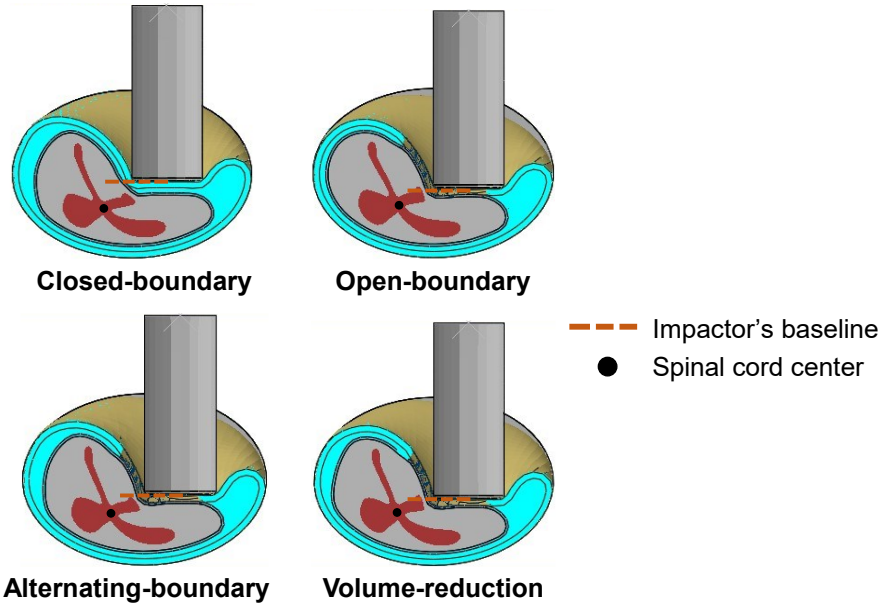

Figure B.5. Comparison of the spinal cord's lateral shift for every CSF boundary condition evaluated in the large SCI model. The figure shows the cord's lateral shift with respect to the impactor's baseline at the impact epicenter.

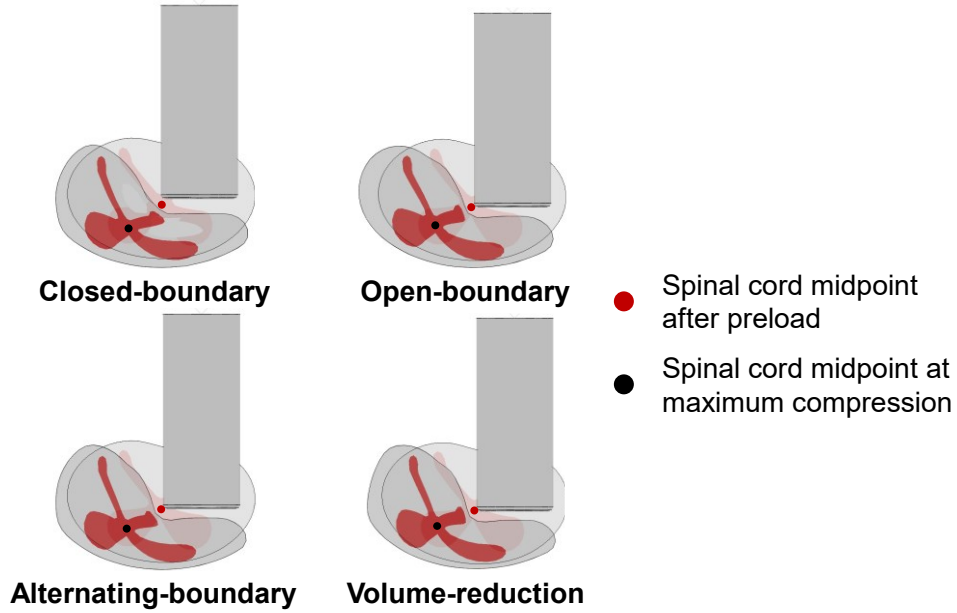

Figure B.6. Comparison of the spinal cord midpoint's shift between the end of the preload (translucent shape in the back), and the time of maximum compression in the impact phase of the large SCI model for each evaluated CSF boundary condition.

Appendix C.

Deformed shapes of the spinal cord cross-sections at the end of the preload phase in the FE models of SCI

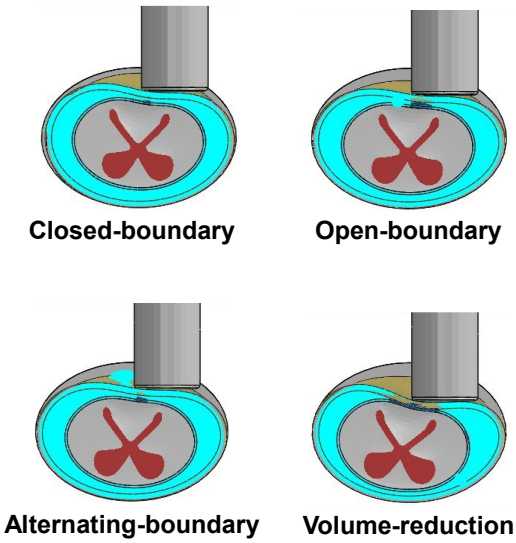

Figure C.1. Compression of the spinal cord at the end of the preload for every CSF containment method in the small SCI model.

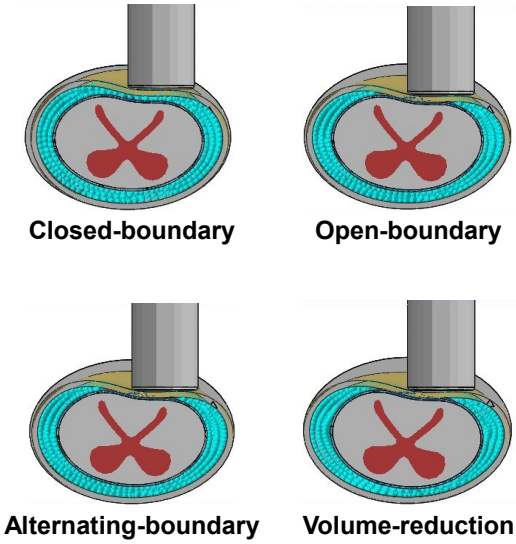

Figure C.2. Compression of the spinal cord at the end of the preload for every CSF containment method in the average SCI model.

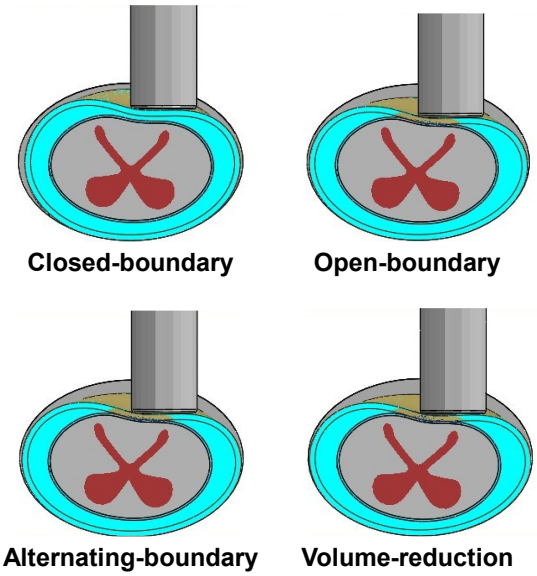

Figure C.3. Compression of the spinal cord at the end of the preload for every CSF containment method in the large SCI model.